UNIVERSITÀ DEGLI STUDI DI MILANO

Scuola di Dottorato in Fisica, Astrofisica e Fisica Applicata

Dipartimento di Fisica

Corso di Dottorato in Fisica, Astrofisica e Fisica Applicata

Ciclo XXXIII

Isospin mixing in the nucleus ^{60}Zn

Settore Scientifico Disciplinare FIS/04

Supervisor: Prof. Franco Camera

Co-Supervisor: Prof. Angela Bracco

Coordinator of the School: Prof. Matteo PARIS

PhD thesis of:

Giulia Gosta

Academic year 2019/2020

Commission of the final examination:

External Member:
Giuseppe Gorini

External Member:
Gabriele Pasquali

Internal Member:
Franco Camera

Final examination:

Date 18/12/2020

Università degli Studi di Milano, Dipartimento di Fisica, Milano, Italy

To Pu

The most successful people are those who are good at plan B.
James A. Yorke

Contents

Introduction

Isospin symmetry was introduced by Heisenberg in 1932, to cope with the experiments finding of the charge symmetry and the charge independence of the nucleons interaction, namely n-n, p-p and n-p interactions are the same. In the isospin formalism, neutrons and protons are viewed as two quantum states of the same particle, the nucleon, with isospin projection $I_z = 1/2$ and $I_z = -1/2$ for proton and neutron, respectively. Consequently, a nucleus has a well defined value of $I_z = (N-Z)/2$, while I, according to quantum mechanics rules, can assume values $(N-Z)/2 < I < (N+Z)/2$. In general, for N=Z nuclei, the nuclear ground state corresponds to the lower value of isospin $I = |I_z|$. This symmetry doesn't hold for the Coulomb interaction between protons in the nucleus and this leads to a breaking of the symmetry which induces a mixing between states with different values of the isospin. This phenomenon is called *isospin mixing*. The consequence is that it is not possible to assign a unique value of isospin to a nuclear state. Because the nuclear force overwhelms the Coulomb interaction, a perturbation approach can be used to describe the isospin mixing. In a previous work (1), it is shown that the value of the isospin mixing in the ground state can be obtained from the measurement of isospin mixing at high excitation energy, by using the theoretical approach reported in (2). For ^{60}Zn the theoretical expectation value for the mixing probability in the ground state α^2 is about 2-3% as reported in (3). The knowledge of isospin impurities is interesting in several contexts such as the properties of Isobaric Analog State (IAS) and the Fermi β-decay of the N $\sim$ Z nuclei near the proton drip line. For β-decay, the isospin impurity of states gives an important correction factor to the Fermi transition rates from which the first element of Cabibbo–Kobayashi–Maskawa matrix is deduced (3).

The breaking of the isospin symmetry can be identified by observing a transition that would have been forbidden by the selection rules if the mixing of states was not present. In this connection, the γ-decay of Giant Dipole Resonance (GDR),

in which the total strength of E1 transition is concentrated, is a perfect probe to investigate this effect (4, 5). In fact, in the long wavelength approximation, E1 transitions, as those from the GDR, are possible only between states with difference of isospin equal to one ($\Delta I = 1$). This approach has been employed to measure the isospin mixing in nuclei at finite temperature T, formed in fusion evaporation reactions. In this type of experiments the use of self-conjugate projectile and target nuclei ensures the population of a compound nucleus (CN) with I=0. The yield of the GDR gamma decay can be measured and thus the mixing amplitude deduced. A partial restoration of the isospin symmetry is expected at high temperature due to the decreasing of CN lifetime for particle decay according to the hypothesis of Wilkinson in 1956 (6).
The experiment, on which this thesis is based, was performed at Laboratori Nazionali di Legnaro (LNL). In order to deduce the isospin mixing effect in the nucleus ^{60}Zn, the fusion-evaporation reaction ^{32}S + ^{28}Si in a I=0 channel was employed. Moreover, a similar reaction ^{32}S + ^{30}Si was used to produce ^{62}Zn in a I$\neq$0 channel. This last reaction was used to study the decay of the compound nucleus and thus to fix the parameters entering in the statistical model and describing of the GDR strength function. These values were used to describe the reaction with isospin mixing so that the mixing coefficient is the only free parameter left in the analysis. Both of nuclei were produced at 2 different excitation energies (E_1*=47 MeV and E_2*=58 MeV) in order to study the trend of mixing probability with nuclear temperature (where $T_1\approx$2 MeV and $T_2\approx$2.4 MeV).
In this thesis we report on a study addressing the problem of isospin mixing in ^{60}Zn. The aim of the thesis is to analyse the data for the 4 reactions to obtain the following:

- to test experimentally the trend of the temperature dependence of the isospin mixing;
- to extract the value of the isospin mixing for Z = 30 at zero temperature;
- to extract the isospin mixing correction δ_c necessary to obtain the correct ft value of super-allowed Fermi transitions.

In the first chapter the theoretical model of isospin mixing together with the CN and resonances description is proposed. In the second chapter there is the description of the experiment performed to study the isospin mixing phenomenon. In the 3 following chapters the preliminary analysis is presented and in the last 3 there is the conclusive analysis and the results.

Part I

Introduction

CHAPTER 1

Overview of the theoretical models

Every sentence I utter must be understood not as an affirmation, but as a question.

Niels Bohr

1.1 Compound nuclear reactions

1.1.1 The Bohr independence hypothesis

The compound nucleus (CN) theory was developed by Bohr in 1936. The model for a formation of a CN with a bombarding particle with energy around the coulomb barrier, is based on the fact that the nuclear force is so strong that the projectile is captured in the target nucleus and it can't escape before the complete sharing of the energy has occurred. The Bohr independence hypothesis claims that the decay of a compound nucleus is determined entirely by its energy, angular momentum and parity, but not on the way it was formed. This requires that the mean free path of the projectile in the nucleus is much shorter than the nuclear radius, so there is no chance to escape before the statistical equilibrium. Estimating the mean free path from the classical relation $\lambda = (\sigma\rho)^{-1}$ where σ is the total interaction cross section and ρ the nuclear density, the mean free path turns out to be about 1 fm, which is less than the nuclear radius. Actually, this assumption is a good approximation at low energies, but becomes less valid as the incident energy increases, starting from some MeV/nucleon. For the validity of the hypothesis is also required that a long time should elapse between the formation and the decay, that happens if the average excitation energy per nucleon is much less than the energy needed by any one of them to escape. This ensures that many interactions must take place before sufficient energy is concentrated on one particle to enable it to escape. Compound

nuclear reactions are found to take place when a projectile is captured creating a compound nucleus in an excited energy state which subsequently decays by gamma or particle emission. Between its formation and the decay, the excitation energy is shared statistically among the nucleons so that the memory of the formation mode is lost. For this reason, the two processes, the formation and the decay are independent of each other. In the CN model, at the moment of interaction, the projectile collides with the target nucleus. At the end of the process the compound nucleus reaches the statistical equilibrium and slowly emits particles until it is energetically possible, when decay to the ground state by beta and gamma emission. Unfortunately, it is not possible to measure the time emission of particles from a nuclear reaction with sufficient precision to resolve these stages experimentally. One of the possible way used to study the compound nucleus reaction is to evaluate the energy spectra of the particles of the different type as a function of the emission angle. These spectra are composed by both resolved peaks and peaks merged into a continuum. The peaks discrimination depends, on one side, on the energy and target nucleus and on the other side, on the energy resolution of the detecting apparatus. In fact, at low energy, the level width is much smaller than the level spacing ($\Gamma \ll D$) and so the states can be resolved energetically. As the energy increases, both the level density and the level width increase and when the level width overcomes the level spacing ($\Gamma \gg D$), the cross section going to the discrete states is negligible and only the continuum states must be considered. A schematic representation of the process is shown in figure 1.1.

1.1.2 The Hauser-Feshbach theory

For the CN theory, nucleus formation gives the cross section of the reaction and it is based on the Bohr independence hypothesis. The basic idea is to consider the nucleus formed through a reaction channel α, that can decay by a number of channels β. We assume that only compound nucleus processes take place and that the final CN is in a single angular momentum state. Thus, the cross section depends on the orbital angular momentum, the transmission coefficient for the channel α (T_α) and for the time reversal state for the channel β ($T_{\hat{\beta}}$) (7):

$$\sigma_{\alpha\beta} = \pi\lambda_\alpha^2 \frac{T_\alpha T_{\hat{\beta}}}{\sum_i T_i} \tag{1.1}$$

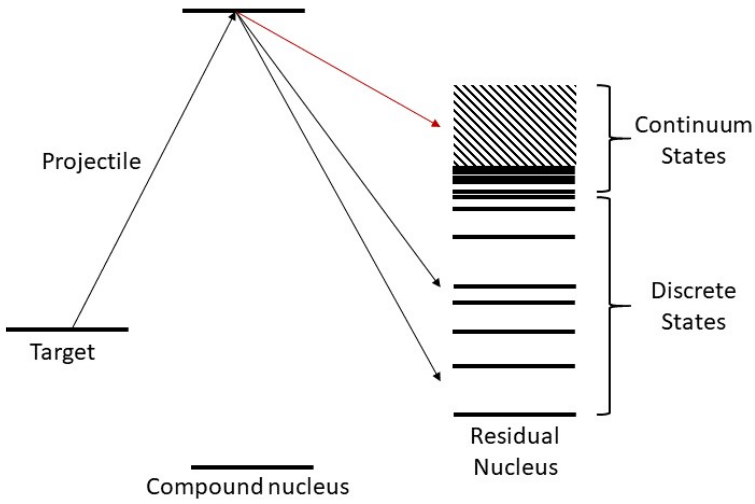

Figure 1.1: Compound nucleus: at low energy, the level width is much smaller than the level spacing ($\Gamma \ll D$) and so the states are resolvable. At increasing energy, both the level density and the level width increase and when the level width becomes broader than the level spacing ($\Gamma \gg D$), the continuum states must be considered.

This cross section does not consider the spin and the continuum space. The conservation of isospin imposes a constraint on compound nucleus reactions, forbidding transitions to certain final states. Since, however, this is not absolute, the measurement of the cross sections of isospin-forbidden reactions gives an estimate of the isospin breaking. The Hauser-Feshbach theory has been extensively applied to the analysis of the compound nucleus reaction to discrete state. But this theory in only applicable in reaction in which there are no direct contribution to any of the non-elastic outgoing channels.

1.1.3 CN formation

The formation and the one-step decay of compound nucleus can be written schematically as:

$$A + B \rightarrow C^* \rightarrow R^* + r \tag{1.2}$$

where A is the projectile, B the target nucleus; the compound nucleus C is created in an excited state and R is the excited residual nucleus populated after the emission of the particle r.
In the center of mass frame, the maximum excitation energy (E^*_{CN}) given to the

system by the fusion reaction is provided by the expression:

$$E^*_{CN} = Q + E_{CM} \tag{1.3}$$

where Q is the Q-value of the reaction and E_{CM} is the kinetic energy in the center of mass that depends on the kinetic energy in the laboratory frame of the projectile nucleus E_{lab}, the projectile nuclear mass M_p and the nuclear mass of the target M_t:

$$E_{CM} = E_{lab}\frac{M_t}{M_p + M_t} \tag{1.4}$$

E_{CM} must be larger than the repulsive interaction originated from the Coulomb interaction and the centrifugal potential:

$$E_{CM} > \frac{Z_p Z_t e^2}{R_c} + \frac{\hbar^2 j(j+1)}{2\mu R_c} \tag{1.5}$$

where Z_p and Z_t are the charge of the target and the projectile, R_c is the Coulomb barrier radius, j is the angular momentum of the system and μ is the reduced mass.

1.1.4 Statistical description of the CN decay

As described in the previous section, the CN is formed in an exited state and with the increase of excitation energy, the energy distance between two levels becomes smaller than the decay width. In this situation is more convenient to describe the system in term of continuum level density instead of single levels. From to the Bohr independence hypothesis the CN and its decay can be analyzed using a statistical approach in which all degrees of freedom are in equilibrium and thus all the states with the same angular momentum J, parity π and excitation energy E^* have an equal probability to be populated. The probability p_i to find the CN in a state i at an energy E_i, angular momentum J_i and parity π_i will be:

$$p_i = \frac{\delta(E_i - E^*)\delta(J_i - J)\delta(\pi_i - \pi)}{\rho(E^*)} \tag{1.6}$$

where $\rho(E^*)$ is the density of states. The conservation of the quantum numbers introduces other multiplicative δ factors. This probability distribution is called Microcanonical (8). The nuclear level density $\rho(E^*)$ can be written in term of the entropy of the system:

$$\rho(E^*) = \rho_0 \exp(S(E^*)) \tag{1.7}$$

Now, starting from the analogy with a system in thermodynamic equilibrium, it is possible to introduce the concept of nuclear temperature T:

$$T = (\frac{dS}{dE^*})^{-1} = (\frac{1}{\rho}\frac{d\rho}{dE^*})^{-1} \tag{1.8}$$

In order to describe, in detail, the level density of the system, the Fermi gas model can be useful, because of the many degrees of freedom involved at high excitation energy. In this model, the level density is obtained by counting the number of ways in which the excitation energy of the system can be distributed among single particle states, described in term of plane-waves. For N $\approx$ Z $\approx \frac{A}{2}$ the result is:

$$\rho(A, E^*) \approx \frac{e^{2(\sqrt{aE^*})}}{\sqrt{48}E^*} \tag{1.9}$$

where the empirical value of the level density parameter is a = $\frac{A}{k}$ (see figure 1.2). The general requirement for a physical system to be described using a statistical approach is a large elements number. In this sense, the comparison between the atomic nucleus (with A $\sim$ 100 nucleons) with a classic gas (with 10^{23} particles) seems to be improper. Anyway, the statistical description appears more reasonable if we think of the CN in terms of the high number of states. Combining the equations 1.9 and 1.8, the explicit relation between the nuclear temperature and the excitation energy is pointed out:

$$E^* = aT^2 \tag{1.10}$$

In analogy with the classical gas, the energy distribution of particles emitted during the CN evaporation process is expected to be Maxwell-Boltzmann distribution. With the increasing of the projectile energy, anyway, the limit of the Bohr independence hypothesis becomes more evident due to the increase of the probability of pre-equilibrium emission (i.e. the emission of particle before the thermodynamic equilibrium has been reached)(9).

1.1.5 CN Decay

In order to describe the evaporation spectra for compound nuclei, it is necessary to consider the three main ingredients of the statistical model: the transmission coefficients or barrier penetration factors for particle emission, an excitation-energy dependent level-density parameter and the angular-momentum dependence of the level density. In the statistical model calculation it is important to have realistic spin distribution for the compound nuclei. The fusion cross section as a function of spin was assumed to have the form (10):

$$\sigma_{Fus}(J) = \pi\lambda^2 \sum \frac{(2J+1)}{1 + exp(\frac{J-J_0}{d})} \tag{1.11}$$

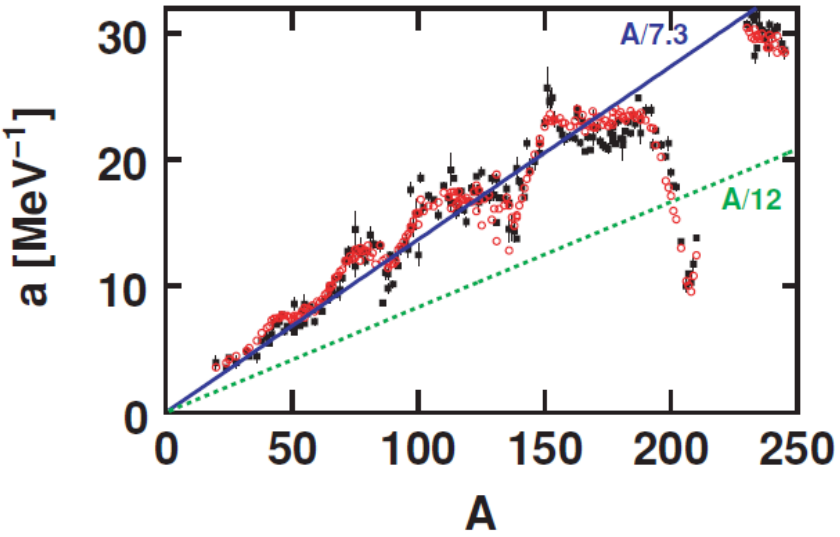

Figure 1.2: Mass dependence of level-density parameters. Experimental points from neutron-resonance counting are shown as the solid square data points. The blue line is the linear interpolation of the data in comparison with the trend deduced from the independent-particle model (green line). The red dots where obtained with a more sophisticated model taking into account the shell effect for single nuclei (10)

where J_0 is the maximum value of the angular momentum before the fission and can be obtained from systematic or from the Bass model (11). Instead, d is the diffuseness which can vary from 2 up to 10. The evaporation of light particles is treated with the Hauser-Feshbach formalism (12), which explicitly takes into account the spin degrees of freedom. The partial decay width of a CN of excitation energy E^* and spin J_{CN} for the evaporation of particle i is:

$$\Gamma_i(E^*, J_{CN}) = \frac{1}{2\pi\rho_{CN}(E^*, J_{CN})} \int d\epsilon \sum_{J_d=0}^{\infty} \sum_{J=|J_{CN}-J_d|}^{J_{CN}+J_d} \sum_{l=|J-S_i|}^{J+S_i} T_l(\epsilon)\rho_d(E^* - B_i - \epsilon, J_d) \tag{1.12}$$

where J_d is the spin of the daughter nucleus; S_i , J and l are the spin, the total angular momentum and the orbital angular momentum of the evaporated particle; ϵ and B_i are its kinetic and separation energy; T_l is its transmission coefficient or barrier penetration factor; ρ_d and ρ_{CN} are the level densities of the daughter and CN, respectively.

1.2 Giant resonances

1.2.1 Introduction

A powerful method to study the properties of nuclear systems is to examine their response to photon absorption or to the electromagnetic scattering of particles. From what we know, nuclei consisting in protons and neutrons (nucleons) show both independent-particle and collective behaviour, as reported in 1.3.

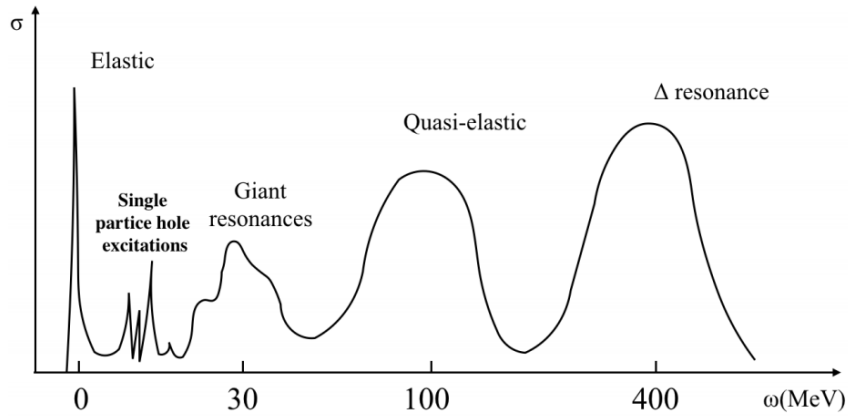

Figure 1.3: Characteristic response of atomic nucleus as a function of energy transfer. (5)

In general, up to about 10 MeV of energy, the nucleus responds through simple state excitation involving, usually, only few particles. Instead, at excitation energy between 10 and 30 MeV the nuclear system exhibits broad resonances. These states are the *Giant Resonances* that correspond to a collective motion involving many, if not all, the nucleons in the nucleus. From a quantum mechanical point of view, they represent a transition between the ground state and the collective state and their strength is described by a transition amplitude. The strength of the transition depends on the number of particles involved and the size of the system. From this follows that the total strength is limited by a sum rule, which depends only on ground state properties and we call the transition *Giant Resonance* if its strength exhausts a major part of the sum rule. Macroscopically, a giant resonance can be seen as a high-frequency, damped, (nearly) harmonic density/shape vibration around the density/shape equilibrium of the nuclear system. A (giant) resonance, as reported in figure 1.4 (13), is described by three characteristics parameters: the centroid energy E_R, the width Γ_R and the strength S_R (5) and fitted with a Lorentzian distribution:

$$\sigma(E) = \frac{\sigma_m \Gamma_m^2 E^2}{(E^2 - E_m^2)^2 + \Gamma_m^2 E^2} \tag{1.13}$$

where σ_m, Γ_m and E_m are respectively the peak cross section, the resonance width and the resonance energy.

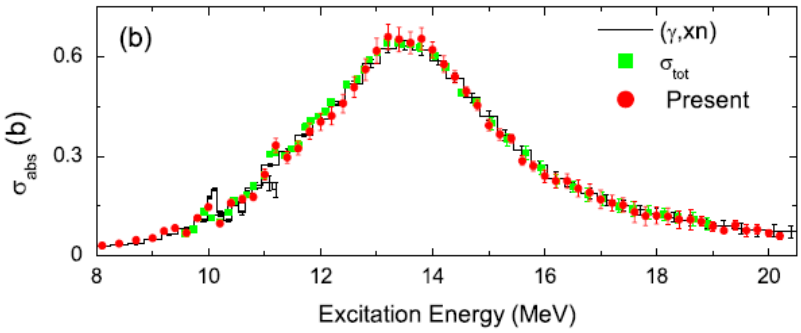

Figure 1.4: Photoabsorption cross sections in the GDR region for the nucleus ^{208}Pb (14)

1.2.2 Giant Resonance modes

The types of giant resonances can be classified according to their multipolarity L, spin S and isospin I quantum numbers, as represented in figure 1.5.

- The ΔS=0, ΔT=0 modes are *electric* and *isoscalar* vibrations in which protons and neutrons oscillate in phase.
- The ΔS=0, ΔT=1 modes are *electric* and *isovector* vibrations in which protons and neutrons oscillate out of phase against each other.
- The ΔS=1 ,ΔT=0 modes are *magnetic* and *isoscalar* vibrations in which nucleons with spin up vibrate against nucleons with spin down.
- The ΔS=1, ΔT=1 modes are *magnetic* and *isovector* vibrations in which protons with spin down/up oscillate against neutrons with spin up/down.

This thesis deals with the analysis of the experimental data on the Isovector Giant Dipole Resonance (IVGDR), for this reason in the following we will focus on it.
The IsoVector Giant Dipole Resonance (IVGDR) is the best known and studied giant resonance. The dipole vibration is a very general phenomenon, since it occurs in all the nuclei from the ^4He up to ^{238}U (13). The IVGDR has been historically observed in photo-absorption experiment with a γ-ray beam of energies between

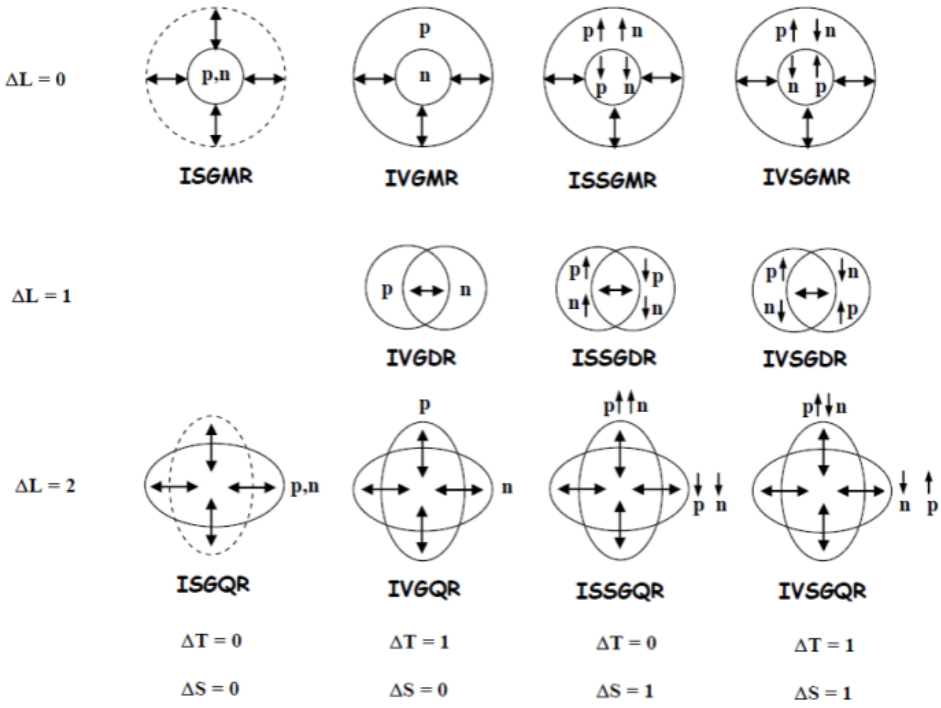

Figure 1.5: Schematic representation of various collective modes.(5)

10 to 30 MeV, but can also be excited with virtual photons. With real photons the wavelength associated to the projectile ($\hbar\omega \approx 15$MeV) is $\lambda \approx 100$ fm, much larger than the nuclear radius. In this condition it is possible to assert that the nucleus feels a constant electric field E and the protons move in the direction of E. To keep at rest the center of mass and to conserve the momentum, the neutrons move in the opposite direction. The attractive nuclear force acts as a restoring force which reverses the motion of neutrons and protons. This description follows the semi-classical hydrodynamic model of Goldhaber and Teller (15). Microscopically, one can construct the giant resonance from a coherent superposition of particle-hole states based on the shell model. The IVGDR centroid energy E_0 depends on the nuclear mass. It has been parametrized using a combined power relation (13):

$$E_0 = 31.2A^{-\frac{1}{3}} + 20.6A^{-\frac{1}{6}} MeV, \tag{1.14}$$

where A is the nucleus mass number, the first term is a volume term and the second one is a surface term. The trends of experimental data is such that the term $A^{-\frac{1}{3}}$ becomes dominant for increasing A. This can be explained by the fact that in heavier nuclei a larger fraction of the nucleons is located in the interior (rather than

on the surface), so the surface term becomes less important. Whilst in spherical nuclei the strength distribution can be well represented by Lorentzian shape (Eq. 1.13), in axially symmetric deformed nuclei the photo-absorption cross section is split in two Lorentzian components (see figure 1.6) with different centroids, corresponding to the different oscillation axis. The strength of the IVGDR, in terms of the Thomas-Reiche-Kuhn (TKR) sum rule, is:

$$S_{IVGDR} = \int_{E_{min}}^{E_{max}} \sigma_{\gamma}^{abs} dE = \frac{60NZ}{A} MeVmb \tag{1.15}$$

S_{IVGDR} exhausts $\approx 100\%$ of the energy weighted sum rules for the electric dipole operator and the γ-decay of the IVGDR has a E_1 character. The width of the IVGDR built on the nuclear ground states varies from ≈ 4 MeV up to ≈ 8 MeV and it can be described microscopically as a sum of two contributes:

$$\Gamma_{IVGDR} = \Gamma^{\uparrow} + \Gamma^{\downarrow} \tag{1.16}$$

where $\Gamma^{\uparrow}$ is the *escape width*, associated to particle emission, while $\Gamma^{\downarrow}$ is the *spreading width* due to the coupling of the 1p-1h state to more complicated configuration (np-nh). The contribution of $\Gamma^{\uparrow}$ is, for heavy nuclei, less than 10%, so $\Gamma^{\downarrow}$ is the dominant term.

1.2.3 IVGDR in hot nuclei

Nuclei at high excitation energy decay by emission of light particles such as neutrons, protons, alphas and also by emission of γ-rays, though at a probability about $10^{-3} - 10^{-5}$ smaller. According to the statistical model, with the increasing of γ-rays energy, the yield should exponentially drop down, but experimentally it has been observed an enhancement in the region of the IVGDR. This observation was explained by the consideration that the compound system, formed at a certain excitation energy E*, is coupled to a system in which the IVGDR is built on an excited state. Indeed, in 1955 Brink suggested the possibility to build the IVGDR on excited state and this suggestion became the *Brink-Axel hypothesis* (16)(17): giant resonance (not only the IVGDR) can be built on each nuclear state and its overall characteristics do not depend on the microscopical structure but on the bulk properties of the system. The measurement of γ-decay spectra of nuclei as a function of the compound nucleus excitation energy E_x and angular momentum J, allows one to study how nuclear properties are affected by temperature and spin. We can define the intrinsic excitation energy or temperature as following:

$$E_{int}(CN) = E^* - E_{yrast} = aT^2 \tag{1.17}$$

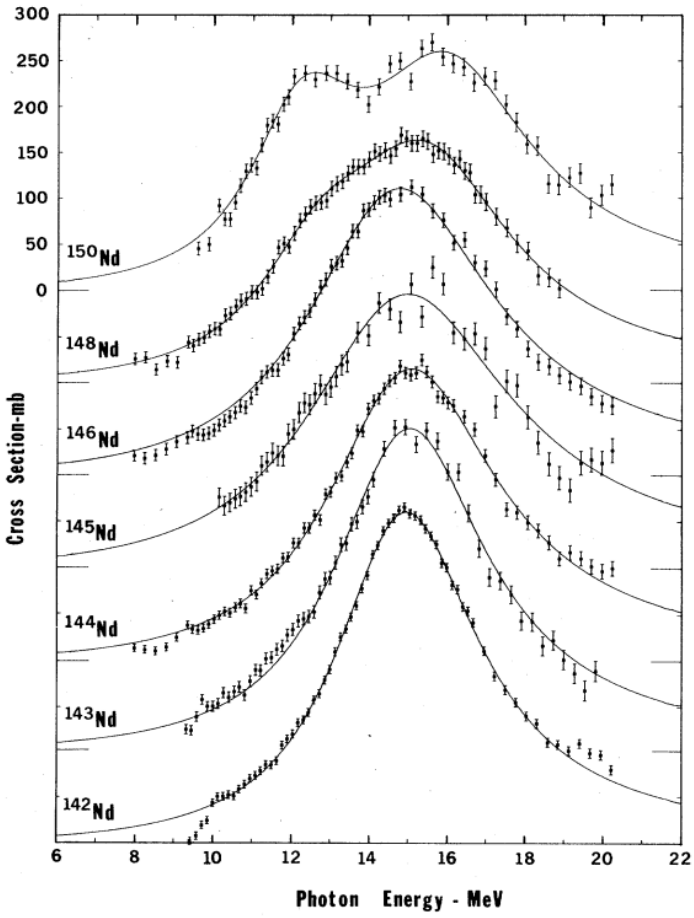

Figure 1.6: Total photoneutron cross sections for the neodymium isotopes, showing the "evolution" of the giant resonance from spherical to statically deformed nuclei. (13)

where E^* is the compound nucleus excitation energy, E_{yrast} is the rotational energy and the level density parameter is $a = \frac{A}{k} MeV^{-1}$ with k=8-12 MeV. If we want to determine the excitation energy of the excited state on which the IVGDR is built, we should subtract the collective and the rotational energy form the CN energy E_x:

$$E_x = E_{int}(CN) - E_R(IVGDR) \tag{1.18}$$

Because the shell structures are predicted to dissolve for a temperature higher

than 1-1.5 MeV, differences between cold and hot nuclei are expected. One of the possible consequence is that nuclei, that are deformed in the ground state (prolate), will become spherical because of the disappearance of shell effects. If they have in addition a non-zero angular momentum, as in the case of heavy-ion fusion reaction , they are expected to become non collective rotators like in any classical system.

The heavy-ion fusion reactions are good methods to obtain a hot equilibrated compound nucleus, in which both energy and angular momentum are transferred to compound system. This is schematically described in figure 1.7.

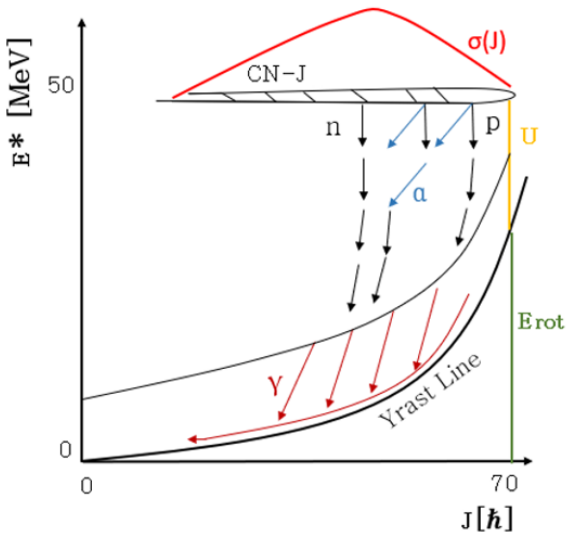

Figure 1.7: Schematic of the compound nucleus decay process. The compound nucleus decays by emission of particles, up to the particle binding energy and then by emission of γ-rays along the Yrast line and just above it.

In general, neither the initial energy nor the angular momentum of compound nucleus are sharply defined. For excitation energy higher than some MeV/nucleon, processes other than fission, such as pre-equilibrium emission and incomplete fusion can occur and generate the energy uncertainty. The spread in J originates, instead, from the spread in the impact parameter of the collision. As explained before, the statistical description of CN decay is based on the assumption that all the degrees of freedom have reached statistical equilibrium before the cooling process (decay). Following the Axel-Brink hypothesis, we can express the decay probability σ_{decay}

as a function of the absorption cross section σ_{abs} at T=0:

$$\sigma_{decay}(E_\gamma) = \sigma_{abs}(E_\gamma)\frac{\rho(E^*_{fin})}{\rho(E^*_{in})} = \sigma_{abs}(E_\gamma)\exp(-E_\gamma/T) \tag{1.19}$$

where ρ is the level density, E_γ is the energy of the γ transition and T the average temperature. The absorption cross section has the Lorentzian shape of eq. 1.13. If the excitation energy E* is higher than the particle binding energy, the γ-decay process is in competition with the decay of particles, mainly neutrons in the case of stable nuclei. At the thermal equilibrium, the neutron evaporation cross section can be parametrized using the Maxwell-Boltzman distribution:

$$\sigma_n \sim T^2\exp((E_n - B_n)/T) \sim T^2\exp((-B_n)/T) \tag{1.20}$$

being B_n the neutron binding energy. So, the branching ratio between a γ ray of energy E_γ and n decay, whatever is the neutron energy, is:

$$\frac{\sigma_\gamma}{\sigma_n}(E_\gamma) \sim \sigma_{abs}T^{-2}\exp(-(E_\gamma - B_n)/T) \tag{1.21}$$

From the eq. 1.21 we can deduce that: if $E_\gamma > B_n$, the emission probability for a high-energy γ-ray increases with T: the emission of high-energy γ-ray occurs preferably at high temperature, therefore in the first steps. If $E_\gamma < B_n$, the γ-emission probability decreases with T: σ_γ is dominated by the last decay-steps, i.e. at low temperature.

IVGDR γ decay can occur after different neutron emissions as long as the excitation energy is higher than the Yrast line plus the energy of the resonance (in general more than 10 MeV). For this reason, the IVGDR can originates not only from the CN but also from all the nuclei populated in the de-excitation chain. However, gamma rays with energy $E_\gamma > B_n$, are preferentially emitted in the first few steps of the de-excitation chain. In the region between the neutron binding energy and the yrast line, manly statistical E1 emission (however GDR decay) occurs. After that, the de-excitation can happen with low energy E_2 emission along the Yrast line and the γ multiplicity depends principally on the initial angular momentum. The study of nuclear structure starting from the interpretation of a measured gamma spectrum is not straightforward:

- For a given $(E, J)_{init}$ the γ spectrum has contribution from all populated nuclei.
- The properties of the CN depend on J_{init} which is almost constant during the de-excitation process because most of the angular momentum is carried

off in the final stage, after the nucleus has already cooled down at energies around the Yrast line.

- If J_{init} is sufficiently high the analysis is complicated by the fission process.

In figure 1.8 a γ-decay spectrum from the reaction $^{16}O + {}^{118}Sn$ is shown. It is characterized by the presence of three different parts, all decreasing approximately exponentially:

- In the energy region $E_\gamma \leq 8$ MeV the spectrum is dominated by statistical γ decay from the lasts steps when the nucleus is already cooled down below the neutron binding energy. The relatively steep slope reflects the dominant effect of the level density.
- For $10 \leq E_\gamma \leq 25$ MeV the spectrum is manly due to statistical decay of IVGDR.
- The component visible for $E_\gamma \geq$ 30-35 MeV, is due to nucleon-nucleon bremsstrahlung, emitted during the initial stage of the collision.

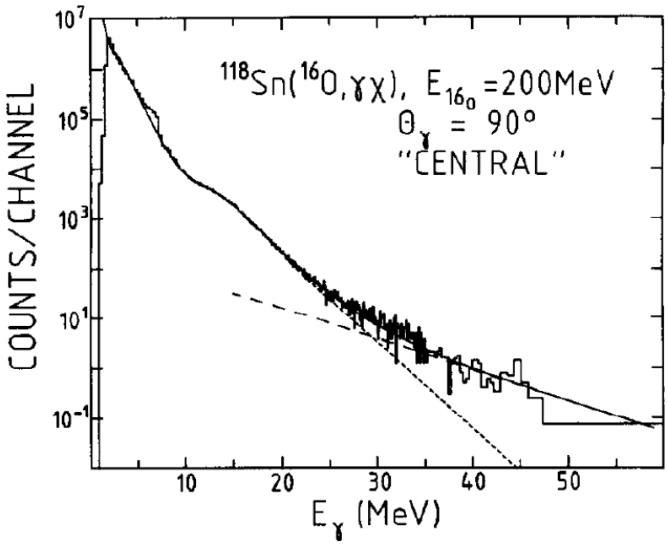

Figure 1.8: γ-ray spectrum from the fusion-evaporation reaction $^{16}O + {}^{118}Sn$ with a beam energy of 200 MeV. The full line corresponds to a fit to the data obtained by the sum of the Bremsstrahlung component and the CN decay component (long dashed line and short dashed line respectively) (19).

1.3 Isospin Symmetry

1.3.1 Introduction

The isospin concept begins in 1932, when Heisenberg (18) introduced an additional variable, the isospin, to specify whether a particle in the nucleus is a proton or a neutron. He noticed that the clustering of stable light and medium weight nuclei about $N \approx Z$ implied the symmetry of the basic nuclear force. Heisenberg assumed that the neutron-proton force was the main source of binding and that the electrostatic repulsion between protons was the main source of asymmetry in the nucleus. In the following years many experiments to study the charge independence of nuclear force were performed, as np and pp scattering and some indirect measurements of nn scattering. The charge independence statements says that the pp, nn and pn forces are equal to each other in the same space-spin states. Instead, the charge symmetry is a weaker statement that affirm that the nn and pp forces are identical, it makes no assertions about the np force. It is known that the Coulomb force breaks both of these symmetries. It is therefore generally assumed that the validity of charge independence and charge symmetry can only be expected for adronic forces, in the absence of all electromagnetic effects. Because electromagnetic effects are characterized by the fine structure constant α, we expect these symmetries to be valid to within a few percent. Nature does not allow us to " turn off " the charge of the proton, so that we are forced to remove the electromagnetic effect theoretically. The major effect is due to the static coulomb force, which is weak compared to the nuclear force.

1.3.2 Isospin formalism

In the isospin formalism, neutron and proton are considered as two states of a nucleon, as an "isospinors" with components:

$$\chi_n \equiv \begin{pmatrix} 1 \\ 0 \end{pmatrix} \qquad \chi_p \equiv \begin{pmatrix} 0 \\ 1 \end{pmatrix} \tag{1.22}$$

The isospin operators **I** and $I^2 = I_x^2 + I_y^2 + I_z^2$ have the properties under rotation completely analogous to those of the spin (6). In analogy with a spin 1/2 particle, which has two states, the nucleon has an isospin value of I=1/2 and neutron and proton are two different projection I_z of the isospin operator, with value +1/2 and -1/2, respectively. If we consider a system with A nucleons, namely the nucleus, the I_z values correspond to half the difference between the number of neutron (N) and proton (P):

$$I_z = \frac{N - Z}{2} \tag{1.23}$$

and the possible total isospin values associated to the nuclear state are:

$$|I_z| \leq I \leq \frac{N+Z}{2} \tag{1.24}$$

The nuclear force prefers the states with the lowest possible isospin value, therefore the isospin of the nuclear ground state is generally $I_0 = |I_z|$. An exception to this rule, which holds well for even-even and odd-mass nuclei, are some odd-odd nuclei like ^{34}Cl, ^{42}Sc, ^{46}V, ^{50}Mn, ^{54}Co, ^{62}Ga and ^{70}Br where $I_z = 0$ and I(g.s.) $= 1$ (20). The condition which guarantees the charge independence of nuclear force is that the total isospin commutes with the Hamiltonian, for which we have

$$[H, I] = 0 \qquad or \qquad [H, I^2] = 0 \tag{1.25}$$

that implies the invariance of the nuclear forces under rotation in charge or isospin state.

1.3.3 Evidence for charge independence and charge symmetry

Low energy pp and np scattering were the first experiments that have shown the charge independence, whilst the first evidence of charge symmetry came with the study of mirror nuclei through beta-decay (21). Indeed, the two nuclide ^3H and ^3He showed that the ground state energy difference could be accounted for by extra Coulomb potential energy in ^3He. Afterward, in order to study the two symmetries two primary techniques were developed: a) a search for reactions that are forbidden by isospin selection rules, and b) careful comparison of cross sections related through rotations in isospin space.

1.3.4 Isospin in electromagnetic transitions

In order to obtain the isospin selection rules for the electromagnetic transition, let's start from writing the width of a gamma-decay from state "a" to state "b" in terms of nuclear matrix element:

$$\Gamma_\gamma(L) = 8\pi k \sum_{M,M_b} |\langle J_b M_b; I_b I_{zb}|H(L,M)|J_a M_a; I_a I_{za}\rangle|^2 \tag{1.26}$$

where the interaction H(L,M) is given by:

$$H(L,M) = \int \frac{1}{c}\mathbf{j}_N(\mathbf{r})\mathbf{A}^*_{LM}(k\mathbf{r})d\tau \tag{1.27}$$

$\mathbf{j}_N(\mathbf{r})$ and $\mathbf{A}^*_{LM}(k\mathbf{r})$ are the nuclear current density and the vector potential of the electromagnetic field, respectively. Introducing the isospin formalism we can

write the current density as sum of two components, the isovector part $\mathbf{j}_N^{(1)}$, linearly dependent on I_z and the isoscalar one $\mathbf{j}_N^{(0)}$, independent of I_z:

$$\mathbf{j}_N = \mathbf{j}_N^{(0)} + \mathbf{j}_N^{(1)} \tag{1.28}$$

It is therefore useful to split in the same way the transition matrix element:

$$\langle J_b M_b; I_b I_{zb} | H_0(L,M) + H_1(L,M) | J_a M_a; I_a I_{za} \rangle \tag{1.29}$$

From the Wigner-Eckhart theorem we can extract the I_z dependence as follow:

$$\begin{aligned} &\langle J_b M_b; I_b I_{zb} | H_0(L,M) + H_1(L,M) | J_a M_a; I_a I_{za} \rangle = \\ &= (-1)^{I_b - I_{zb}} \begin{pmatrix} I_b & 0 & I_a \\ -I_{zb} & 0 & I_{za} \end{pmatrix} \langle J_b M_b; I_b | H_0 | J_a M_a; I_a \rangle \\ &+ (-1)^{I_b - I_{zb}} \begin{pmatrix} I_b & 1 & I_a \\ -I_{zb} & 0 & I_{za} \end{pmatrix} \langle J_b M_b; I_b | H_1 | J_a M_a; I_a \rangle \end{aligned} \tag{1.30}$$

Both isoscalar and iscovector terms do not vanish only if $I_{za} = I_{zb}$, therefore the first selection rule for the electromagnetic transition is:

$$\Delta I_z = 0, \tag{1.31}$$

which formalizes that an electromagnetic transition cannot occur between different nuclei. The Wigner coefficients in eq. 1.30 allow us to deduce another isospin selection rule:

$$\Delta I = 0, \pm 1 \tag{1.32}$$

Indeed,

$$(-1)^{I_b - I_z} \begin{pmatrix} I_b & 0 & I_a \\ -I_z & 0 & I_z \end{pmatrix} = (2I_a + 1)^{-\frac{1}{2}} \delta_{I_b I_a} \tag{1.33}$$

and

$$\langle J_b M_b; I_b | H_0 | J_a M_a; I_a \rangle = (2I_a + 1)^{\frac{1}{2}} \langle J_b M_b | H_0 | J_a M_a \rangle \tag{1.34}$$

point out that the isoscalar contribution vanishes except for I $\rightarrow$ I transitions. The Wigner coefficient that enters the isovector part contribution has the property for $T_a = T_b \pm 1$:

$$\begin{aligned} (-1)^{I_b - I_z} \begin{pmatrix} I_b & 1 & I_a \\ -I_z & 0 & I_z \end{pmatrix} &= (-1)^{I_b + I_z} \begin{pmatrix} I_b & 1 & I_a \\ I_z & 0 & -I_z \end{pmatrix} \\ &= (-1)^{I_b - I_a} \left[\frac{I_>^2 - I_z^2}{I_>(2I_> - 1)(2I_> + 1)} \right]^2 \end{aligned} \tag{1.35}$$

where $I_>$ is larger of I_a and I_b. We can note from eq 1.30 that similar $\Delta I = \pm 1$ transitions in conjugate nuclei are identical in all properties-strengths, mixing, ratios, phases. It is important to underline the following consideration: in long-wavelength limit ($k_\gamma r$), the E1 operator is fully isovector. This is clear by writing the charges of proton and neutron in terms of the nucleon isospin (4):

$$\sum_{i=1}^{A} q_i \vec{r}_i = \sum_{i=1}^{A} \frac{(1 - I_{zi})}{2} \vec{r}_i = \frac{1}{2}\vec{R}_{com} - \frac{1}{2}\sum_{i=1}^{A} I_{zi}\vec{r}_i \tag{1.36}$$

in which we assumed the proton and neutron masses are equal. The first term, the isoscalar part, is the nuclear center of mass coordinate, therefore it cannot produce Coulomb excitations (it is responsible for Thompson scattering). So in this approximation the E1 operator allows only isovector transitions. It follows the rule:

ΔI=0 for E1 transitions in self-conjugate nuclei are forbidden.

Because only $\Delta I = 1$ transitions can occur, the total E1 strength is reduced. As explained in the previous paragraph the γ decay of the GDR has an E1 character. Thus in self-conjugate nucleus the γ decay yield is strongly reduced. It is worth noting that only the first step of the γ decay is inhibited. In fact, after a proton or a neutron evaporation (which is the favorite decay) a self-conjugate nucleus is no more self-conjugate in a $I_z = 0$ state and thus also isoscalar $\Delta I = 0$ transition can occur.

1.3.5 Isospin mixing

As described previously, the isospin symmetry is largely preserved by strong interaction, even if a small violation of the symmetry on the hadronic level is due to the difference in the masses of the up and down quarks (22). In atomic nuclei, the main source of isospin breaking is the electromagnetic interaction and since it is much weaker than the strong interaction between nucleons, many effects associated with isospin breaking in nuclei can be treated in a perturbative way. Inside a nucleus, two competitive trends occur: the nuclear force is strongly attractive in the isoscalar p-n channel, while the Coulomb force acts against this attraction by making neutron and proton states different (3). Let's start writing the Coulomb potential in the isospin formalism:

$$V_c = \sum_{i<j} \left(\frac{1}{2} - I_z^i\right)\left(\frac{1}{2} - I_z^j\right)\frac{e^2}{r_{ij}} \tag{1.37}$$

that can be written as the sum of an isoscalar $V_C^{(0)}$, isovector $V_C^{(1)}$ and isotensor $V_C^{(2)}$ terms:

$$V_c^{(0)} = \sum_{i<j} \frac{1}{4}\frac{e^2}{r_{ij}} \left(1 + \frac{4}{3}\mathbf{I}^i\mathbf{I}^j\right),$$
$$V_c^{(1)} = -\sum_{i<j} \frac{1}{2}\frac{e^2}{r_{ij}} \left(I_z^{(i)} + I_z^{(j)}\right), \tag{1.38}$$
$$V_c^{(2)} = \sum_{i<j} \frac{1}{4}\frac{e^2}{r_{ij}} \left(4I_z^{(i)}I_z^{(j)} - \frac{4}{3}\mathbf{I}^i\mathbf{I}^j\right).$$

From Eq.1.38 we can deduce that the contribution to isospin breaking comes only from the Isovector and Isotensor terms, inducing impurities in the nuclear wave function with $\Delta I = 1$ and $\Delta I = 2$ respectively. The isoscalar term has indeed, no effects. A consequence of these impurities is the inducing of mixing between different isospin, namely the nuclear state must be described as a superposition of two or more states with different isospin. In first order perturbation theory, the probability to have admixture of $I = I_0 + 1$ states into $I = I_0$ ones, the α^2, is defined as:

$$\alpha^2 = \sum_{I_0+1 states} \frac{|\langle I = I_0 + 1|V_c^{(1)}|I_0\rangle|^2}{(E_{I_0+1} - E_{I_0})^2} \tag{1.39}$$

Inside nuclei, the Coulomb potential varies very slowly and it preserves angular momentum and parity. From Eq. 1.39 we can deduce that a large matrix element can occur only between states with very similar spatial wavefunctions and of same J^π. Moreover, because of the denominator, the isospin mixing probability is important only between states close together in energy. To sum up, the isospin mixing is large only between nearby states having the same spin and parity and a large overlap between their spatial wave functions. Because of the tensor part induces mixing with $\Delta I = 2$ states that lye much higher in energy than $\Delta I = 1$ ones, this part is neglected. The mixing coefficient of a nucleus gives information on how much the isospin is a good quantum number. In the past years many theoretical calculations of the isospin mixing in the ground state were performed using several approaches. In a work by Satula reported in (3), the Energy Density functional approach was used to deduce the isospin mixing mass dependence and as expected, the α^2 value increases with the mass number, since the Coulomb interaction increases as shown in figure1.9. In the case of ^{100}Sn, which is the heaviest $N = Z$ nucleus existing in the nuclear chart, the α^2 is largest.

Effect of increasing energy

At the increasing of the excitation energy, states start to lie close together and if they are above the particle threshold, also acquire a finite particle decay width.

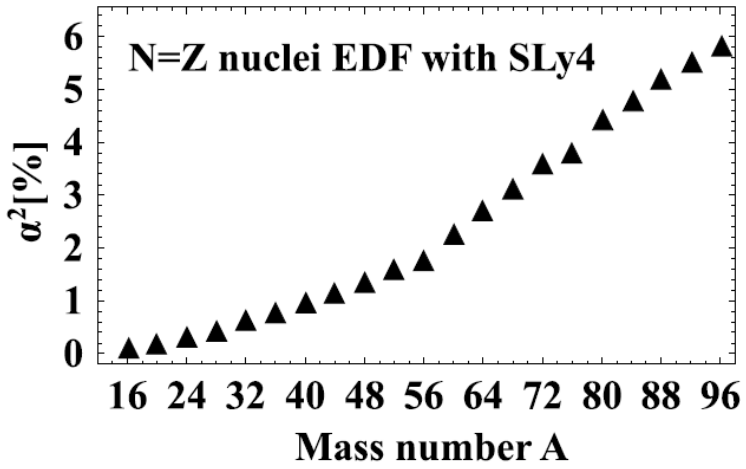

Figure 1.9: Degree of mixing α^2 in the ground states for $N = Z$ nuclei, obtained using an Energy Density Functional approach and a SLy4 nuclear interaction (3).

The decay probability increases exponentially with excitation energy caused by the opening of decay channels. The previous equation will be, therefore, generalized in the following expression considering the complex energy (4):

$$\alpha^2 = \sum_{I_0+1 states} |\frac{\langle I = I_0 + 1|V_c^{(1)}|I_0\rangle}{(E_{I_0+1} + i\frac{\Gamma_{I=I_0+1}}{2}) - (E_{I_0} + i\frac{\Gamma_{I=I_0}}{2})}|^2 \tag{1.40}$$

where Γ is the total particle decay width. From the denominator of the expression, it turns out that if the width were negligible, the mixing coefficient would increase as the level density decreases as in eq. 1.39. However, since Γ becomes important with the excitation energy, namely in the region of overlapping levels, one expects to have the maximum of α^2 when the level spacing and the decay width are similar. In 1955, Wilkinson (6) and Morinaga (23) proposed a time dependent approach to describe the behaviour at high excitation energy instead of a time independent model as describes the equation 1.40. They suggested that the time independent nuclear states themselves don't have a good isospin, but that a given reaction can form a compound nuclear wavefunction that is initially a superposition of defined isospin states. At high excitation energy, the compound nuclear decay width becomes large, overwhelming the Coulomb interaction matrix element; thus, the nucleus decays before the isospin degrees of freedom have time to equilibrate. We have, therefore, the restoration of the symmetry. This implies a dynamical behavior between the Coulomb interaction time-scale and the compound nucleus

lifetimes (4). In order to better understand this concept, it is useful to describe the effect of the Coulomb interaction not in terms of a matrix element, but in terms of a spreading width, whose meaning is illustrated introducing the following picket fence model. Imagine, in a plus to minus infinity space, a certain number of I=0 states with the same level spacing energy D and a state of good isospin T=1 lies in their midst at energy $E_{T=1}$. If we consider a perturbation with a constant matrix element v between this state and each of the underlying state, it is possible to solve analytically the Hamiltonian matrix. The probability $P_{I=1}[E]$ of the I=1 configuration per unit energy interval, in the limit of v»D is given by a Breit-Wigner distribution (24):

$$P_{I=1}[E] = \frac{1}{2\pi}\frac{\Gamma^{\downarrow}}{(E_{I=1}-E)^2+(\frac{\Gamma^{\downarrow}}{2})^2} \qquad \Gamma^{\downarrow} = \frac{2\pi v^2}{D} \tag{1.41}$$

In a time dependent space, we can describe the amplitude $A_{I=1}[t]$ at the time t of finding the system initially populated in the I=1 state still in the I=1 state by the Fourier transform of Eq 1.41:

$$A_{I=1}[t] = exp(-\frac{\Gamma^{\downarrow}}{2\hbar}t - \frac{i}{\hbar}E_{I=1}t) \tag{1.42}$$

from where one can deduce a relation that links the Coulomb spreading width and the timescale of isospin mixing:

$$\tau_{mixing} = \frac{2\hbar}{\Gamma^{\downarrow}} \tag{1.43}$$

Parametrization of Harney, Richter and Weidenmüller

Harney, Richter and Weidenmüller proposed a model that allows to describe at the same time the compound nucleus system and the isospin formalism, incorporating the isospin mixing in the statistical model. With this formalism, it is possible to describe a reaction with the entrance channels of two different isospins and exit channels of two different isospins, with mixing allowed between the two isospin classes in the compound nucleus, through the use of the S-matrix. They assumed no mixing before the compound nucleus formation and that the only states with the same angular momentum and parity can be mixed, because of the conservation of angular momentum and parity. The Coulomb spreading width, for the state $I_< = I_z$ can be expressed in terms of the Coulomb matrix element, averaged over

all possible states, linking the $I_<$ and $I_>$ $(= I_z + 1)$ states at given energy and angular momentum:

$$\Gamma^{\downarrow}_{<} = 2\pi\overline{|\langle I_>|H_c|I_<\rangle|^2}\rho[I_>] \tag{1.44}$$

Moreover, this statistical mixing model assumes mixing only between states at the same excitation energy, for this reason, the Coulomb matrix element will be the same for the $I_>$ states at the same energy, so that

$$\Gamma^{\downarrow}_{<} = \frac{\rho[I_>]}{\rho[I_<]}\Gamma^{\downarrow}_{>} \tag{1.45}$$

In their formalism the isospin mixing term is expressed with a single parameter z

$$\begin{aligned} z = 4\pi^2\overline{H_c^2}\rho[I_<]\rho[I_>] = \\ 2\pi\Gamma^{\downarrow}_{>}\rho[I_>] = \\ 2\pi\Gamma^{\downarrow}_{<}\rho[I_<] \end{aligned} \tag{1.46}$$

and using this equation, it is possible to derive the fraction $\alpha^2_>$ of states $I_>$ which mix with $I_<$ states

$$\alpha^2_> = \frac{\Gamma^{\downarrow}_{>}/\Gamma_>}{1 + \Gamma^{\downarrow}_{>}/\Gamma_> + \Gamma^{\downarrow}_{<}/\Gamma_<} \tag{1.47}$$

and similarly the fraction $\alpha^2_<$ of states $I_>$ which mix with $I_<$ states

$$\alpha^2_< = \frac{\Gamma^{\downarrow}_{<}/\Gamma_<}{1 + \Gamma^{\downarrow}_{<}/\Gamma_< + \Gamma^{\downarrow}_{>}/\Gamma_>} \tag{1.48}$$

where $\Gamma_{>(<)}$ is the total decay width of the states $I_{>(<)}$.
For small mixing, the previous equation is reduced to

$$\alpha^2 \approx \frac{\Gamma^{\downarrow}}{\Gamma} \tag{1.49}$$

and this confirms the Wilkinson hypothesis that, at finite excitation energy, the mixing degrees should depend only on the ratio between the time scale characterizing the isospin mixing process and the CN decay. With increasing temperature, CN lifetime becomes too short (and thus Γ large) to allow a complete mixing, therefore a decrease of isospin mixing parameter is expected, corresponding to a partial restoration of isospin symmetry at high temperature. For larger mixing degrees, also the correction in the denominator, that give the probability that $I_>$ states mix back to $I_<$ has to be taken into account.

Isospin mixing temperature dependence

The isospin symmetry restoration at high excitation energy, proposed by Wilkinson, was successively studied also by Sagawa, Colò and Bortignon (2) using a microscopic model. This model is based on the Feshbach projection method and gives an explicit relation between the spreading width of the IAS and the isospin mixing probability in excited compound nuclei. The authors, indeed, assume that the Coulomb spreading width of a CN is the same as that of the corresponding IAS, because both are originated by the isospin mixing. Moreover, the temperature dependence of isospin mixing is described. In order to describe the mixing probability let's start from the Coulomb spreading width of the IAS:

$$\Gamma^{\downarrow}_{IAS} = \Gamma^{\downarrow}_{C}(E^*) + \Gamma_M(E^*)\alpha^2_{T_0+1}(T_0+1) \tag{1.50}$$

and thus the mixing probability is given by:

$$\alpha^2_{T_0+1} = \frac{1}{T_0+1}\frac{\Gamma^{\downarrow}_{IAS}}{\Gamma_C(E^*)+\Gamma_M(E_{IAS})} \tag{1.51}$$

where $\Gamma_C(E^*)$ is the compound nucleus decay width, $\Gamma^{\downarrow}_{IAS}$ is the Coulomb spreading width of the IAS and $\Gamma_M(E_{IAS})$ is the width of the Isovector Monopole Resonance (IVM) at the excitation energy of the IAS. This quantity has to be considered as a parameter of the model, because is impossible to measure experimentally. Whilst, the compound nucleus decay width is expected to increase with temperature, on the other hand, the other two widths don't have a strong temperature dependence. As one can see in figure 1.10 for the case of ^{208}Pb, the mixing probability remains nearly constant with the temperature up to about 1 MeV and then decreases down to around $1/4$ of its zero temperature value, because of the short lifetimes of the compound system, at temperature higher than about 3 MeV. The slight temperatures T dependence has been parametrized as:

$$\Gamma^{\downarrow}(T) = \Gamma(T=0)(1+cT) \tag{1.52}$$

where the parameter c should be determined through a microscopic calculation.

1.3.6 Isospin mixing beyond nuclear structure: The CKM matrix

Studies concerning isospin symmetry breaking are not only important for nuclear structure. The isospin mixing parameter, indeed, is one of the ingredients of the first term of the Kabibbo-Kobaiashi-Maskawa matrix. In the standard model (SM) this matrix contains information about the transitions between quarks due to the weak force. Because it is hypothesized to be unitary, testing this property is important for the validity of the SM. The first element V_{ud} of the CKM provides

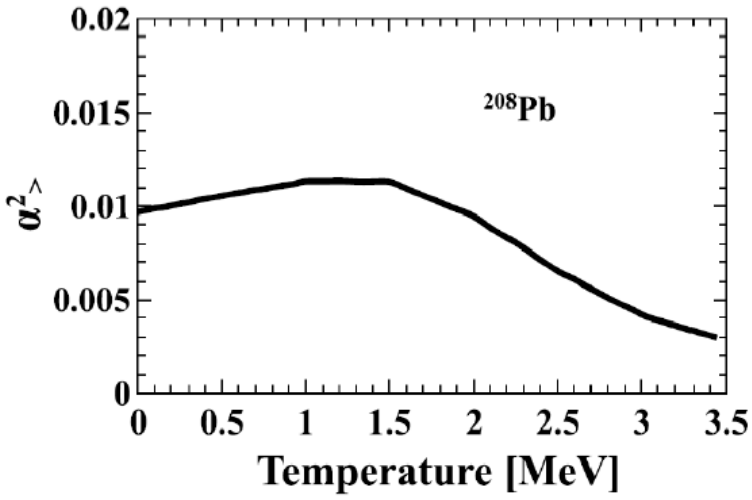

Figure 1.10: Temperature dependence of the isospin mixing probability for the nucleus ^{208}Pb. (2).

the coupling between the quarks u and d, which is the basis of the β-decay transitions in nuclei. The V_{ud} value can be obtained from the *ft* values of $0^+ \rightarrow 0^+$ superallowed Fermi β transition:

$$ft = \frac{K}{G_V^2 |M_F|^2} \tag{1.53}$$

where $\frac{K}{(\hbar c)^6} = \frac{2\pi^3 \hbar \ln 2}{(m_e c^2)^5} = (8120.2707 \pm 0.0011) * 10^{-10}\ GeV^{-4}s$, G_V is the vector coupling constant obtained from semileptonic weak interaction and M_F is the Fermi matrix element.
The Conserved Vector Current (CVC) hypothesis indicates that the *ft* values should be the same irrespective of the nucleus (25). Actually, in the expression one must consider two further effects: first, there are radiative corrections, for example bremsstrahlung photon emitted by electrons and second, the isospin is not an exact symmetry. Therefore, the nuclear matrix element is slightly reduced from its ideal value:

$$|M_F|^2 = |M_0|^2 (1 - \delta_C) \tag{1.54}$$

where M_0 is the value assuming isospin symmetry. Thus the "correct" *Ft*:

$$Ft = ft(1 + \delta_R)(1 - \delta_C) = \frac{K}{2G_V^2 (1 + \Delta_R^V)} = const, \tag{1.55}$$

where δ_C is the isospin-symmetry breaking correction, δ_R is the transition dependent part of the radiative correction and Δ_R^V is the transition-independent part. From Ft one can in principle extract the value of G_V and thus V_{ud} form the relation $V_{ud} = \frac{G_V}{G_F}$ where G_F is the well known the weak interaction constant. In practice, it is important to take many values of Ft coming from nuclei in different mass region, then if they are statistically consistent the two values can be extracted from the average of Ft. To do this, it is important to have a good estimation of the correction terms (25). The isospin-symmetry breaking correction, is unfortunately not directly measurable and many theoretical approaches are used to parametrized its behaviour along to the mass number (26). N. Auerbach (27) proposed a simple analytic relation between the δ_c and the isospin mixing probability:

$$\delta_C = 4(I+1)\frac{V_1}{41\xi A^{\frac{2}{3}}}\alpha^2 \tag{1.56}$$

where $V_1 = 100$ MeV and $\xi = 3$, while α^2 is the isospin impurity in the ground state and I the isospin of the nucleus.
In figure 1.11 the uncorrected *ft* values for twelve super-allowed decay are shown and compared after application of correction terms.
In figure 1.12 the experimental values of δ_C along to the mass number in comparison with two theoretical calculations are presented. The experimental values were obtained using the β-decay ft (28) and the mass measurement in the case of ^{74}Rb (29). It is worth to note that these experimental values were obtained using Eq 1.55 assuming the other known quantities and considering Ft as an adjustable parameter equal for all nuclei. This method is limited by the precision in the *ft* measurement (especially for short lifetime) and because it assumes valid the constance of Ft.

1.3.7 Experimental methods and recent results

After the description of the isospin mixing phenomenon from a theoretical point of view by Morinaga and Wilkinson, many experimental methods were developed to measure the effect. All techniques are based on the identification of transitions that would be forbidden if the isospin was a good quantum number to describe the nucleus, for example β-transitions among nuclei with different isospin (30) or E1 transitions, and thus the γ-decay of the IVGDR, in self-conjugate nuclei (31, 4, 32, 33, 34, 35, 36, 37). In the present work, the γ decay of the GDR was used to probe the isospin mixing effect. In particular, the experimental method concerns the measurement of an E1 decay forbidden by the selection rules of the isospin symmetry. By measuring the γ-decay of the IVGDR, built on a CN state, and fitting such data with the statistical model (in which the formalism proposed by Harney, Richter and Weidenmuller is included) it is possible to obtain the value

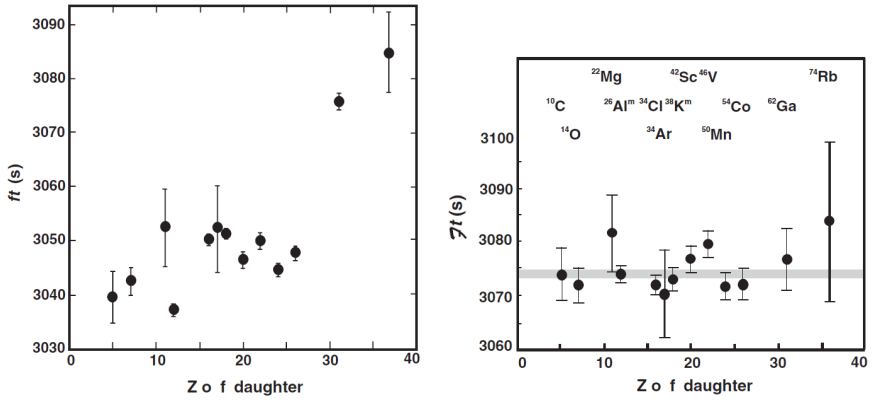

Figure 1.11: In the left panel, the uncorrected ft values for twelve superallowed decay, compared after application of correction terms in right panel. The grey band is the average value including its uncertainty. (25)

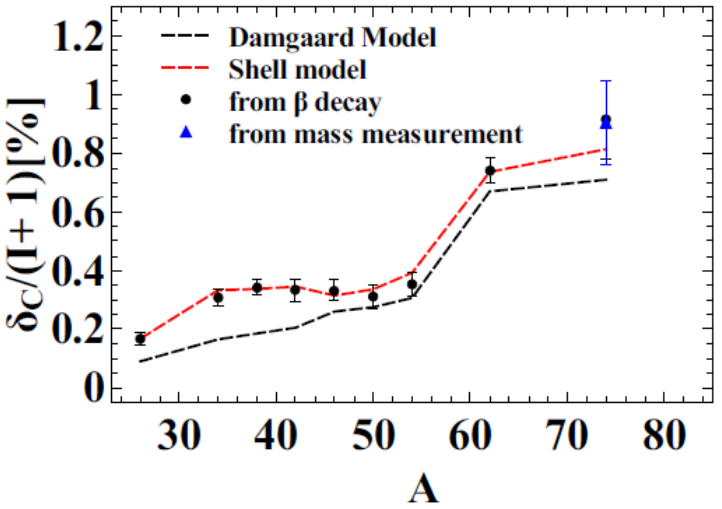

Figure 1.12: Isospin mixing correction as a function of the nuclear mass number. The dashed black line is the prediction from the Damgaard model (38), while the red line is a shell model with Saxon-Woods radial wave function prediction (39). Black circles are the experimental points extracted from β-decay as reported in Ref. (28), the blue triangle is the value obtained from the mass measurement in Ref. (29)

.

of α^2, the mixing degree, and the Coulomb spreading width Γ at the temperature value T of the CN. This technique has been proposed firstly in (31) by Harakeh, who studied the γ emission from the hot nuclei $^{28}Si^*$ and $^{24}Mg^*$ populated using a fusion-evaporation reaction. This type of studies was continued also by the Milano Group with two works (by Simone Ceruti (32) and Anna Corsi (33)). They measured the isospin mixing in the nucleus ^{80}Zr at two different temperatures, to describe the trend of the symmetry breaking with nuclear excitation energy. In these works, the theoretical model proposed by Sagawa, Bortignon and Colò(2) was used to extract the mixing probability for the nucleus ^{80}Zr at T=0, starting for the two values of α^2 at finite temperature. The mixing probability, together with the Coulomb spreading width, was determined at $T \approx 3$ MeV ($\alpha^2_> = 1.3\% \pm 0.4\% (J = 0), \Gamma^{\downarrow} = 10 \pm 3$) keV in (33) and at $T \approx 2$ MeV ($\alpha^2_> = 4.6\% \pm 0.7\% (J = 0), \Gamma^{\downarrow} =$ 12±3 keV) in (32). From the two results it was deduced that the Coulomb spreading widths are in good agreement and that they are rather independent from the nuclear temperature (32). Using the model described in the previous paragraph, the isospin mixing at T=0 temperature (and J=0) was deduced with a value of 4.6%±0.9% in good agreement with the theoretical prediction reported in (3) , which represents a good evidence for the validity of the theoretical model. In figure 1.13 the gamma spectrum for both Milano measurements are shown, compared with the statistical model calculation whilst, in figure 1.14, the isospin mixing parameter obtained experimentally is compared with the theoretical value.

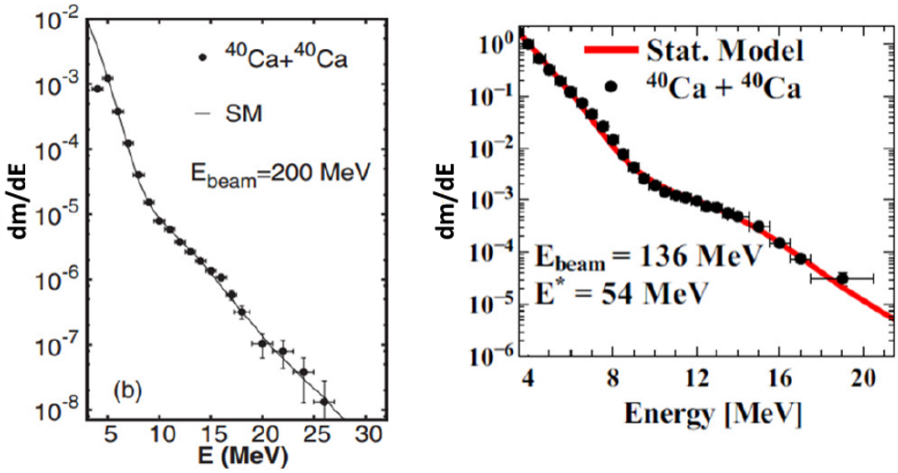

Figure 1.13: In the left panel the γ-spectrum of ^{80}Zr at T≈3 MeV (33). In the right panel the γ-spectrum of ^{80}Zr at T≈2 MeV (32). The experimental data (the black dots) and the statistical model calculation (the lines) are compared.

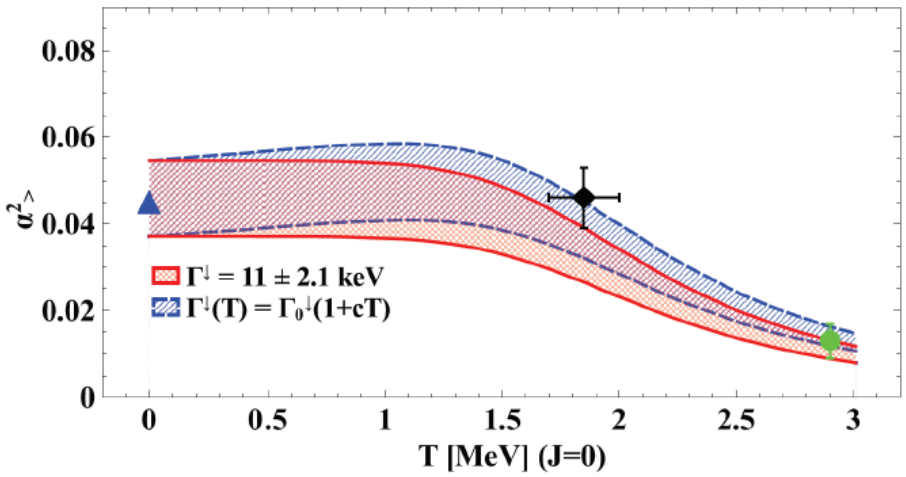

Figure 1.14: Isospin mixing as a function of temperature (as in eq. 1.51) obtained with the procedure in (2). The red band correspond to the average value of Coulomb spreading width $\Gamma^{\downarrow} = 11 \pm 2.1$ keV obtained from (33) and(32) and considered constant with T. For the blue band, $\Gamma^{\downarrow}$ vary slightly and linearly with T (as in 1.52). The blue triangle is the theoretical value at T=0, defined in (3), the green circle is the datum from (33) and the black diamond is obtained from (32). Figure taken from (32).

Part II

Isomix in mass A=60

CHAPTER 2

The experiment

Life is trying things to see if they work.

Ray Bradbury

For the study of isospin at finite temperature at A=60 (^{60}Zn), two sets of experiments were performed. In this chapter we will explain the details of the experimental Set1 corresponding to the experiment carried out in June 2016 at Laboratori Nazionali di Legnaro. We will describe the experimental methods, the set up composed by four different arrays of detectors and the data acquisition system. Then we will move to the data analysis and the results of the experiment.

2.1 Description of the experiment - SetI

As previously described, the way we used to determine the isospin mixing coefficient, is to study a γ - decay that would be forbidden by the selection rules of the isospin symmetry if isospin were a good quantum number. Let's assume that we are able to form a compound nucleus in a I=0 excited state. For the selection rules of the symmetry, as described in 1.3.4, electric dipole transitions in the long wavelength limit are forbidden between states of the same isospin, thus, the nucleus can't decay to a state of I=0 but it can decay to a state of I=1. The density of T = 0 levels is always higher than the density of T= 1 levels. Therefore, if compound nuclear isospin is pure, the production of high energy γ-rays in T= 0 compound nuclear entrance channels should be reduced compared to T $\neq$ 0 entrance channels (31). So, from the experimental point of view, the γ decay should be barely visible. The scheme described is reported in figure 2.1a. Now, if we assume the breaking of the symmetry and that the nucleus is formed in a state which is composed by the mixing of two states (at the first order), I=0 and I=1, a decay becomes possible.

The I=1 part of the initial state can decay to the I=0 state, as shown in figure 2.1b. The measurement of the yield of this decay provides information regarding the isospin mixing coefficient.

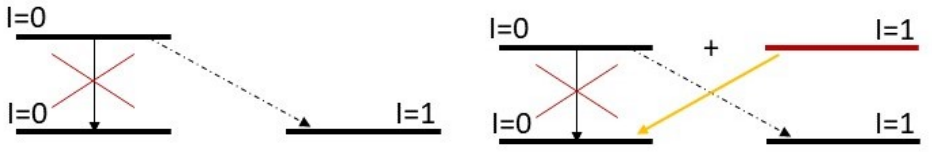

(a) Decay scheme without mixing. *(b) Decay scheme with mixing.*

Figure 2.1: Compound nucleus decay scheme, considering, in case (a) the validity of the symmetry and the isospin mixing effect in case (b).

The compound nucleus selected to study the mixing effect is the ^{60}Zn formed by a fusion-evaporation reaction, with a bunched beam of ^{32}S (intensity $\approx$ 2pnA) and a self-supporting target of ^{28}Si ($400\mu g/cm^2$):

$$^{32}S +^{28} Si \rightarrow^{60} Zn^* \tag{2.1}$$

We can notice that both the projectile and the target have, respectively, the same number of proton and neutron (N=Z), therefore, the nucleus of interest ^{60}Zn has also N=Z. This ensure that, supposing I=0 projectile and target, we are creating a nucleus in a I=0 state, the perfect probe to test the breaking of the symmetry. So, from an experimental point of view we expect to observe the E_1 decay (GDR) between the states with I=1 (due to the mixing effect in the initial state) and I=0. An other important point is to determine not only the value of the mixing coefficient but also its dependence from the nuclear temperature. Analysing the fusion cross sections and the beam energies available, as reported in (40), the following parameter were chosen to form the nucleus of interest at two different temperatures.
Because the isospin mixing probability is a quantity of the order of few per-cent, we need a second reaction, which is not affected by the mixing effect, to use as a reference. This reaction should create a very similar compound nucleus with very similar excitation energy and angular momentum but in a non zero state of Isospin. This reaction is used to tune the statistical model and to fix the GDR parameters.

$$^{32}S +^{30} Si \rightarrow^{62} Zn^* \tag{2.2}$$

In this case the beam intensity was approximatively the same and the thickness of the target was $250\mu g/cm^2$. The ^{62}Zn is an N$\neq$Z nucleus thus, it is formed in

$^{32}S + {}^{28}Si \rightarrow {}^{60}Zn^*$				
$E_{beam}[MeV]$	T[MeV]	$\sigma_{Fus}[mb]$	$E^*[MeV]$	$< J > [\hbar]$
86	2.1	487	47	14
110	2.4	884	58	21

Table 2.1: Beam energies $E_{beam}[MeV]$ and temperature values T[MeV], selected for the present work, with the corresponding fusion cross sections $\sigma_{Fus}[mb]$, CN excitation energies $E^*[MeV]$ and CN average angular momenta $< J > [\hbar]$ for the reaction $^{32}S + {}^{28}Si \rightarrow {}^{60}Zn^*$

$^{32}S + {}^{30}Si \rightarrow {}^{62}Zn^*$				
$E_{beam}[MeV]$	T[MeV]	$\sigma_{Fus}[mb]$	$E^*[MeV]$	$< J > [\hbar]$
75	2.1	312	47	11
98	2.4	815	58	20

Table 2.2: Beam energies $E_{beam}[MeV]$ and temperature values T[MeV], selected for the present work, with the corresponding fusion cross sections $\sigma_{Fus}[mb]$, CN excitation energies $E^*[MeV]$ and CN average angular momenta $< J > [\hbar]$ for the reaction $^{32}S + {}^{30}Si \rightarrow {}^{62}Zn^*$

an unknown state of isospin and the GDR γ-decay does not depend on the value of the isospin mixing. From the comparison between data from the two reactions, it is possible to eliminate the uncertainties related to the IVGDR and statistical model parameters. The parameters for the two reactions are shown in table 2.1 and 2.2.

The main part of the analysis is based on the comparison between the experimental data and the statistical model calculation (as described in section 6.1) that simulate the statistical decay of the compound nucleus. The main assumption is that the parameters to describe the decay of ^{60}Zn and ^{62}Zn are the same and such assumption is valid if the average temperature, the mass and the shape of the compound nuclei are similar. The condition on mass is ensured by choosing two CN with mass A=60 and A=62, that in the statistical process can be considered identical. The choice of the beam energies fulfils the condition on temperature as shown in table 2.1 and in 2.2. Under these condition we can consider the GDR parameters (strength, centroid energy and width) the same for both nuclei. The data analysis will be focused on the identification of residual nuclei that will be useful to verify that the experimental distribution is reproduced by the statistical model. After that, we can use the statistical model to obtain the GDR parameters

of the reference nucleus ^{62}Zn and for the reasons explained before, we can apply these parameters to the ^{60}Zn. In this way the only free parameter will be the isospin mixing coefficient.

2.2 Experimental set-up

A very complex experimental set-up was assembled in order to allow the measurement of both γ-rays and particles emitted during the decay of the compound nucleus. The set-up was composed by four different detectors arrays. The main part consisted in an array of 25 HPGe detectors, called GALILEO (41), coupled to an array of 10 $LaBr_3(Ce)$ scintillator detectors (42). In addition, an array of 40 Silicon detectors in $\Delta E - E$ telescopes configuration, EUCLIDES (43) was employed. Also an array of 15 BC501A scintillator detectors, named Neutron Wall (44) were installed in the set-up. A schematic picture of GALILEO coupled with $LaBr_3(Ce)$ detectors is shown in figure 2.2. As described in the previous part, in order to deduce the isospin mixing parameter, the GDR γ-decay must be measured. Thanks to the intrinsic time, energy resolution and detection efficiency for high energy γ-rays, large volume of $LaBr_3(Ce)$ detectors can provide, at the same time, clean spectroscopic information from a few tens of keV up to tens of MeV, being furthermore able to clearly separate the full energy peak from the first escape peak up to at least a γ-ray energy of 25 MeV (42). For this reason the $LaBr_3(Ce)$ array was chosen to measure the GDR γ-rays. This array is, indeed, the most important part of the experimental set-up for the purpose of this work on isospin mixing. On the other hand, we need to measure low energy γ-rays emitted during the de-excitation of the CN for the study of the populated residues nuclei. The energy of these γ-rays extends between tens of keV to 3-4 MeV. $LaBr_3(Ce)$ detectors are not "optimal" to measure these transitions because of their energy resolution(about 3% at ^{137}Cs that doesn't allow to clearly discriminate betweens discrete peaks). For this reason, the GALILEO Array was used, because of the very high energy resolution of the HPGe detectors which make possible the measurement of the populated residues. The identification of residual nuclei is the base for the test of the statistical model. EUCLIDES and Neutron Wall array should validate the GALILEO results, measuring charged particles and neutrons.

2.2.1 The GALILEO Array

The GALILEO Array is an Italian project, built with the purpose to be an advanced device in the field of nuclear structure studies performed with in-beam gamma-ray spectroscopy methods. This kind of research can be done with the available stable beams and, in the future, with radioactive beams which will be provided, in Italy,

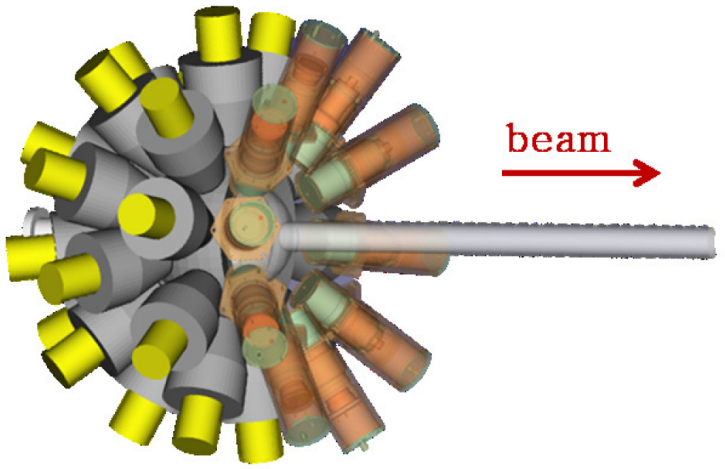

Figure 2.2: A scheme of GALILEO coupled with $LaBr_3(Ce)$ detectors.

by the facility SPES (45). GALILEO is a 4π high-resolution γ-array spectrometer (41) which will employ 30 GASP Germanium (Ge) tapered detectors together with their anti-Compton shield, and triple clusters of High-Purity Germanium (HPGe) detectors realized with the capsules of the previous EUROBALL Array. The geometry was designed to maximize the photo-peak efficiency under typical in beam medium-high (10-30) γ-ray multiplicity condition, achieving an efficiency value of about 8%. The Ge detectors are surrounded by anti-Compton shields in order to reach, for the whole array, a peak-to-total-ratio of about 50%. At the time of the experiment, the GALILEO Array was composed by 25 single GASP HPGe detectors (with anti-Compton shields), arranged on 4 different rings: 5 detectors placed at 152°, 5 at 129°, 5 at 119° and 10 at 90° with respect to the beam line. The detectors are placed at a distance of 22.5 cm from the target. A complete view (2.3a) and a front-view (2.3b) of the 25 GALILEO detectors are shown in figure 2.3

2.2.2 The $LaBr_3(Ce)$ detectors array

The $LaBr_3(Ce)$ is a scintillator with a large potential in γ-ray spectroscopy. It has, indeed, a high efficiency, a good energy resolution ($\approx 3\%$ at ^{137}Cs), excellent time resolution (< 1 ns depending on the size of the crystal) and a high light yield (63000 photons/MeV) (42). For this reasons, the $LaBr_3(Ce)$ detectors represent a suitable choice to measure high-energy γ-rays from fusion-evaporation reactions, where the γ-rays/neutrons discrimination is a crucial point. An array of 10 $LaBr_3(Ce)$ can be installed, coupled to the GALILEO array, in two different positions: in the

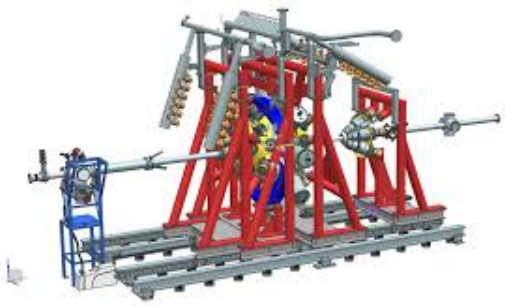

(a) Complete view of GALILEO Array.

(b) Front-view of the 25 GALILEO detectors.

Figure 2.3: A CAD picture of the complete GALILEO Array and a front-view picture of the HPGe detectors.

central ring (90°), removing 10 HPGe detectors, or at 70° with respect to the beam line. In this experiment the latter solution was used and $LaBr_3(Ce)$ detectors were placed at 20 cm from the target position. The signals coming from $LaBr_3(Ce)$ detectors were implemented into the GALILEO DAQ system through a half-analog and half-digital readout. The detector signals are sent to dedicated NIM module, called LaBr-pro and the shaped signals are sent to the digitizers. The time signals from LaBr-Pro are instead sent into a TAC module and then digitized. The digitizer channels associated to $LaBr_3(Ce)$ detectors were settled on an input range corresponding to an energy interval 0-40 MeV. The GALILEO digitizers are not optimized for $LaBr_3(Ce)$ detectors, for this reason we observed a slightly degradation of the energy resolution, passing from ≈24 keV at 661.7 keV(^{137}Cs) with the full analog system to ≈28 keV with digitalized signals. For our experiment, a very high energy resolution for $LaBr_3(Ce)$ is not mandatory, so we used the semi-digital acquisition.

2.2.3 EUCLIDES array

The Si 4π array EUCLIDES (EUropean Charged Light Ions DEtector Sphere), is a light charged particle ancillary array, inserted in the reaction chamber of GALILEO (43). It is made up of 40 two-stage $\Delta E - E$ telescopes arranged in a 42-face polyhedron composed of 30 irregular hexagonal and 12 regular pentagonal faces. Two pentagonal faces are used for the incoming and outgoing beam ports. ΔE and E silicon detectors have $\approx$ 130 μm and $\approx$ 1000 μm thicknesses. EUCLIDES with the whole support structures and cabling fits inside a 22 cm diameter reaction

chamber, as shown in figure 2.4.

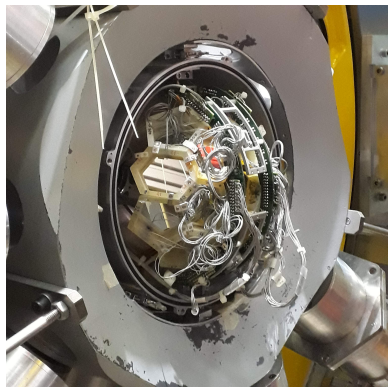

Figure 2.4: A picture of EUCLIDES array.

Through an extensive GEANT 4 simulation of the whole array, the optimal geometry was estimated with a solid angle coverage of $\approx 81\%$ and $\approx 80\%$ for ΔE and E, respectively. The light charge particles identification of EUCLIDES relies on the ΔE - E method. The energy detected in the thin ΔE detector is combined with the total energy loss in the E detector placed behind it. The energy loss process is described by the Bethe-Bloch expression (46) as a function of the atomic number and the mass of the incident particle, in the non-relativistic approximation. In order to have a good energy resolution, the E detector must be thick enough to stop the particle but even if the particle is not completely stopped it can be still identified using the energy released in the telescope. The high efficiency is guaranteed by a 4π solid angle and a high granularity. In a typical symmetric fusion-evaporation reaction, the compound nucleus has $v/c < 5\%$. Therefore, considering the kinematic enlargement of the solid angle in the laboratory reference frame, five of the forward-most positioned telescopes are segmented. The total sustainable counting rate for a forward telescope can be of ≈ 100 kHz. However this was never achieved in the experiment. The segmentation is also important to correct for the Doppler effect which occurs when particles are emitted in flight. Finally, Si telescopes and the holding structure do not cause large γ-ray absorption or scattering. The typical average energy resolution, using the 5.485 MeV alphas from an ^{241}Am source, is about 50 keV for the ΔE detectors with full depletion voltage ranging from 40 to 60 V. For the E detectors, due to their smaller capacitance, the typical energy resolution is about 30 keV with full depletion bias ranging from 120 to 200 V.

2.2.4 Neutron Wall Array

The Neutron Wall is an array composed by 15 hexagonal BC501A liquid scintillation detectors. They are mounted in the forward hemisphere of the GALILEO array and each of them is subdivided into 3 segments. There are 45 different segments in total with 6 different geometries, placed at 18.5°, 30.3°, 34.9°, 46.8°, 47.2°, 57.2° with respect to the beam line. In the experiment Neutron Wall is an ancillary of the GALILEO array, so the focal point is located 50 mm down stream from the target position. In general the distance between the focus and the front edge of each segmented detector is 510 mm but in our experiment the distance was increased to 640 mm, due to the presence of the $LaBr_3(Ce)$ array. In figure 2.5, two different views of the array are shown. For our experiment the central part of the array was removed to allow the beam to pass through and reach the beam dump.

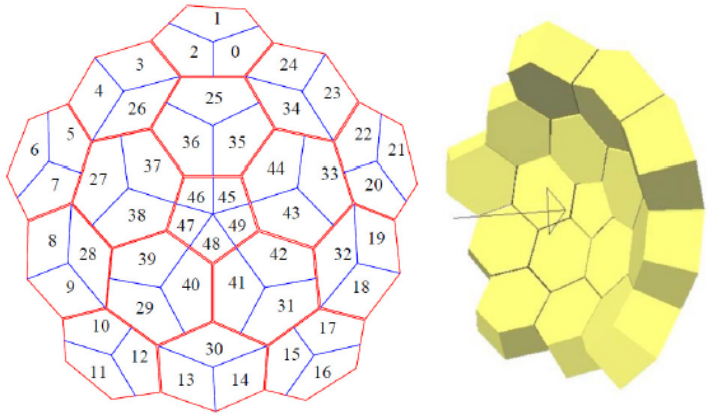

Figure 2.5: Representation of the Neutron Wall array. On the left the array viewed from down stream, with the official numbering scheme of the detector segments. On the right the 3D figure shows the aluminium cans of the neutron detectors as modelled in GEANT4, with the beam direction indicated by the arrow. In our case, the pentagonal detector (5 segments) placed in the center of the array was removed. Taken from (47).

The BC501A scintillator, is a carbon-hydrogen based liquid with the composition $C_6H_4(CH_3)_2$ (xylene). The neutron detection mechanism in the liquid scintillator is manly the elastic scattering of neutrons on protons. The recoiling proton converts part of its kinetic energy, gained in the elastic scattering process, into internal excitations of the molecules of the liquid. As a consequence of the molecules de-

excitation, photons are emitted with a wavelength detectable by the PMT. The absolute detection efficiency for a single neutron of energy En=1.5 MeV (with the array placed at a distance of 510 mm) is 0.5% for the single segment and $\approx$ 23% for the whole array.

2.3 The readout electronics

The Front-End Electronics is composed of two main blocks: preamplifiers, digitizers and processing electronics.
The HPGe detectors are read out by custom charge-sensitive preamplifiers employing a fast reset technique for dead time and dynamic range optimization (48). Typical output signals of the preampilifiers have a rise time of the order of 150 ns and an exponential decay constant of about 45 μs. The electric signals from the Bismuth Germanium Oxide (BGO) scintillators surrounding each HPGe detector are summed and gain-matched producing one single analog signal for each group of BGO scintillators. This work is necessary in order to reduce the number of channels to digitize. Output signals of HPGe-BGO couples are sent to digitizers that are composed by two independent modules. Each module is connected to a preprocessing board that provides the sampling clock and the synchronization signals, receive the digital data and performs the slow control of the digitizer module. Processing boards perform a digitalization of the differential input signals at 100 Mbps with 14 bits of resolution. The digital output is sent to a 12-fiber optical cable via high-speed serial links, encoded with the JESD204A protocol and working at 2 Gbps each. Each HPGe channel has two programmable input ranges, corresponding to energy interval of 0-7 MeV and 0-20 MeV for γ-rays interacting in HPGe detectors (49). For the experiment we used the input range corresponding to 0-7 MeV to maximize the energy resolution of HPGe detectors. The preprocessing board consists in a custom PCI express board which processes and sends data to the hosting PC through a 4 x PC express link. The data from 36 high-speed links at 2 Gbps are processed in a Xilinx Virtex-6 Field Programmable Gate Array (FPGA), where custom algorithms select the information from events of interest and send the data to the hosting PC via the PCI express link at a sustained rate up to 400 MB/s (49).
After the protocol decoding, samples get processed in a first level trigger generation module using fast moving window deconvolution in order to limit the influence of electronic noise and baseline fluctuations on the trigger. The trigger module sends a trigger request to the Global Trigger and Synchronization (GTS) system, which is in charge of the trigger coordination of the whole array and of other detectors in the setup. The GTS system provides a phase-matched and phase-aligned clock

(100 MHz with sub-nanosecond precision) and a timestamp to the first-level trigger generator.
When the resulting signal exceeds a programmable threshold the energy computation mechanism and the capture of the trace are activated. In this case, data contains the computed energy deposited in the HPGe detector and BGO scintillator (**Long-Trace Energy (LTE)**) and a short trace with a programmable length up to 250 samples around the trigger instant (**Short-Trace Energy (STE)**). The computation of the energy in the FPGA prevents the transferring a high amount of data to the PC. The Long-Trace Energy is computed from the input pulse using a Moving Window Deconvolution (MWD) algorithm with a short trapezoidal shaping. The use of a shorter shaping time in the filter provides a trigger signal while the computation of the energy is still taking place. The Short-Trace Energy around the trigger instant permits to analyse the digitized samples in the on-line software used for read out. On the other hand, trace capture is composed of a few hundred of samples (up to 250) from the digitized output signal and recorded in a time window of 1 μs around the trigger sample. The long trace length, indeed, is enough for the Pulse Shape Analysis algorithm but it is not adequate to analyse the input signal in the frequency domain. While the LTE estimate provides a better energy resolution for both GALILEO and EUCLIDES, we found that the best energy resolution for the $LaBr_3(Ce)$ detectors is obtained using the STE approach. This is due to the fact that the programmable parameters of the MWD algorithm cannot be optimized for the very fast $LaBr_3(Ce)$ signals.

2.4 The Data Acquisition System (DAQ)

The GALILEO DAQ is based on the XDAQ framework (50), a software that was designed and developed for the data acquisition of the CMS experiment (49). A different XDAQ application was developed in order to manage the GALILEO data flow. A schematic picture of the GALILEO Data Acquisition System is shown in figure 2.6.
The DAQ is composed by four main parts: the readout units, the filter units, the builder units and the merger units. All of these are written in C++ language and compiled for Scientific Linux 6 operating system. The readout units run on the front-end PCs, equipped with the custom preprocessing board. The rack in experimental hall hosts 9 machines (indicated with gal-XX in figure 2.6) where **Readout Units (RU)** and **Local Filter (LF)**, **Builder Units (BU)**, **Merger Units (MU)** and **Global Filters (GF)** run. Two RUs are dedicated to HPGe detectors (25 channels), four to EUCLIDES Si detectors (40 channels in our case), one dedicated to Neutron Wall and one to other possible detectors, that in our case

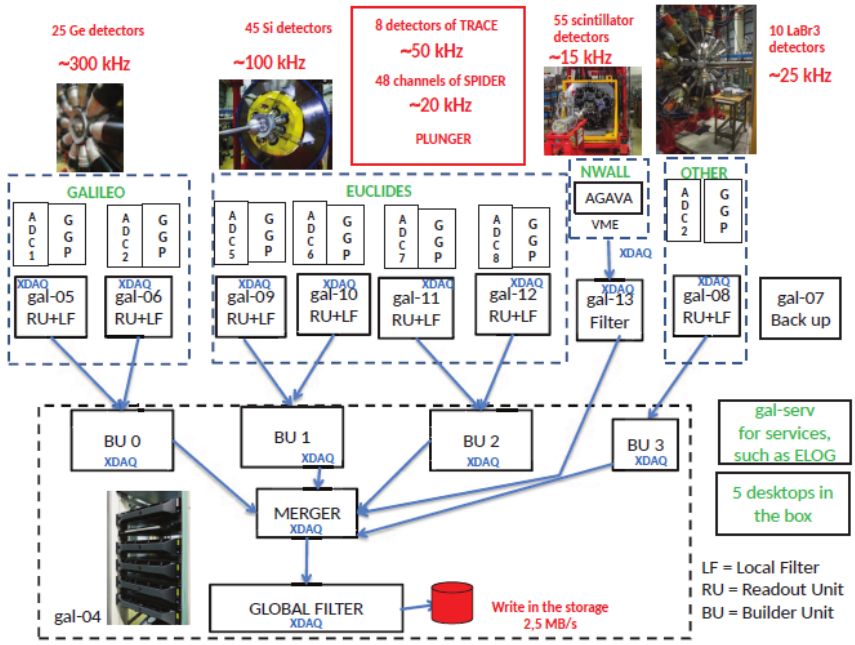

Figure 2.6: GALILEO Data Acquisition System (51)

are the 10 $LaBr_3(Ce)$ detectors. Another machine is dedicated to the BUs, MU and GF. At this point, any RU dispatches data to the local filter units applications. Local filters unit have the purpose of running dedicated algorithms to the raw acquired data. Different filters are applied at this level of the chain: the Compton suppression, checking the time coincidence between HPGe and BGO detectors (if there is a coincidence the event is rejected at this level), calibrations, the pile-up rejection and the Digital Constant Fraction Discriminator. The short traces are 100 samples long (1 μs) and from the comparison between them and the long trace integral it is possible to perform the pile-up rejection. At this level, files have the following format: the size of the event, the key word (that identify the type of detectors), channel number and time stamp. The event is written in two lines, one for HPGe and one for BGO, in case of the GALILEO detectors and one for E and one for ΔE for EUCLIDES detectors.

After the first level of filtering, data are sent to the Event Builder which performs the time ordering and creates a complete event within a configurable time coincidence window, set to a standard value of 50 TS, that corresponds to 500 ns. The BU

looks only the channel number and the TS. There are 4 BUs, one for GALILEO, 2 for EUCLIDES and 1 for $LaBr_3(Ce)$ detectors. Every kind of detector can trigger the opening of the event windows of 50 TS; the BU looks for the event with the lower TS and uses it as start. Now, let's suppose that a HPGe from GALILEO array makes the trigger and a window of 50 TS is opened. A value of TS=0 will be assigned to this first event. If, within this window, a different array measures an event, another window 50 TS long will be opened. All these sub-events will form one "single event" in the BU, with multiplicity defined by the number of γ-rays detected, as shown in figure 2.7.

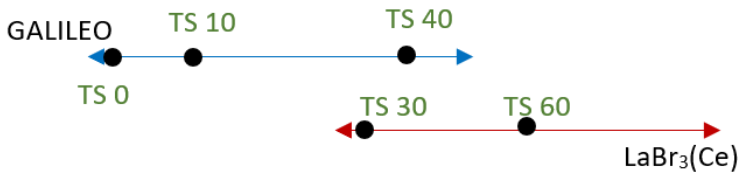

Figure 2.7: Scheme of the creation of a "single event" in the BU. The GALILEO Array opens the main windows of 50 TS units (with the sub-event TS=0). A second window opens by $LaBr_3(Ce)$ detection with the sub-event TS=30. The "single event" will have multiplicity 5 and will be composed by 3 sub-events on GALILEO and 2 sub-events detected by $LaBr_3(Ce)$.

It's important to underline that there are two extreme cases: the first one happens when only one type of array detects something and in this case the "single event" is composed by sub-events arrived within 50 TS or 500 ns. The other one is formed by sub-events with a maximum distance of 100 TS or 1 μs, that occur when a second array detect something just a moment before the closure of the main window. At the end of the BU two information are added, the size and the built event. The Merger Unit collects and combines data from all the builder units. Additional branches, for which no builder units are requested, can be directly sent to the merger as it was the case of the Neutron Wall Array. Finally, the Global Filter unit (GF) performs a last stage of data filtering before storing the data on disk. In particular, the GF performs a software trigger algorithm able to select events based on the fold of the different arrays and on the time coincidence between GALILEO and its ancillary detectors. This was implemented to reduce the data written on disk. Inside the event the information, for each detector module is characterized by 8 parameters: Energy raw and calibrated from the digitizers, the baseline position, the energy raw and calibrated from the local filter (obtained finding the maximum

of the short trace), the digital Constant Fraction Discriminator (to have a more precise value of time), the short integration signal and the long integration signal (for detectors with signals too short for the digitizers).

CHAPTER 3

Data analysis of the GALILEO data

Errors using inadequate data are much less than those using no data at all.

Charles Babbage

In this chapter we will start with the description of the main information we obtain from the Data Acquisition System and we will discuss all the variables we need for the data analysis. In particular, here we are going to focus on the GALILEO Array, analysing the time variable and time coincidence between two or more events. From the energy spectra, we will identify the emitted γ-rays in order to determine the population of the residual nuclei.
Even if, we produced the two compound nuclei, ^{60}Zn and ^{62}Zn, thorough 4 reactions, in order to create them at two different temperatures, in the following analysis, for sake of simplicity, only the results on the reaction ^{32}S + ^{30}Si $\rightarrow ^{62}$Zn at T= 2 MeV are reported.

3.1 Preliminary analysis

As we understood from the DAQ description, after this process, we obtain that each detected γ-ray has a group of 8 variables associated to it. When all the events are collected, the single acquired run, written in a special format, is transformed in a root file. Each "event" is written in an array, that has a length equal to the number of sub-events (the fold of event) and each sub-event is defined with the linked variables. We have to keep in mind during the analysis that the GALILEO spectra and the fold are all Compton suppressed. The first step of the analysis concerns the energy calibration, the fold simulations and the Doppler Correction.

3.1.1 Energy Calibration

The energy calibration of the HPGe detectors was performed using the following radioactive sources: ^{22}Na, ^{60}Co, ^{88}Y, ^{133}Ba, ^{137}Cs, ^{152}Eu, which emit γ-rays in the energy interval 0.1-3 MeV. Polynomial functions up to the fifth order, depending on the detector, were used. For the single detector the FWHM of the 1332.5 keV transition was measured to be $\approx$ 2.2 keV corresponding to an energy resolution of 0,17% and consistent with what expected for the GALILEO HPGe array (40). In figure 3.1 the calibrated energy spectra for the 25 detectors is shown.

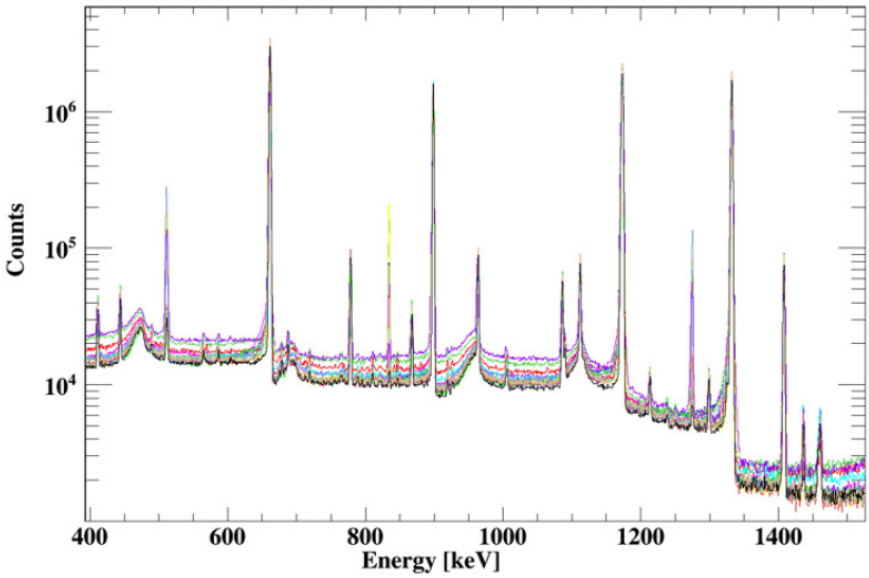

Figure 3.1: Calibrated energy spectra of the 25 HPGe detectors of the GALILEO array. Taken from (40)

3.1.2 Doppler correction

Since the γ-rays are emitted by a non-stationary object, the residual nucleus, a the Doppler correction must be applied to bring back the γ-energy spectrum in the rest frame of the emitting nucleus. The relation between the energy in the rest frame of the emitting nucleus, E_0, and the detected energy E_γ depends on the velocity of the nucleus and the angle of emission respect to the nucleus direction as:

$$E_0 = E_\gamma \frac{(1 - \beta cos\theta)}{\sqrt{1 - \beta^2}}. \tag{3.1}$$

Reaction	E_{beam}	β
$^{32}S + ^{28}Si \rightarrow ^{60}Zn$	86	0,041
$^{32}S + ^{28}Si \rightarrow ^{60}Zn$	110	0,046
$^{32}S + ^{30}Si \rightarrow ^{62}Zn$	75	0,036
$^{32}S + ^{30}Si \rightarrow ^{62}Zn$	98	0,042

Table 3.1: β values for the 4 different reactions of the experiment calculated using the PACE4 code, modelling the CN decay.

The β values for the 4 different reaction are reported in table 3.1. In figure 3.2 the comparison between the spectrum before (the black one) and after (the red one) the application of the Doppler correction is presented for the reaction $^{32}S + ^{30}Si \rightarrow ^{62}Zn$ at 75 MeV.

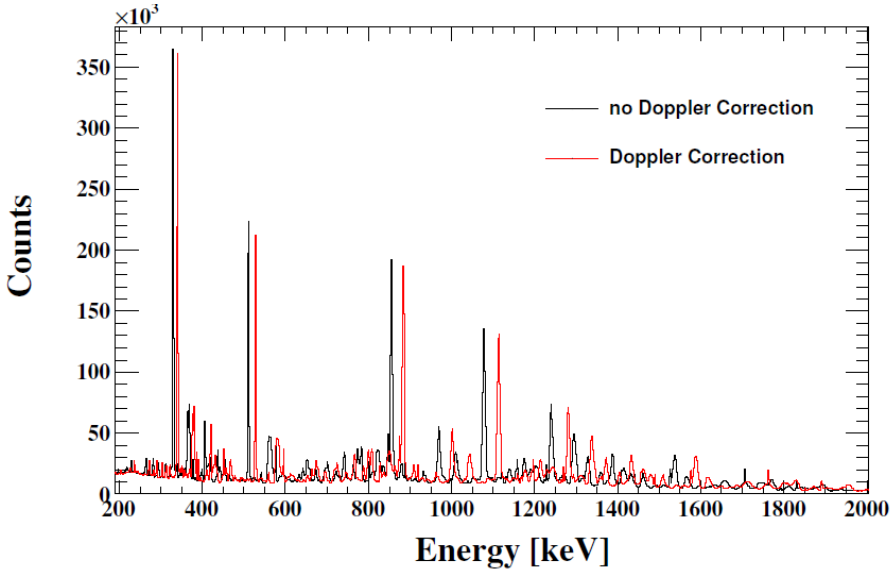

Figure 3.2: Energy spectra associated with the compound nucleus ^{62}Zn with $E_{beam} = 75$ MeV, before (black spectrum) and after (red spectrum) the Doppler correction. Taken from (40)

3.1.3 Fold distribution

As said before, the Galileo spectra are Compton suppressed. This, unfortunately forbids us to obtain information on the relation between fold and multiplicity and

thus on the spin distribution of the CN. To understand more the relation between unsuppressed and suppressed fold we performed some simulations with a code that simulates the GALILEO apparatus composed by both HPGe detectors and related BGO shields and a single γ-ray emitted from the centre of the scattering chamber in a random direction (52). Figure 3.3 shows the trend of the probability of interaction as a function of energy and fold, for unsuppressed (left panel) and suppressed (right panel) events. In the inset of each figure there is an enlargement of the fold 1 trend with energy. We don't plot the fold=0 to make more visible the fold=1 and fold=2. We can observe that in the case of unsuppressed events, the probability to detect a γ increases with energy for both folds. This is due to the Compton interaction probability, dominant effect from 300 keV. We can also observe that the probability of unsuppressed fold=1 saturates at $\approx 7.9\%$ for energies higher than 500 keV, whilst for the suppressed fold=1 the probability decreases assuming a value $\approx 3.8\%$ at around 1100 keV.

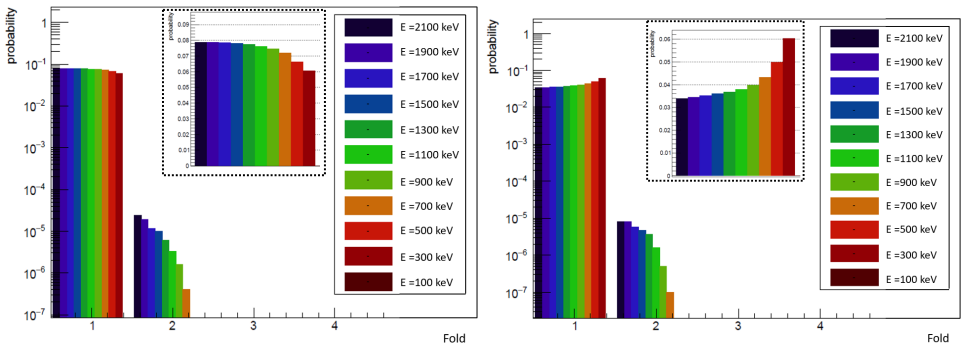

(a) Unsuppressed *(b) Suppressed*

Figure 3.3: Trend of the interaction probability as a function of energy and fold, for unsuppressed (left panel) and suppressed (right panel) events. Taken from (52).

3.1.4 Full energy peak absolute efficiency

The GALILEO efficiency is an important quantity for the determination of the cross-section of the residual nuclei. The calculation of the absolute photo-peak efficiency as a function of energy was performed in (53), using a calibrated ^{152}Eu source. The absolute efficiency is defined as the ratio between the number of γ-rays detected and emitted by the source (40). The calculation was performed considering all the 25 detectors of GALILEO. The absolute efficiency value for the full energy peak for the GALILEO array located at 22.7 cm from the target and with the absorber, was estimated to be $\approx 2.3\%$ at ≈ 1.3 MeV. The efficiency curve

for a single GALILEO HPGe detector is shown in Fig 3.4.

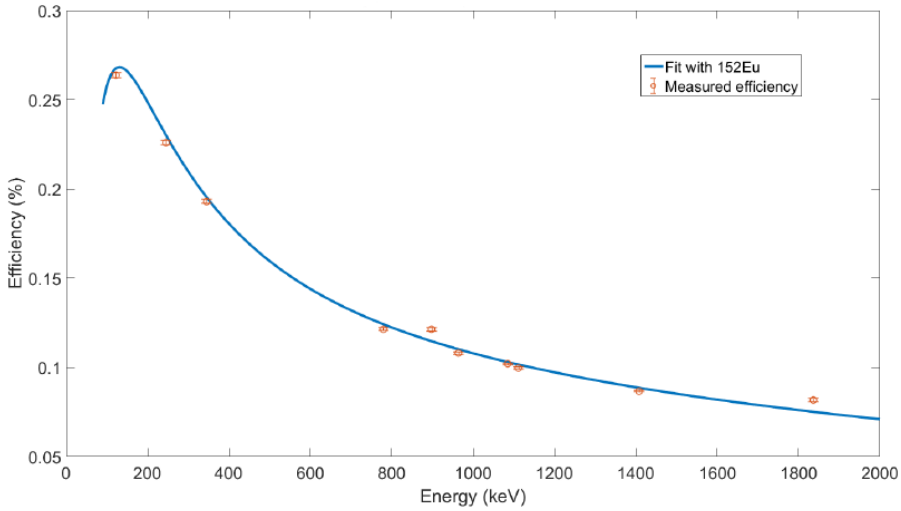

Figure 3.4: Absolute efficiency for the full energy peak for a single GALILEO HPGe detector, in the Compton suppression mode. Taken from (40)

3.2 Time and coincidence

In section 2.4, we explained that each event is created in the Event Builder starting from a sub-event (a TS=0 is assigned) that opens a window of 500 ns. All the sub-events arrived within 50 TS, in case of just one array, or within 100 TS, in case of two or more arrays are considered as part of the same event. Therefore, the Time Stamp is the main variable that gives us the time information. The determination of Time Stamp is obtained through the leading-edge method. Using a leading-edge discriminator, where the input signal crossing a fixed threshold level generates the output pulse, is the simplest way of implementing a time measurement. However, the measured output time depends on the amplitude, on the rise time of the input signal and on the sample frequency (providing the minimum value of the resolution which can be achieved), making this option useful only in those applications involving a very narrow range of signal amplitudes and rise times. Indeed, signals with the same rise time and different amplitudes occur simultaneously, but they cross the threshold at different times thereby generating time walk of the output logic pulse from the discriminator. Similarly, signals, having the same amplitude but different rise times, introduce a walk error. The error is most pronounced for signals with longer rise times that only slightly exceed the threshold level. This

method, therefore, provides the first time information but brings along with it the time walk error and a minimum resolution of 10 ns (1TS = 10ns). In order to obtain a more precise measure of time, a digital Constant Fraction Discriminator method (CFD) is also implemented. The scheme of the CFD is shown in figure 3.5. The input signal is first split into two parts. One is delayed and the other one is inverted and attenuated by a constant fraction f, which corresponds to the desired fraction of the full amplitude. The attenuated pulse and the delayed pulse are then summed to give the time that this pulse crosses the zero axis. In a CFD, therefore, the time, at which the logic pulse is generated, depends on the zero-crossing point of the bipolar pulse. In theory, even though the pulses have different amplitudes, the time at which the waveforms cross zero volts is the same and depends only on the amplifier shaping constants, chosen to produce the pulses.

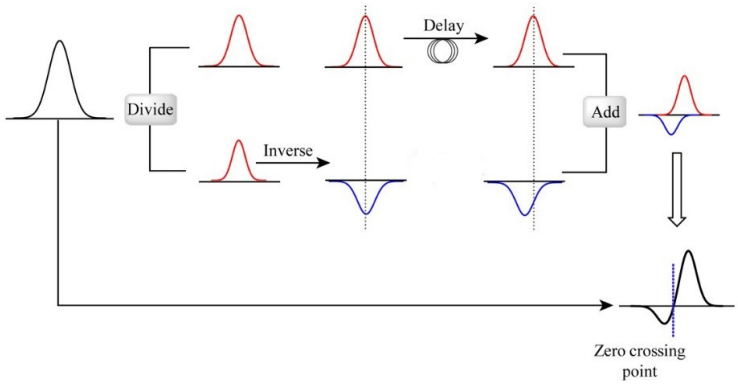

Figure 3.5: Scheme of Constant Fraction Discriminator method. The input signal is first split into two parts. One is delayed and the other one is inverted and attenuated by a constant fraction f. The two signals are then summed. The time at which the logic pulse is generated depends on the zero-crossing point of the bipolar pulse.

We can now define a global time variable, that we are going to call TimeDiff, formed by the sum of the Time Stamp and the value extracted using the CFD method, that gives a more precise value of event time. This new variable is crucial for defining the time coincidence between events. The time coincidence is a fundamental condition to be applied to the data in order to identify events that belong to the decay of the same compound nucleus. As we explained, the event, in the way it is defined, contains sub-events detected in a range up to 1μs. The compound nucleus decay takes place in much less time. The way to determine if two or more events belong to the same CN decay is to measure the time distance between them. We expected

that the major part of events will be detected in a very limited span of time. We have therefore built a matrix that has the difference of the value of the variable TimeDiff between two sub-events on the y axis and the energy on the x axis. The matrix is shown in figure 3.6a. We can immediately notice that the largest amount of events is located within $\pm 50ns$, far from the others as we can see in 3.6b where a zoom of the whole matrix is shown. This matrix allows us to define and select the events that we can considered in coincidence between them. For the GALILEO events the coincidence is set to 40 ns. The second thing we can notice is that there are vertical lines that stand out at certain energies. These energies that extend over time represent isomers, populated states that have very long life time and natural background. The analysis of the isomers will be deepened in the section 3.3.1.

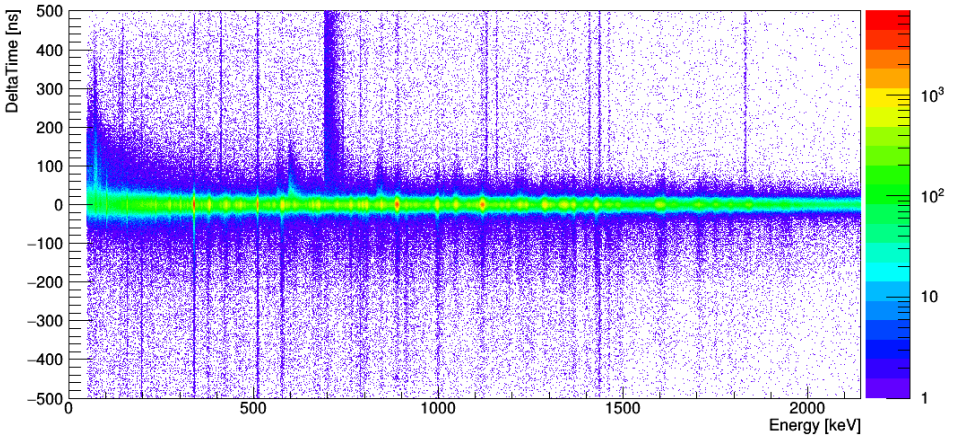

(a) Matrix for the coincidence events for GALILEO. The largest amount of events is located within 100 ns.

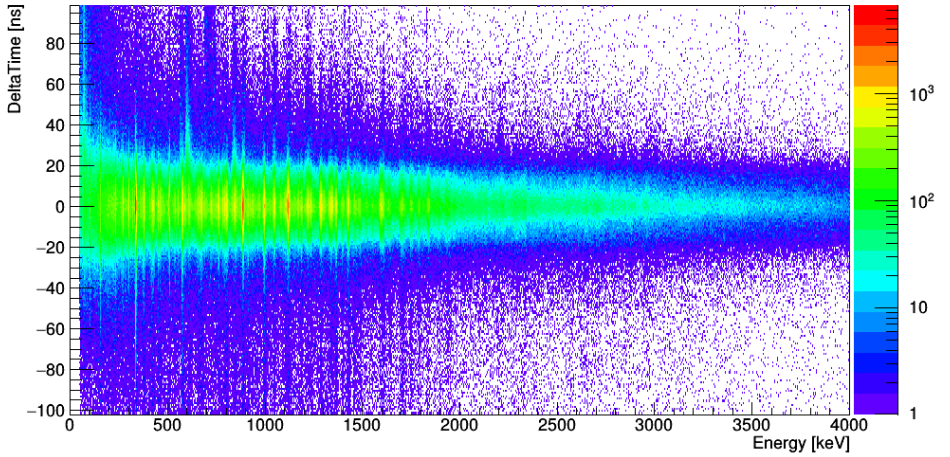

(b) Zoom of the matrix shown in part (a). For GALILEO events the coincidence is set to 40 ns.

Figure 3.6: Two matrices having on the y axis the variation of the TimeDiff variable (defined as differences between the sum of Time Stamp and the Constant Fraction Discriminator) between couples of events and on the x axis the energy.

3.3 Energy and residual nuclei identification

As a result of the fusion-evaporation reaction, the compound nucleus is formed at certain excitation energy. During the decay process, the nucleus emits many particles,namely neutrons, protons and alphas, until the excitation energy remains

above the particle binding energy. After that, it decays only by the emission of γ-rays around and following the yrast-line. The entire process is illustrated in figure 1.7. The nuclei populated after the particle emission are called residual nuclei, or residues. Each residue, created in an excited state, is going to de-excite by the emission of low-energy γ rays and the identification of each transition leads to information about which type of residues are populated in the reaction. As discussed before, HPGe detectors, that compose the GALILEO array, are optimal for the detection and the identification of low-energy γ rays, thanks to their good energy resolution. The γ-ray spectrum of the GALILEO array, associated with the reaction ^{32}S + ^{30}Si $\rightarrow^{62}$Zn at T= 2 MeV, is displayed in figure 3.7. Using the RadWare archives (54) as a reference, ^{59}Ni, ^{56}Co and ^{56}Fe have been identified to be the main residues populated in the reaction and the transition from the first excited state to the ground state is indicated for each residual nucleus, with a coloured rectangle which contains the value of the energy.

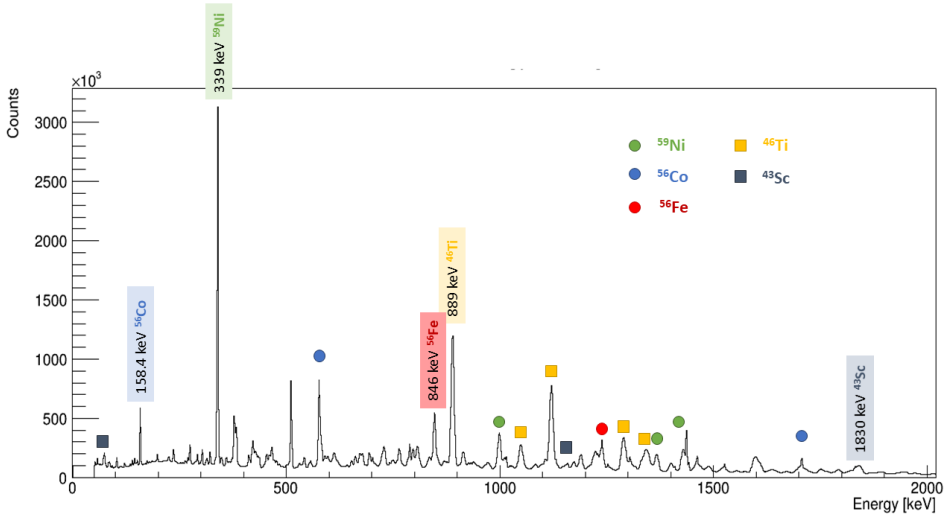

Figure 3.7: Energy spectrum of HPGe detector for the reaction ^{32}S + ^{30}Si $\rightarrow^{62}Zn$ at T = 2 MeV. The main residues are identified and the transition to the ground state of the five residues are underlined.

After a careful analysis, we realized that some peaks don't belong to the residual nuclei produced in the reaction and expected in the statistical model and were identified as belonging to ^{46}Ti and ^{43}Sc nuclei. These two nuclei result from the decay of the compound nucleus ^{48}Cr, formed in the reaction ^{32}S + ^{16}O $\rightarrow^{48}$Cr. This suggested the presence of oxygen contamination in the target, probably due to the target production technique. The ^{28}Si and ^{30}Si targets were then analysed at

the AN2000 accelerator of the Laboratory Nazionali di Legnaro (LNL-INFN, Italy) in October 2016. A proton beam was used to determine the targets composition through the Elastic BackScattering (EBS) technique. The results of the analysis, reported in (55), confirmed the presence of Oxygen in the targets. In particular, in (55), it is indicated that the ratio between the Si and O amounts is $Si/O \approx 1$ for the ^{28}Si target and $1.2 \leq Si/O \leq 1.5$ for the ^{30}Si one. Moreover, some other elements, such as C and Pb, are present within the targets, but in negligible quantities. Figure 3.8 shows an image of the ^{28}Si target produced using a scanning electron microscope (SEM).
The main residues identified in the analysis are reported in table 3.2, together with the corresponding compound nucleus, the decay channels and the transition from the first excited state to the ground state.

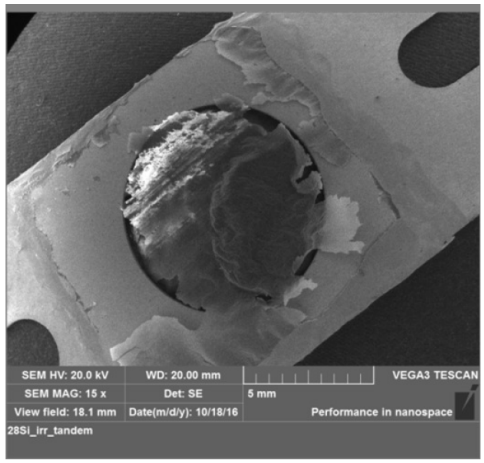

Figure 3.8: Picture of the ^{28}Si target produced using SEM technique

3.3.1 Isomers and background gammas

The energy spectrum of the GALILEO array is the sum of the spectra of the Compton suppressed single detectors, that, as we explained in the previous chapter, belong to 4 different rings. If we compare the energy spectra of the different rings, before performing the Doppler correction, we expected many peaks to be shifted in energy. This is indeed, what we observe together with some un-shifted peaks. These stationary peaks could be γ-rays of background radiation or isomeric states populated in the reaction with long lifetime that allows the nucleus to stop before decay. An example is shown in figure 3.9, in which two main transitions are visible. The first at 339 keV is the transition to the ground state of ^{59}Ni that, emitted in

Residues	Compound	Decay mode	Transition to the GS
^{59}Ni	^{62}Zn	2p1n	339 keV
^{56}Co	^{62}Zn	1p1n1α	158.4 keV
^{56}Fe	^{62}Zn	2p1α	846 keV
^{46}Ti	^{48}Cr	2p	889 keV
^{43}Sc	^{48}Cr	1p1α	1830 keV

Table 3.2: Main residual nuclei observed, with the relative compound, the decay mode and the energy of the transition from the first exited state to the ground state for the reaction ^{32}S + ^{30}Si $\rightarrow$$^{62}Zn$ at T= 2 MeV.

flight, shows the expected shift. The second one at 511 keV is overlapped for the four rings because it is emitted following the annihilation of a positron somewhere.

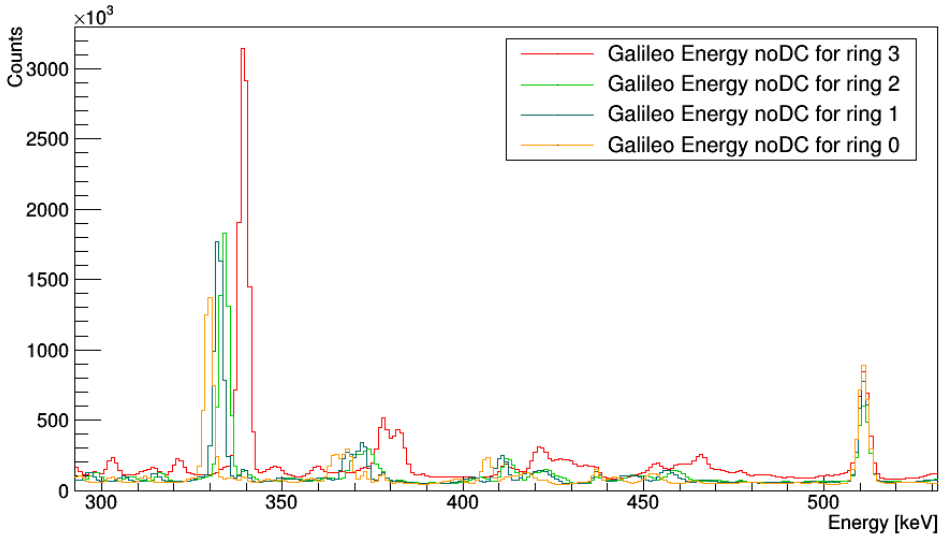

Figure 3.9: Comparison between a section of the GALILEO energy spectrum for the four different rings. The first peak on the left at 339 keV is the transition to the ground state of ^{59}Ni that, emitted in flight, shows the expected shift. The second one at 511 keV is overlapped because it is emitted following the annihilation of a positron in the crystal.

In order to study more systematically these events and to discriminate background gammas and isomeric states, we can use the DeltaTime-Energy matrix shown in the previous section in figure 3.6a. When we compose the matrix, for each couple

of sub-events (time-ordered), the time difference between them is calculated and associated to the first energy and the same difference, with opposite sign, is associated to the second energy. Because isomeric states have long lifetime, we expected they are going to be the last sub-events and for this reason, the time difference associated will be positive in sign. Regarding the background sub-events, instead, the time difference associated to the energy could be both positive and negative because time detection of these gammas is completely random. Looking at the matrix we can indeed notice that there are vertical lines only in the upper part of the matrix that are linked to isomeric states, vertical lines only in the lower part, connected to compound nucleus state (if in coincidence with an isomer) and vertical lines that extended over all time differences, that represent natural events (in random coincidence with CN events). In table 3.3 the identified lines are listed with the emitter nucleus and classified if they are isomers, gammas from natural background or residues decays.

Isomers		**Background**		**Residues**	
Energy[keV]	Nucleus	Energy[keV]	Nucleus	Energy[keV]	Nucleus
70	^{43}Sc	511	e^-	158	^{56}Co
136	^{43}Sc (*)	789	^{138}La	197	^{54}Fe
146	^{54}Fe (*)	1436	^{138}La	339	^{59}Ni
411	^{54}Fe	1460	^{40}K	576	^{56}Co
1130	^{54}Fe			763	^{59}Ni
1157	^{43}Sc			889	^{46}Ti
1408	^{54}Fe			998	^{59}Ni
1830	^{43}Sc			1049	^{46}Ti
3432	^{54}Fe			1120	^{46}Ti
				1705	^{56}Co

Table 3.3: The identified line are listed with the emitter nucleus. On the left are listed the transitions which belong to isomeric state (upper part of the matrix), in the central part, the γs coming from background radiation (extended over all the time window in matrix) and on the right, the transitions of residual nuclei (lower part of the matrix).

The first isomer is in the ^{43}Sc nucleus. This is populated in a state with lifetime 472 ns that decays by the emission of 136 keV γ-ray and than with other transitions down to the 1830 keV decay to the ground state. The other isomeric state with lifetime 364 ns belong to the ^{54}Fe nucleus. This nucleus is produced following the reaction in a very small quantity. We don't see it, indeed, in the total energy

spectrum but only selecting the isomers with this matrix, we were able to identify it. Moreover, we identified the 511 keV emitted following the annihilation of an electron in the detectors, as previously mentioned, and the ^{40}K γ-rays that are always present as background radiation. The two gammas coming from ^{138}La, emitted in the $LaBr_3(Ce)$ detector, that contain a small percentage of this isotope, are also detected by HPGe detectors. The lines in the residues column belong to the main residual nuclei produced in the reaction: ^{56}Co, ^{59}Ni, ^{46}Ti. Besides, we observed the 197 keV that comes from a state that is populated before the isomeric one in ^{54}Fe. In the region of the matrix between 600 and 700 keV the contribution due to inelastic scattering of neutrons in HPGe detectors is also visible. In Figure 3.10 a projection of this section shows the characteristic and well-known rather broad distributions due to inelastic scattering of fast neutrons ((46)). We can observe the combination of 596 keV and 608 keV transitions coming from the reaction $^{74}Ge(n,n')$ and the 691 keV emitted following the reaction $^{72}Ge(n,n')$. This last peak is special since it is entirely due to the detection of conversion electrons, which are emitted when the 0^+ first excited state of ^{72}Ge, with a half-life of 444 ns decays to the ground state (56). This is the reason why in the matrix we observe it over all time.

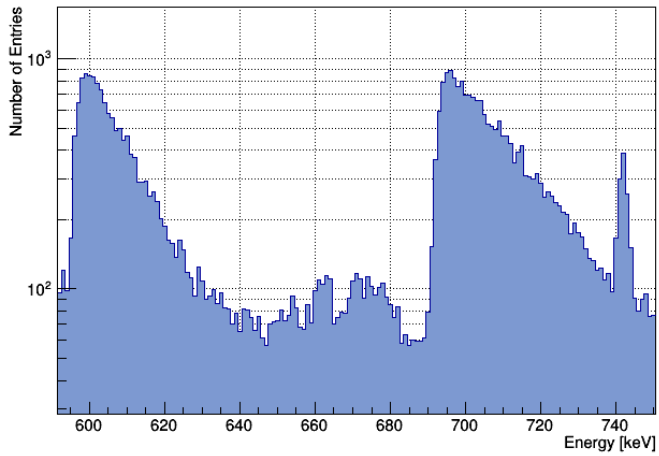

Figure 3.10: Contribution due to inelastic scattering of neutrons in the HPGe detectors. The peak on the left is the combination of 596 keV and 608 keV transitions coming from the reaction $^{74}Ge(n,n')$ and the other one is the 691 keV emitted following the reaction $^{72}Ge(n,n')$. This last peak is due to the detection of conversion electrons, which are emitted when the 0^+ first excited state of ^{72}Ge, with a half-life of 444 ns decays to the ground state (56).

CHAPTER 4

Analysis of high energy data

Analyse data just so far as to obtain simplicity and no further.

Henri Poincaré

In this chapter, the data analysis related to the $LaBr_3(Ce)$ detectors is presented. After the first step analysis, we will explain how to extract the energy spectrum in order to study the GDR decay for the determination of the isospin mixing parameter.

4.1 Preliminary analysis

As mentioned several times, the $LaBr_3(Ce)$ array is the one used to measure the γ-decay from the IVGDR of the nucleus of interest, that is located around 15 MeV. Therefore, an energy calibration up to 15 MeV was performed. Another important parameter to be under control is the time information that plays a key role in the background rejection. For this reason the timing of events was accurately studied.

4.1.1 Energy Calibration

For the energy calibration of $LaBr_3(Ce)$ detectors the sources of ^{137}Cs, ^{60}Co and $^{241}Am - Be$ were used and in addition, an in beam calibration was performed with the reaction $^{11}B + d \rightarrow ^{12} C + n$ in order to guarantee a calibration interval from 0.6 to 15.1 MeV. This reaction, indeed, excites a resonant state of ^{12}C, which decays emitting a γ-ray of energy of 15.1 MeV. Due to the fact that the PMT does not guarantee good linearity over a so wide energy range, a quadratic calibration was employed and, in this way, the difference between the calibrated energy and the nominal one, i.e. the residue, is very small ($\leq$ 100 keV for all the detectors)

as shown in figure 4.1 (40). During the experiment, the calibration measurements were performed before and after each one of the four CN reactions. This allowed us to check the gain stability of the detectors along all the experiment and to correct for any possible drift.

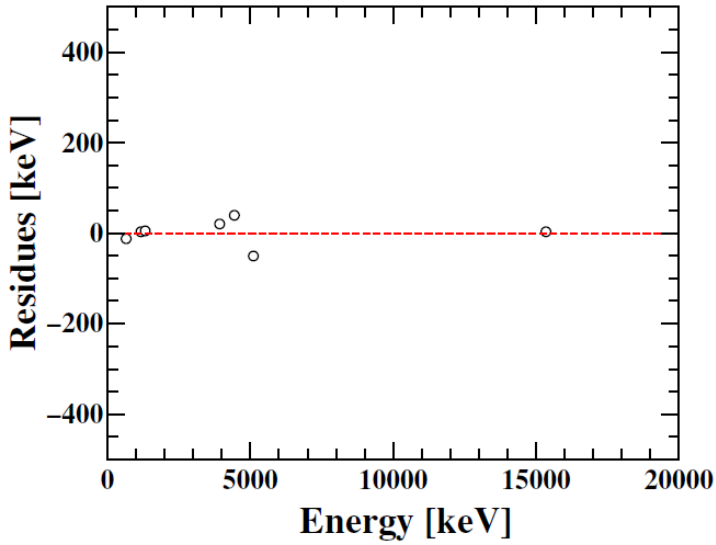

Figure 4.1: Difference between the calibrated energy (quadratic calibration) and the nominal one, i.e. residues, for a single $LaBr_3(Ce)$ detector (40).

4.1.2 Efficiency

The absolute photo-peak efficiency was measured for the $LaBr_3(Ce)$ array with a ^{60}Co source (40). This source emits simultaneously two γ-rays in the same energy range (1173.2 keV and 1332.5 keV) and by comparing the areas of each experimental peak associated with a γ-transition (1173.2 keV or 1332.5 keV) and the sum peak, corresponding to events in which both γ-rays release all their energy inside the detector, it is possible to obtain an absolute efficiency. This is called sum-peak technique. To use this method we need to assume that the efficiency for a γ-ray of 1173.2 keV is the same of that for 1332.5 keV. The absolute efficiency values of the 10 $LaBr_3(Ce)$ detectors were averaged. The result was $\epsilon = (0.22 \pm 0,02)\%$ in agreement with the simulated value performed with the GEANT4 code. It is worth to note that, for γ-rays of 1332.5 keV, the absolute photo-peak efficiency of the whole $LaBr_3(Ce)$ array is $\approx$2.2 %, value very similar to that of the whole GALILEO array.

4.1.3 Response Function

The shape of the γ-spectrum that we measured, depends on the detection process. The fact that the photo-peak efficiency changes with energy, indeed, entails a modification of the measured γ spectrum. If we want to compare the experimental spectra with the simulated ones we have to know how the detection process perturbs the real spectra. This means that we have to consider the so-called "Response Function" of the apparatus. The response function of $LaBr_3$(Ce) detectors has been calculated following a standard procedure reported in (57, 58). We simulated 30 interactions, in $LaBr_3$(Ce) array, of monochromatic γ-rays from 1 to 30 MeV at single steps, obtaining 30 different simulated spectra. Each spectrum will be considered as a column in a 30x30 matrix, where each element (E_{det},E_γ) represents the probability to detect a γ-ray with energy E_{det} when a γ-ray of energy E_γ interacts. In this way, the spectrum detected (w) will be the product between emitted spectrum (v) and response function matrix (A):

$$w = A \times v \tag{4.1}$$

Therefore, to properly compare the experimental spectrum and the simulated one, the latter must be folded with the response function. In figure 4.2 the comparison between the γ-ray spectra simulated using the statistical code CASCADE before and after the application of the response function is displayed (40).

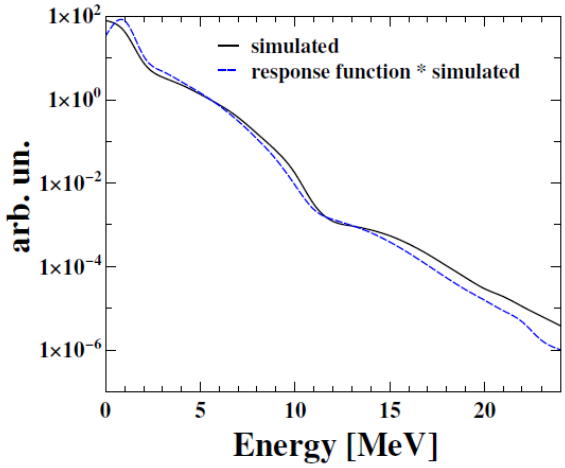

Figure 4.2: Comparison between the γ-ray spectrum simulated using the statistical code CASCADE before (black solid line) and after (blue dashed line) the application of the response function. Taken from (40).

4.2 Time, coincidence and energy

The time information for $LaBr_3(Ce)$ detectors is a fundamental quantity for the identification of GDR and to measure the isospin mixing coefficient. For this reason, two different approaches to obtain the time information were implemented. The first one is the same adopted for HPGe detectors, namely the combination of the leading-edge methods for the Time Stamp identification and the digital CFD resulting in the TimeDiff variable. As for HPGe detectors, we created a matrix that gives information about the difference in time between two events as a function of energy, that is reported in figure 4.3. This figure give us the selection capability for the coincidence between two $LaBr_3(Ce)$ events. Most of the events are located in the central part with a time difference between $\pm 80ns$, a value that we can define as the time coincidence range. This band is much larger than the one we evaluated for Germanium detectors. This is because the digital CFD is optimized for a typical signal of HPGe detectors that is much different from a $LaBr_3(Ce)$ signal and because the $LaBr_3(Ce)$ signal is yet passed through the spectroscopic amplifier.

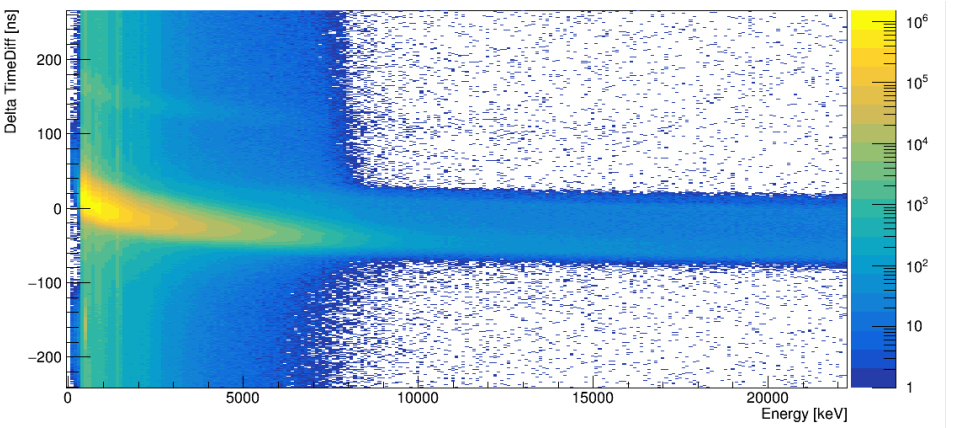

Figure 4.3: On the y axis there is the variation of TimDiff variable (defined as the sum of Time Stamp and Constant Fraction Discriminator) between couples of $LaBr_3(Ce)$ events. On the x axis there is the energy. For the $LaBr_3(Ce)$ events the time coincidence is set within ± 80 ns.

Therefore the second approach comes in, in order to obtain a more precise value of time. The time information for each detector was, indeed, provided also by the LaBrpro CFD coupled to a TAC module (Time to Amplitude Converter). Each TAC module has the LaBrpro CFD signal as START and the RF beam signal (after a delay) as STOP. Inserting a delay cable of 12 ns between the RF beam signal and the TACs input the time calibration was performed for each $LaBr_3(Ce)$ detector.

Since the experiment has run for several days and the time information, using RF, depends on the beam stability we produced for each detector and for each reaction a matrix that represents the "TAC time" as a function of events as reported in figure 4.4. In the left panel of the figure, we can observe that the time peak was not stable during the experiment, a drift of $\pm 2ns$ was observed. The time drifts were therefore corrected and the peak was aligned around 150 ns as shown by the matrix in the right panel of figure 4.4. This kind of correction, together with the time-walk correction, was done for each reaction.

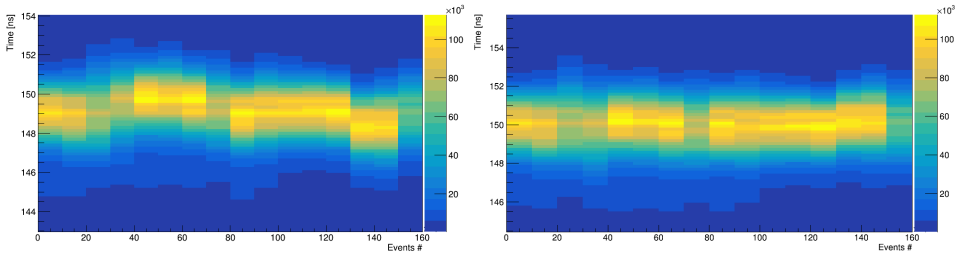

Figure 4.4: "Time-event" matrix for a single $LaBr_3(Ce)$ scintillator, associated with the reaction $^{32}S + ^{30}Si \rightarrow ^{62}Zn$ at $T = 2$ MeV before (on the left) and after (on the right) the time drift correction. The event number and the event time are reported on x and y axis, respectively.

In figure 4.5 the superposition of the aligned time spectra of the 10 detectors for the reaction $^{32}S + ^{30}Si \rightarrow ^{62}Zn$ at T = 2 MeV is displayed. The γ-ray prompt peak can be observed, together with a bump on its left, which indicates the presence of neutrons. The time separation between the neutron and γ-ray peak is $\approx$10 ns. This is consistent with the result of the simulations reported in (40).

In figure 4.6 the total time peak, corrected for the RF drift, the time walk and aligned at 150 ns is shown as a function of energy. We will see the importance of the discrimination between γ-rays and neutron for the identification of the GDR in the energy spectrum. The events of interest, the GDR decays, are located in the prompt peak of figure 4.5. These events will be selected to study the isospin mixing and all the events related to neutrons and background will be rejected. We can understand the effect of this selection if we create again the matrix reporting the variation of TimeDiff as a function of energy (figure 4.3) but now we impose the condition to the events to be in the prompt peak of the TAC spectrum. The resulting matrix is displayed in figure 4.7. By comparing the two matrices the impact of the selection is now visible. The almost totality of events is clustered around time 0 in a tighter peak.

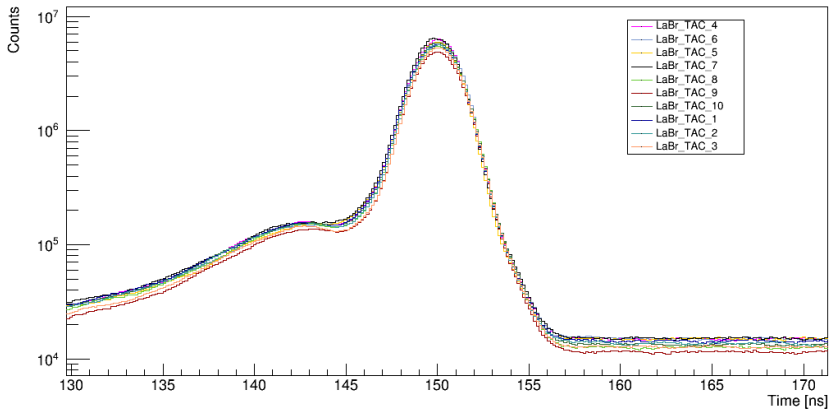

Figure 4.5: Time spectra for the 10 $LaBr_3(Ce)$ scintillators. The γ-ray prompt peak can be observed, together with a bump on its left, which indicates the presence of neutrons with a time separation of $\approx$10 ns.

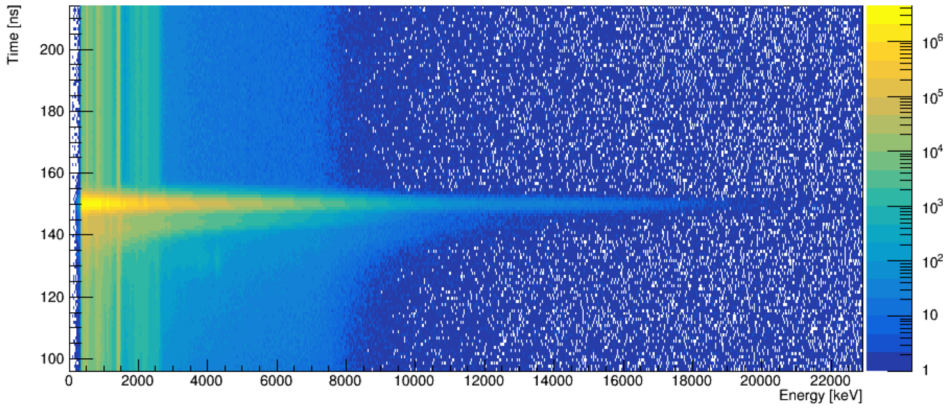

Figure 4.6: The total time peak, corrected for the RF drift, the time walk and aligned at 150 ns is shown as a function of energy.

As previously discussed, the time information is fundamental to the goal of the analysis because allows us to select only the events of interest, in particular, the γ-rays coming from the GDR decay. In figure 4.8 the energy spectra with different time selections choosing 5 ns interval are shown. The red spectrum is the total energy spectrum, for which no time selection is performed. The blue and the green spectra are obtained imposing a gate on the neutron bump and on the background, respectively. The neutron spectrum has a quite flat trend. In the background spectrum, we can notice 2 different structures. At low energy, we identify the

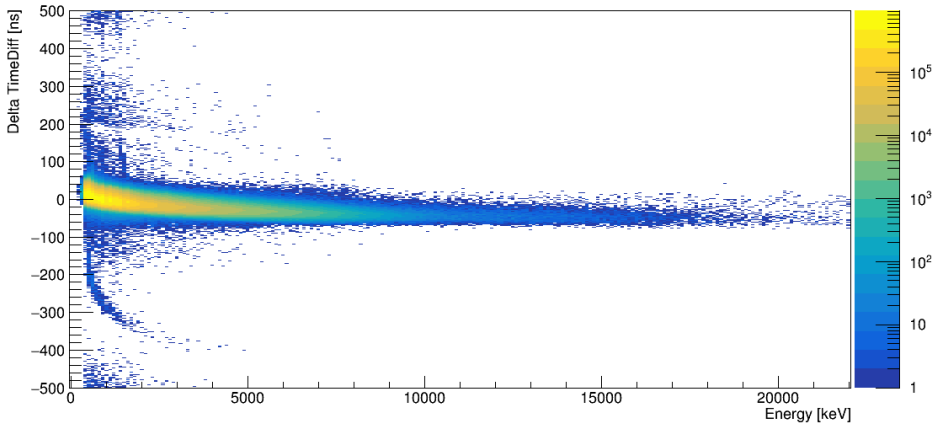

Figure 4.7: Variation of TimeDiff as a function of energy (as figure 4.3) with the selection of the events to be in the prompt peak.

.

internal radiation of $LaBr_3(Ce)$ crystals composed by a peak around 1462 keV and the alphas between 2 and 3 MeV. The second structure is around 7 MeV and it is due to thermal neutrons that are sufficiently slow to be detected as background radiation in the event subsequent to the one in which they are emitted. The yellow one, instead, is obtained with the selection on the γ prompt peak. The spectrum has the typical shape of the IVGDR decay in hot nuclei, as described in section 1.2.3, in which we notice the GDR bump in the region between 10 to 20 MeV. In order to obtain the final energy spectrum the background must be subtracted from the one with the gate on the prompt peak.
In the next chapter we will also use the GALILEO-$LaBr_3(Ce)$ coincidence. In figure 4.9 the matrix coincidence between the two arrays is presented. On the y axis there is the time difference between $LaBr_3(Ce)$ and GALILEO events and on the x axis, the energy of $LaBr_3(Ce)$. We can notice a time walk that brings us to define a coincidence within 70 ns.
In table 4.1 the coincidence times between different combinations of arrays are summed up.

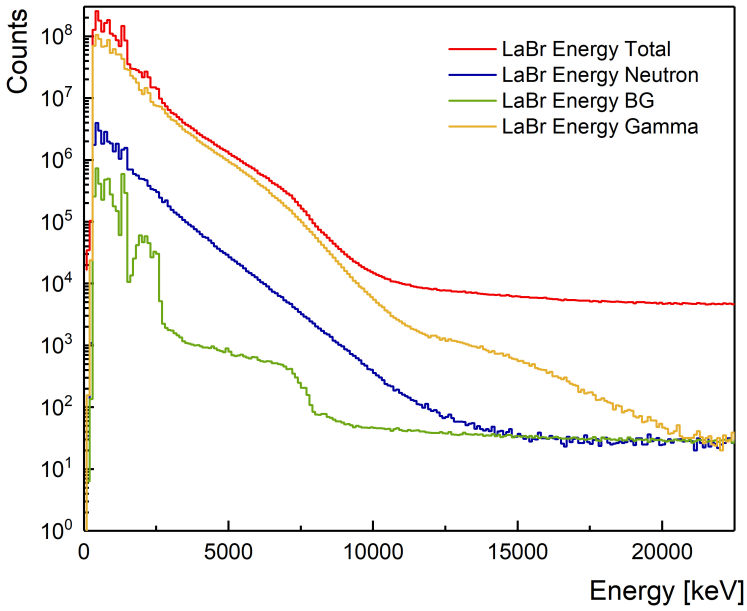

Figure 4.8: Energy spectra with different time selections are shown. The red spectrum is the total energy spectrum, in which no time selection is performed. The yellow one is obtained with the selection on the γ prompt peak: in the region between 10 to 20 MeV the bump represents the high-energy GDR decay. The blue and the green spectra are obtained imposing a gate on the neutron bump and on the background, respectively. All the selections in time were made choosing widths of 5 ns.

.

Types of arrays	Time coincidence
GALILEO-GALILEO	40 ns
$LaBr_3 : Ce$ - $LaBr_3 : Ce$	80 ns
$LaBr_3 : Ce$ - GALILEO	70 ns

Table 4.1: In this table the time coincidences between different combinations of arrays are listed.

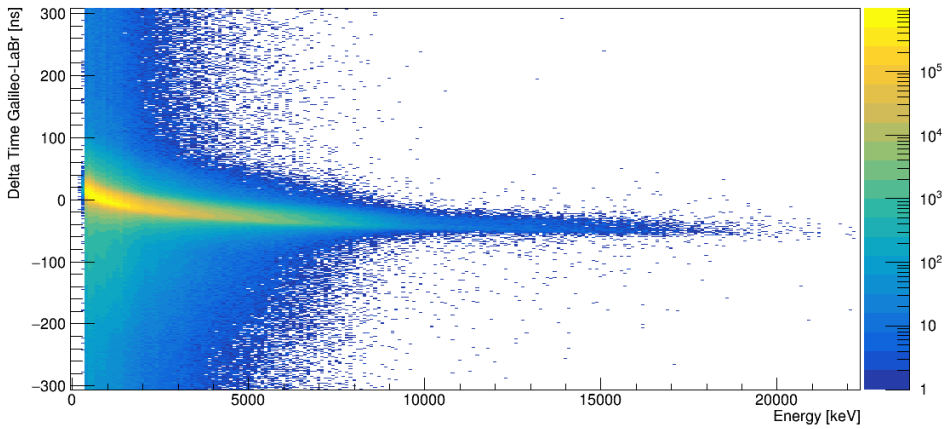

Figure 4.9: Coincidence matrix between two arrays : on the y axis there is the time difference between $LaBr_3 : Ce$ and GALILEO events and on the x axis, the energy of $LaBr_3 : Ce$. The time coincidence is set to 70 ns.

CHAPTER 5

Separation of the Oxygen contribution

There's always some relief in giving up

Lauren Oliver

As we could observe in the analysis of the GALILEO data regarding the study of populated residual nuclei we could clearly discriminate the contribution due to Oxygen and to Silicon. This double contribution is not visible in the high energy spectra of $LaBr_3(Ce)$, but it could be present. As we need to fit the GDR to deduce the isospin mixing coefficient, before doing that we should separate the contribution of Silicon and Oxygen in the $LaBr_3(Ce)$ spectra. In this chapter, we will show the effort which were done to remove of the Oxygen contamination in the data or in general, the effort to find the way to separate the two contributions.

5.1 CASCADE simulation

In order to understand the fraction of Oxygen and Silicon contributions we expected in the high energy spectrum we performed some statistical model calculations using the CASCADE code. This code performs statistical model simulations of the γ-emission up to high energy (25 MeV) producing a spectrum corrected for the response function, provided as input. We performed the simulations listed in table 5.1. For the 4 beam energies we simulate both the nuclei of interest (^{60}Zn and ^{62}Zn) and the contamination nucleus (^{48}Cr). According to the percentage of contamination that has been found in the target after the analysis with the SEM technique (55), each simulated spectrum has been normalized for the related percentage that is reported in table 5.1 and automatically normalized in the code for the fusion cross-section. We also plotted the sum spectra by adding the ^{60}Zn and ^{48}Cr or ^{62}Zn and ^{48}Cr spectra.

Reaction	Beam energy	Percentage of events
$^{32}S + ^{28}Si \rightarrow ^{60}Zn$	86 MeV	(46% ^{60}Zn)
$^{32}S + ^{16}O \rightarrow ^{48}Cr$	86 MeV	(54% ^{48}Cr)
$^{60}Zn + ^{48}Cr$	86 MeV	(46% ^{60}Zn + 54% ^{48}Cr)
$^{32}S + ^{30}Si \rightarrow ^{62}Zn$	75 MeV	(58% ^{62}Zn)
$^{32}S + ^{16}O \rightarrow ^{48}Cr$	75 MeV	(42% ^{48}Cr)
$^{62}Zn + ^{48}Cr$	75 MeV	(58% ^{62}Zn + 42% ^{48}Cr)
$^{32}S + ^{28}Si \rightarrow ^{60}Zn$	110 MeV	(46% ^{60}Zn)
$^{32}S + ^{16}O \rightarrow ^{48}Cr$	110 MeV	(54% ^{48}Cr)
$^{60}Zn + ^{48}Cr$	110 MeV	(46% ^{60}Zn + 54% ^{48}Cr)
$^{32}S + ^{30}Si \rightarrow ^{62}Zn$	98 MeV	(58% ^{62}Zn)
$^{32}S + ^{16}O \rightarrow ^{48}Cr$	98 MeV	(42% ^{48}Cr)
$^{62}Zn + ^{48}Cr$	98 MeV	(58% ^{62}Zn + 42% ^{48}Cr)

Table 5.1: In table are listed the statistical model calculations performed using the CASCADE code and the fraction of events considered in each reaction following the indication of the percentage of nuclei present in the target (55).

In figure 5.1 the comparison between the spectra for different compound nuclei is reported. We compare the spectrum of $^{60,62}Zn$ with that of ^{48}Cr and their sum for the 4 beam energies. We can easily notice that the ^{48}Cr contribution is present at each energy of the spectrum and the difference in shape and yield between ^{48}Cr and $^{60,62}Zn$. In the case of ^{62}Zn, both at $E_{beam} = 75$ MeV and $E_{beam} = 98$ MeV, the yields differ from those for ^{48}Cr in the region of the GDR between 10 and 30 MeV. The difference is sizeable and amounts to $\approx 60\%$ for 75 MeV and 70% for 98 MeV. In the case of ^{60}Zn, instead, the region of the GDR is very similar to that of ^{48}Cr and the difference is mainly visible between 4 to 10 MeV, even if for the 110 MeV the spectra are almost overlapping. In figure 5.2 we show the ratio between the ^{48}Cr and the $^{60,62}Zn$ for the 4 beam energies. As just deduced previously, the contribution of oxygen is always present and in the region of GDR it is more significant for the the ^{60}Zn nucleus at both temperatures. These spectra confirm us that in the high energy spectra we can expect a not negligible contribution of ^{48}Cr events at all energies for all reactions. At this point, we need to find a way to discriminate the two contributions from the experimental point of view.

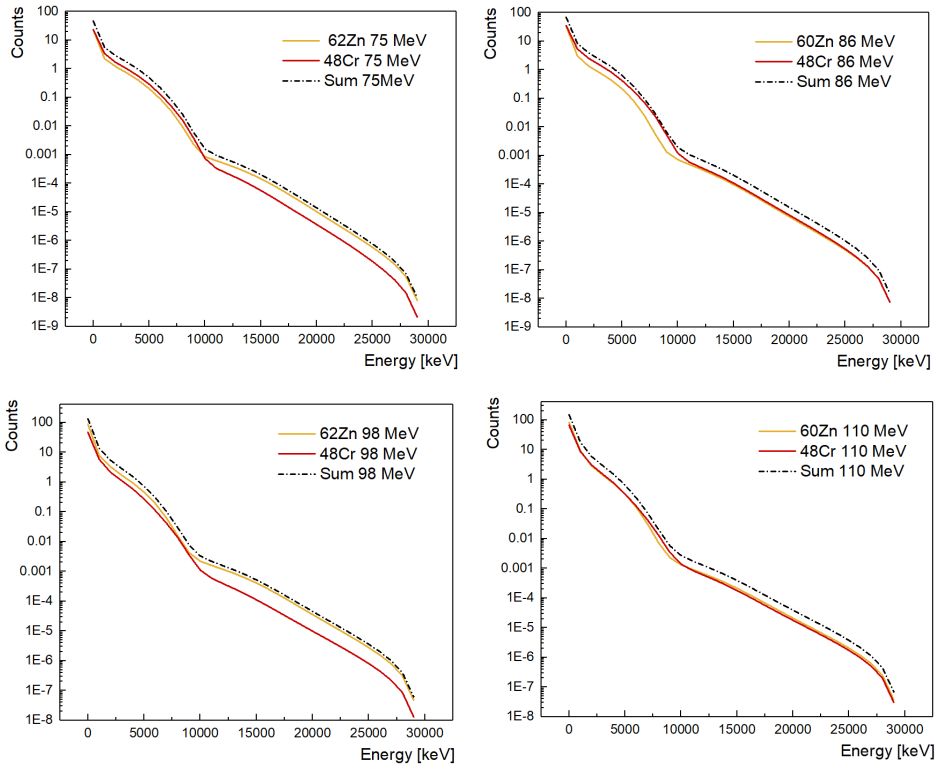

Figure 5.1: Comparison between the $^{60,62}Zn$ and ^{48}Cr yields and the sum spectra $^{60,62}Zn$ + ^{48}Cr yields for 4 beam energies.

5.2 Experimental fold selection

One of the possibilities to discriminate the contribution of Oxygen in the high energy spectra is to study the spin distributions of ^{60,62}Zn and ^{48}Cr. In figure 5.3 the spin distributions obtained through the CASCADE code, for ^{60,62}Zn and ^{48}Cr at the two lower energies are displayed. The red line shows the spin distribution of ^{48}Cr at 86 MeV beam energy and the red dot-dashed line is related to ^{60}Zn at the same energy. The blue line and the blue dot-dashed line are respectively the spin distributions of ^{48}Cr and ^{62}Zn at 75 MeV beam energy. The integral of the spin distributions correspond with the fusion cross-section of the related nucleus. We can immediately notice that the cross-section of the contaminant is higher than the cross-section of the nucleus of interest. On the other hand the maximum of the distributions for ^{60}Zn and ^{62}Zn compound nuclei are higher than those of ^{48}Cr. From an experimental point of view, the angular momentum of the nucleus

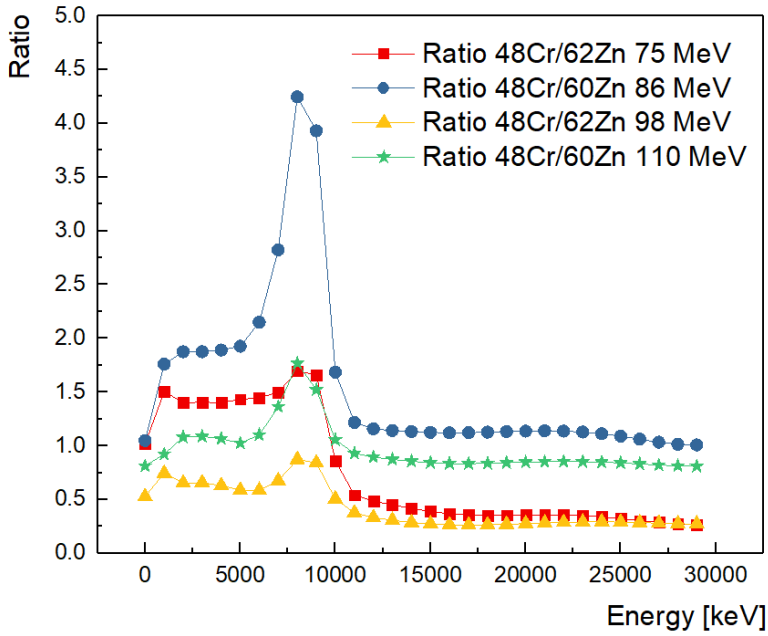

Figure 5.2: Ratio between the ^{48}Cr and the $^{60,62}Zn$ for the 4 beam energies. As just deduced previously the contribution of oxygen is always present and in the region of GDR it is more significant for the ^{60}Zn nucleus at both temperatures.

could be extracted by counting the number of γ-rays emitted in the compound nucleus decay, i.e. the so-called γ-ray multiplicity (M). However, the number of γ-rays detected by the apparatus, the so-called γ-ray fold F, is obviously different and generally less than M, because of the apparatus efficiency and response. In particular, a specific F corresponds to a M distribution. Therefore, if we can select a particular fold, we are indirectly selecting an angular momentum window and thus we could find a fold that reduces the contamination of ^{48}Cr.

In figure 5.4 the fold distribution of the GALILEO Array for the reaction ^{32}S (75 MeV) + ^{30}Si $\rightarrow$ ^{62}Zn (mixed with ^{32}S (75 MeV) + ^{16}O $\rightarrow$ ^{48}Cr) is shown. We can see that most events are up to fold 3, after that the statistic begins to be low. We produced 3 spectra selecting the GALILEO fold $F \geq 1$, $F \geq 2$ and $F \geq 3$ and asking a coincidence with $LaBr_3(Ce)$ array with E_γ between 4 and 10 MeV in order to see the change in the fraction of events coming from ^{62}Zn and ^{48}Cr. Moreover, we create a spectrum with $F \geq 1$ and the coincidence with $LaBr_3(Ce)$ array with E_γ between 10 and 20 MeV. We cannot show the same spectra with

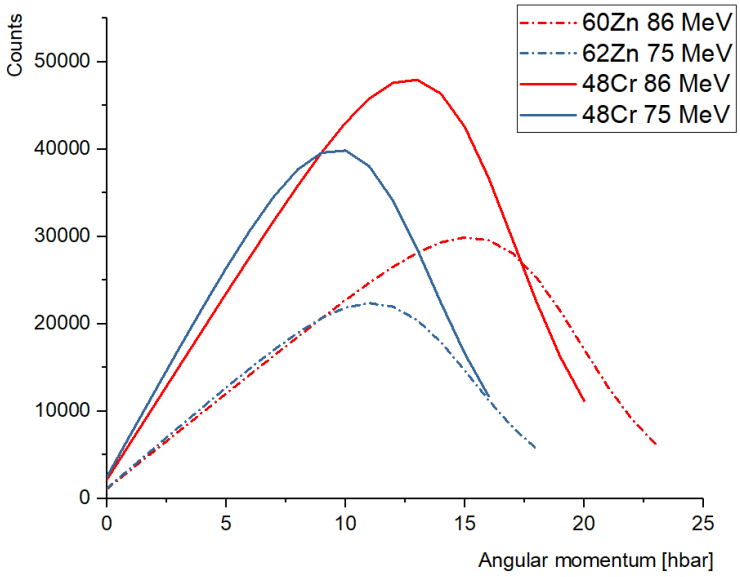

Figure 5.3: Spin distributions, obtained with the CASCADE code, for ^{60}Zn (red dot-dashed line), ^{48}Cr (red line) at a beam energy of 86 MeV, ^{62}Zn (blue dot-dashed line) and ^{48}Cr (blue line) at beam energy of 75 MeV.

higher fold because of a lack of statistic. In table 5.2 the integrals of the spectra are listed for fold and range selection. As anticipated, the number of counts for the fold 2 and fold 3 with the high energy range coincidence, are too low for the visualization of the spectra. We defined the coincidence with two energy intervals of $LaBr_3(Ce)$ spectra because the lower is essential for the normalization between the experimental spectrum and the simulation and the higher interval is the region of GDR.

	Fold 1	Fold 2	Fold 3
Range 4-10 MeV	$2.8 * 10^6$	$3.3 * 10^5$	$2.2 * 10^4$
Range 10-20 MeV	10^4	10^3	/

Table 5.2: This table lists the integrals of the spectra, associated to different values of fold and energy. The number of counts for the fold 2 and fold 3 in the high energy interval, are too low for their visualization in the spectra.

In figure 5.5 the 4 spectra (for the reaction ^{32}S (75 MeV) + (^{30}Si + ^{16}O) $\rightarrow$ ^{62}Zn + ^{48}Cr) just described are presented. The first one (red) is the total spectrum (asking

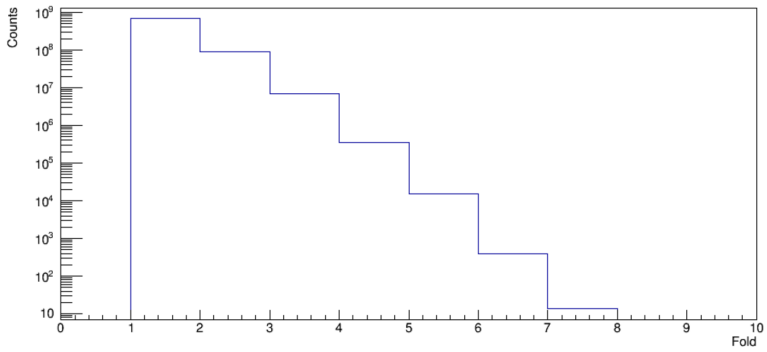

Figure 5.4: Fold distribution of the GALILEO Array for the reaction ^{32}S (75 MeV) + $^{30}Si \rightarrow {}^{62}Zn$ (mixed with ^{32}S (75 MeV) + $^{16}O \rightarrow {}^{48}Cr$)

$fold \geq 1$) in coincidence with low-energy transitions measured in the $LaBr_3(Ce)$ array. The yellow and the black ones have the same coincidence condition with $LaBr_3(Ce)$ array but different condition on fold, namely $fold \geq 2$ and $fold \geq 3$. The last spectrum (green) is in coincidence with the high energy γ-rays in $LaBr_3(Ce)$ and has the condition $fold \geq 1$ in GALILEO. The blue circles and the blue stars identify respectively the transitions coming from the residual nucleus ^{59}Ni that belongs to the decay of ^{62}Zn and the transition coming from the residual nucleus ^{46}Ti that belongs to the decay of ^{48}Cr. We can notice that the relative intensities of the two transitions don't change significantly in the 4 spectra and that the fold selection is not the viable solution to disentangle the contributions of ^{62}Zn respect to ^{48}Cr .

5.3 Gate on ^{62}Zn and ^{48}Cr transitions

Another possibility to separate the two components is to observe the high energy spectrum of $LaBr_3(Ce)$ detectors in coincidence with a particular transition in Germanium detectors. If we select a transition in the GALILEO spectrum that belongs to the nucleus of interest and we plot the spectrum of $LaBr_3(Ce)$ in coincidence we could obtain a high energy spectrum that contains only events related to the ^{62}Zn. We, therefore, selected the main transition of the most populated residual nucleus both for the reaction with ^{62}Zn and ^{48}Cr. For the first one, the most populated nucleus is the ^{59}Ni and we gated on the transition to the ground state, namely 339 keV; for the second one, the transition to the ground state is the 889 keV line related to the ^{46}Ti.
In figure 5.6 the comparison between the $LaBr_3(Ce)$ spectra gated on the two transitions on GALILEO spectra is displayed. Unfortunately, the statistic is too

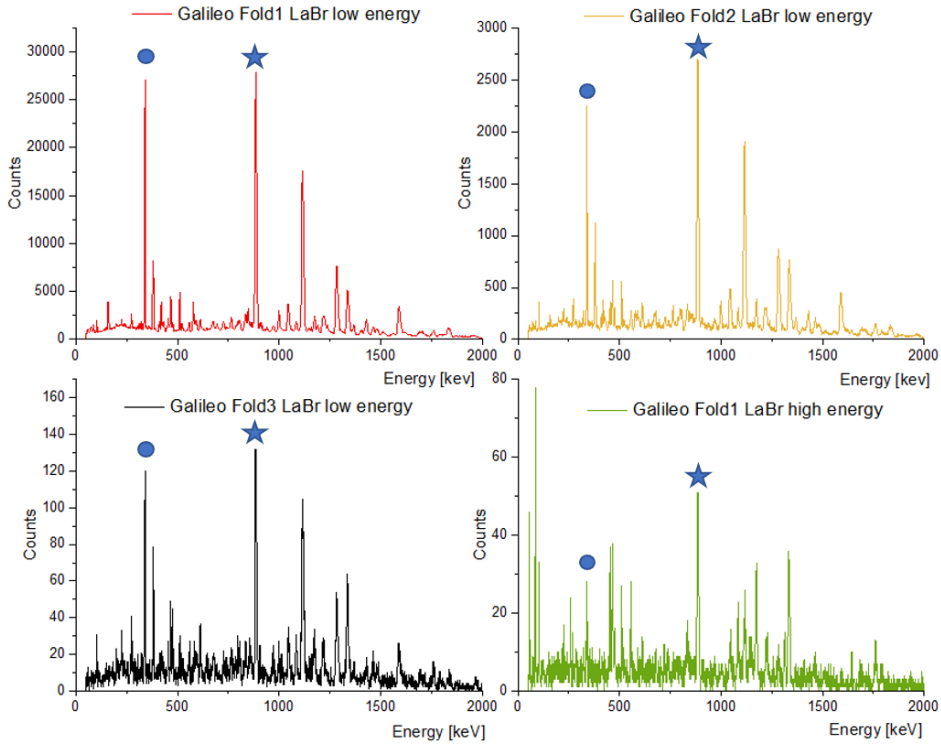

Figure 5.5: Galileo spectra for different folds and in coincidence with $LaBr_3(Ce)$ array. The first one (red) is the total spectrum (asking $fold \geq 1$) and in coincidence with γ-rays in $LaBr_3(Ce)$ array. The yellow and the black ones have the same coincidence condition with $LaBr_3(Ce)$ array and the condition of $fold \geq 2$ and $fold \geq 3$ in GALILEO. The last spectrum (green) is in coincidence with the high energy transitions in $LaBr_3 : Ce$ and the condition $fold \geq 1$ in GALILEO. The blue circles and the blue stars identify respectively the transitions coming from the residual nucleus ^{59}Ni that belong to the decay of ^{62}Zn and the transitions coming from the residual nucleus ^{46}Ti that belong to the decay of ^{48}Cr. The relative intensities of the two peaks don't change significantly in the 4 spectra and thus, the fold selection is not the viable solution to separate the contributions of ^{62}Zn and ^{48}Cr.

low and the high energy part of the spectra is completely not visible. We understand, therefore, that this way to discriminate the two contributions is not a valid option to obtain a γ-ray energy $LaBr_3(Ce)$ spectrum from which extract the mixing probability. We can, however, use this result to get other informations. We

can immediately realize that from 3 MeV the contribution to the spectrum due to the residual nucleus of ^{48}Cr, the ^{46}Ti is higher than the contribution of ^{59}Ni, the residual nucleus of ^{62}Zn. In order to better understand this behaviour, we used GEMINI++ simulation code that with a Monte-Carlo procedure determines the decay sequence of an excited nucleus. We simulated the two reactions and after the selection of the residues of interest, we plotted the gamma spectra, to be compared with the experimental ones. From an experimental point of view, due to the acquisition trigger, the request of the coincidence and the efficiency of the apparatus we are sensible only to a certain multiplicity and as a consequence to a certain range of angular momenta of the residual nucleus. Nuclei with higher angular momentum are indeed favoured but we can't determine the precise value of the angular momentum we are much sensitive experimentally. For this reason, we performed the simulations as a function of a selection on the angular momentum.

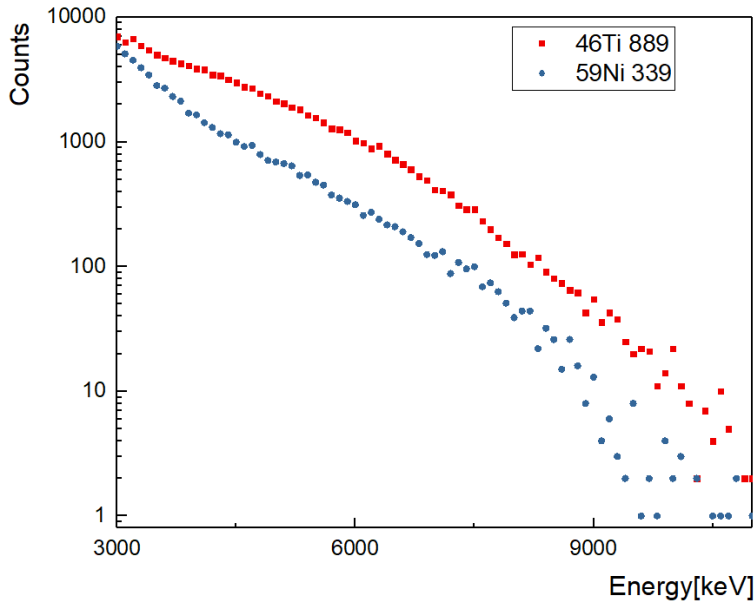

Figure 5.6: Comparison between the $LaBr_3 : Ce$ spectra gated on the transitions (^{46}Ti red and ^{59}Ni blue) on GALILEO spectrum. The error bars, corresponding to the statistical errors, are not displayed to make clearer the comparison.

In figure 5.7 the spectra with an angular momentum selection from the total to $J \geq 8$ with single step are compared. On the left, we compare the spectra for the nucleus ^{46}Ti and on the right for ^{59}Ni. It is clear that for the ^{59}Ni the differences between spectra are not in shape but only in yield. This is not true for the ^{46}Ti,

for which we easily identify 3 different shapes. Up to $J \geq 2$ the spectra show a bump around 10 MeV, for $J \geq 3$ and $J \geq 4$ the spectra are quite flat and from $J \geq 5$ up to $J \geq 8$ there is a dip in the region around 10 MeV.
We want now compare the experimental spectra with the simulated ones. To avoid normalization errors, the best things to do is to compare the experimental and simulated ratios between the ^{46}Ti and the ^{59}Ni spectra. We made the ratios for all the possible combinations of spectra (with different angular momentum conditions) and compared with the experimental ratio. Before doing so, all the simulated spectra were normalized for the compound nucleus cross-section and the photo-peak efficiency of the two experimental transitions. The combination that better reproduce the experimental ratio is $J \geq 3$ for ^{46}Ti and $J \geq 6$ for ^{59}Ni. The comparison of these ratios is displayed in 5.8.
Unfortunately, also this way didn't allow us to separate the contribution of Oxygen.

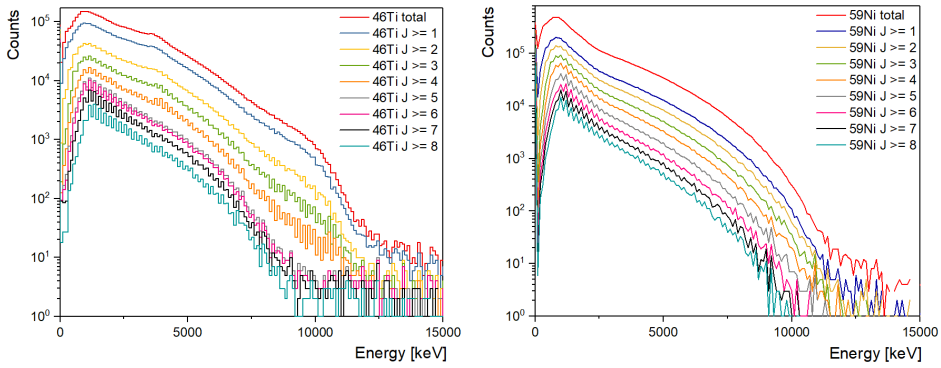

Figure 5.7: Comparison between the spectra with an angular momentum condition from the total to $J \geq 8$, in single step. On the left, we compare the spectra for the nucleus ^{46}Ti and on the right those for ^{59}Ni. For the ^{59}Ni the differences between spectra are not in shape but only in yield. For ^{46}Ti, we identify 3 different shapes: up to $J \geq 2$ the spectra show a bump around 10 MeV, for $J \geq 3$ and $J \geq 4$ the spectra are quite flat and from $J \geq 5$ up to $J \geq 8$ there is a dip in the region around 10 MeV.

5.4 Summary

All the efforts to separate the contributions of ^{48}Cr and ^{60,62}Zn, did not lead to a satisfactory result. Unfortunately, because there is no way to separate only the events related to the nuclei of interest, we can't neither use the informations related to charged particles and neutrons measured with EUCLIDES and the Neutron Wall

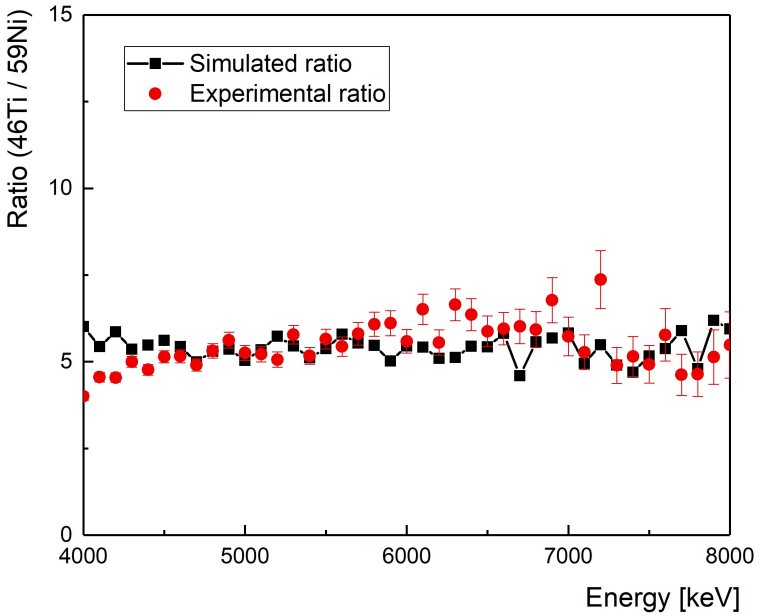

Figure 5.8: Comparison between experimental (red points) and simulated (black squares and line) ratio between the γ yields from the ^{46}Ti and ^{59}Ni compound nuclei. The combination that better reproduces the experimental ratio is $J \geq 3$ for ^{46}Ti and $J \geq 6$ for ^{59}Ni.

array. The particles selection, indeed, wouldn't allow to select one reaction rather than another, also because the decay channels are similar for the residues of both nuclei. Therefore, the preliminary analysis on these two arrays is not reported. We want to make a point on other two issues: from the analysis of the GALILEO spectrum we identified the residual nuclei produced in the reaction and it would be interesting comparing the expected percentage of population of the residual nuclei, calculated through the statistical model, with the experimental one. Unfortunately, the oxygen contamination leads to have unclear peaks of the residues of the nucleus of interest and moreover we know that the Compton suppression modified the interaction probability of γ-rays at different energies. The Compton suppression make also inaccessible the experimental spin distribution that could be passed as input in the statistical model calculation. It is, however, necessary to underline that for the goal of the analysis,EUCLIDES and Neutron Wall are ancillary arrays, such as GALILEO, because the mixing probability is extracted only from the high energy spectra measured with $LaBr_3(Ce)$ detectors.
At this point, we are forced to consider ^{48}Cr and ^{60,62}Zn in the high energy spec-

trum as a global system. We must be aware that ^{48}Cr will contribute to the isospin mixing coefficient because it is an N=Z nucleus. The analysis that follows, will consider the goal as the determination of the mixing probability of the system ^{48}Cr + ^{60}Zn (the expected values for the isospin mixing coefficients at T=0 are, however, quite similar).

CHAPTER 6

Statistical model analysis

Life is like riding bicycle, to keep your balance, you must keep moving.

Albert Einstain

In this chapter the statistical model analysis of the γ-ray spectra is reported. The analysis of the γ spectrum, produced by the statistical decay of the ^{62}Zn compound nucleus, provides the GDR parameters, while the analysis of the γ spectrum, produced by the statistical decay of the ^{60}Zn compound nucleus, provides the value of the isospin mixing coefficient, keeping in mind the oxygen contamination of the target. Therefore, we need to perform a statistical model analysis through the "CASCADE" statistical model code. In the first part we will describe the statistical model code CASCADE and in the second part the application to the experimental spectra.

6.1 Statistical model with Isospin

As anticipated, the CASCADE code has been used to perform the statistical model analysis. The original version of the code (59) has been modified first from M.N.Harakeh (60) and then by the Washington university group (4) in order to implement the isospin symmetry in this way:

- the population cross section matrices and level densities are labled with the quantum number for isospin (in addition to excitation energy, angular momentum and parity)
- the isospin mixing is applied to the nucleus before the decay process occur
- the transmission coefficients are multiplied by isospin Clebsch-Gordan coefficients

The determination of the isospin mixing coefficient follows the parametrization of Harney, Ritcher and Weidenmüller (61) as explained in section 1.3.5 for which we have the definition of two classes of isospin, $I_< = I_z$ and $I_> = I_z + 1$ and thus, two Coulomb spreading widths $\Gamma^{\downarrow}_<$ and $\Gamma^{\downarrow}_>$ and two isospin mixing coefficients $\alpha^2_<$ (that represents the probability that the state $I_<$ is mixed with the state $I_>$) and $\alpha^2_>$ (that represents the probability that the state $I_>$ is mixed with the state $I_<$). In general the initial compound nucleus is populated in the state $I_< = I_z$. States with $I > I_z$ correspond to configurations with a higher excitation energy. The energy of the $I_>$ states are calculated as the energy of the equivalent state in the isobaric analogue nucleus with the same mass A but with Z = Z-1 and N = N + 1, using the formula

$$\Delta_{I_< I_>} = M(A_{analog}) - M(A) + \Delta E_C - (m_n - m_p) \tag{6.1}$$

where ΔE_C is the difference of the Coulomb energy of the two nuclei, while the quantity $(m_n - m_p)$ takes into account the difference in mass between neutrons and protons. For the ^{60}Zn nucleus the parameters are listed in table 6.1.

Nucleus	$M - M_{analog}$	ΔE_c	$m_n - m_p$	$\Delta^{theo}_{I_< I_>}$	$\Delta^{exp}_{I_< I_>}$
^{60}Zn	-4,2	9.9	0,782	5	4.9

Table 6.1: Mass difference between the isobar doublet,ΔE_c, proton-neutron mass difference used to calculate the energy of the IAS $\Delta^{theo}_{I_< I_>}$ with Eq.6.1. The theoretical value is compared with the measured one. All the values are in MeV. Taken from (62)

For each excitation energy E* and angular momentum J, the level density is calculated with the Reisdorf approach:

$$\rho(E^*, J) = \frac{2J+1}{12\Theta^{3/2}} \frac{\sqrt{a}\, exp(2\sqrt{aU})}{U^2} \tag{6.2}$$

where,

$$\begin{aligned} U &= E^* - E_{rot} + \delta P \\ E_{rot} &= \frac{J(J+1)\hbar^2}{2\Theta} \\ aU &= \tilde{a}[U + \delta U[1 - exp(-\gamma U)]] \end{aligned} \tag{6.3}$$

γ is the damping parameter, $\tilde{a}$ the level density parameter, Θ the moment of inertia $\Theta = \frac{2J}{\hbar^2}$ and δP is the pairing correction.

The main input parameters of the statistical model calculations are: Z and A of the projectile, Z and A of the target, energy of the impinging beam, the Coulomb spreading width $\Gamma^{\downarrow}_{>}$ (the $\Gamma^{\downarrow}_{<}$ is calculated in the code with the equation 1.45) and the strength, the centroid and the width of the GDR.

6.2 Analysis

The goal of this part of analysis is to extract the best fitting value of the Coulomb spreading width $\Gamma^{\downarrow}_{>}$ (defined in section 1.3.5) in order to evaluate the degree of mixing in the ^{60}Zn nucleus. The procedure follows the steps listed below:

- Fit of GDR parameters (strength, width and centroid) using the ^{62}Zn data
- Apply the GDR parameters to the ^{60}Zn spectrum and fit the Coulomb spreading width as the only free parameter
- From the Coulomb spreading width, extract the mixing probability

6.2.1 Fit of ^{62}Zn

The statistical model provides the γ-ray spectrum produced during the decay of a CN, which was compared with the experimental data. The statistical model spectra were folded with the detector response function and normalized to the experimental data at around 5-6 MeV. Because of the exponential nature of the spectra, the standard χ^2 is not a suitable quantity because of its weak sensitivity to the low yield part of the spectrum. For this reason, the fit minimization was applied to a Figure Of Merit (FOM) defined as:

$$FOM = \sum_{E=12MeV}^{E=17MeV} \frac{(Y_i - M_i)^2}{Y_i^2} \tag{6.4}$$

where Y_i and M_i are the experimental and simulated counts per bin, respectively. Practically, the FOM was obtained dividing the standard χ^2 over the number of counts for each bin. In this way, the sensitivity to the low yield part of the spectrum is increased. In order to consider, in the fitting process, the statistical error of the experimental spectrum, 10^4 spectra were created adding to the number of the experimental counts a fluctuation randomly extracted from a Gaussian distribution centred at zero and with a standard deviation equal to the statistical error on the number of counts per bin ($\sigma = \sqrt{Y_i}$). Each of the 10^4 spectra was compared with n CASCADE simulations, varying in GDR parameters. The simulations were performed only for the ^{62}Zn and not for ^{48}Cr. In order to reduce the effect of ^{48}Cr in the γ spectrum, the energy region for the minimization of the FOM was chosen

between 12 and 17 MeV. Because of the few points for the minimization, only two GDR parameters were varied, the centroid and the width, keeping constant the strength, set to 90%, as in ref. (32, 33). Figure 6.1 displays the histograms with the frequencies for which a certain combination of centroid and width correspond to the minima of the FOM for the spectrum of ^{62}Zn at T=2 MeV (on the left) and for the spectrum of ^{62}Zn at T=2.4 MeV (on the right). We can deduce that for the lower temperature the best fit turns to be $E_{GDR} = 18.45$ MeV and $\Gamma_{GDR} = 11.6$ MeV and for the higher temperature the best fit turns to be $E_{GDR} = 18.1$ MeV and $\Gamma_{GDR} = 12.6$ MeV.

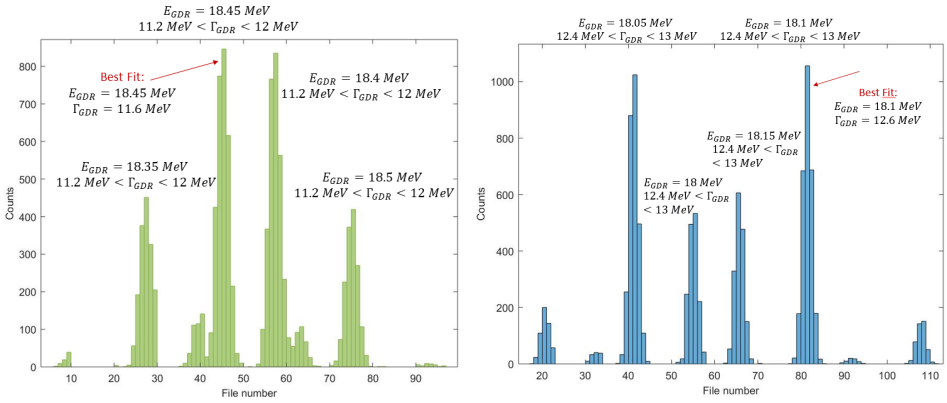

Figure 6.1: Histograms with the frequencies with which a certain combination of centroid and width resulted to be the minima of the FOM for the ^{62}Zn at T=2 MeV (on the left) and for ^{62}Zn at T=2.4 MeV (on the right). For the lower temperature the best fit is $E_{GDR} = 18.45$ MeV and $\Gamma_{GDR} = 11.6$ MeV and for the higher temperature it is $E_{GDR} = 18.1$ MeV and $\Gamma_{GDR} = 12.6$ MeV. The main 4 peaks on the left are in order the groups with $E_{GDR} = 18.35$ MeV, $E_{GDR} = 18.45$ MeV,$E_{GDR} = 18.4$ MeV and $E_{GDR} = 18.5$ MeV with the width varying between 11.2 and 12 MeV, whilst on the right the groups with $E_{GDR} = 18.05$ MeV, $E_{GDR} = 18.0$ MeV,$E_{GDR} = 18.15$ MeV and $E_{GDR} = 18.1$ MeV with the width varying between 12.4 and 13 MeV.

We can notice that the main 4 peaks on the left part of figure 6.1 represent, in increasing order, the groups with $E_{GDR} = 18.35$ MeV, $E_{GDR} = 18.45$ MeV,$E_{GDR} = 18.4$ MeV and $E_{GDR} = 18.5$ MeV with the width varying between 11.2 and 12 MeV, whilst the 4 main peaks on the right part of figure 6.1 represent, in increasing order, the groups with $E_{GDR} = 18.05$ MeV, $E_{GDR} = 18.0$ MeV,$E_{GDR} = 18.15$ MeV and $E_{GDR} = 18.1$ MeV with the width varying between 12.4 and 13 MeV.

To obtain the error bars on the GDR parameters we produced a 3D histogram with

the occurrences of the FOM minimization as a function of each couple (E_{GDR}, Γ_{GDR}). The histogram for ^{62}Zn at T=2 MeV is visualized in the left side of figure 6.2 and for the compound nucleus ^{62}Zn at T=2.4 MeV in figure 6.3. In general, we have noticed that increasing the centroid, to obtain a good fit we need to reduce the width. The projections on the x and y axis of the 3D plots in the left part of the figures 6.2 and 6.3 are shown in the right part of the same figures. On the top there is the distribution of the GDR centroid and on the bottom the distribution of the GDR width. The Gaussian fit centred in the best value is also shown. The Full Width Half Maximum of the Gaussian represents the error in the centroid and width reported in table 6.2. In table 6.2 we have therefore reported, the fitting values of the centroids and widths using only one decimal digit.
In figure 6.4 the ^{62}Zn experimental point and the best fit is shown for T=2 MeV on the left and T=2.4 MeV on the right. We can observe that, even if we know that there is the oxygen contamination, the GDR experimental spectra are well fitted by the statistical model calculations for the nucleus ^{62}Zn.

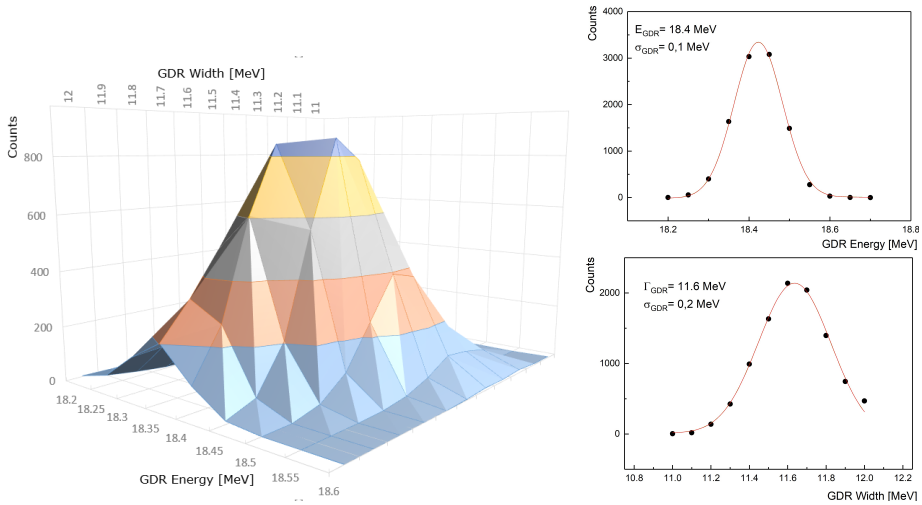

Figure 6.2: Distribution of parameters for ^{62}Zn at T=2.0 MeV (top : GDR energy, bottom: GDR width) obtained from the FOM minimization as described in the text, together with the Gaussian fit (line).

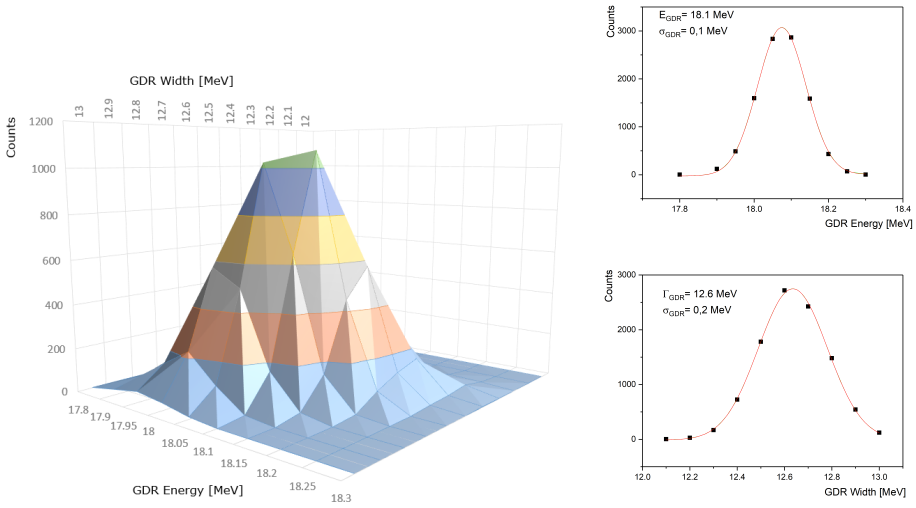

Figure 6.3: Distribution of parameters for ^{62}Zn at T=2.4 MeV (top : GDR energy, bottom: GDR width) obtained from the FOM minimization as described in the text, together with the Gaussian fit (line).

Temperature	$E_{GDR}(MeV)$	$\Gamma_{GDR}(MeV)$	$S_{GDR}(\%)$
2 MeV	18.4 ± 0.1	11.6 ± 0.2	90
2.4 MeV	18.1 ± 0.1	12.6 ± 0.2	90

Table 6.2: GDR parameters obtained for ^{62}Zn at T=2 MeV and T=2.4 MeV

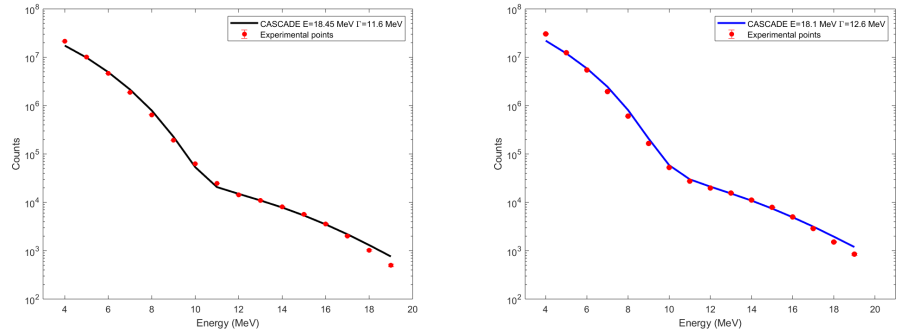

Figure 6.4: Experimental spectra (points) for ^{62}Zn an at different energies and the best fit with statistical model (lines). Data and calculations at T=2 MeV are on the left and those at T=2.4 MeV are on the right.

6.2.2 Fit of ^{60}Zn

We now assume that the GDR parameters in the nucleus ^{62}Zn and in ^{60}Zn are similar enough, that we can apply the parameters deduced in the previous section to the nucleus ^{60}Zn. In this way, the only free parameter is the Coulomb spreading width. Following the same procedure used for ^{62}Zn, we produced 10^4 spectra adding the fluctuation randomly extracted from a Gaussian distribution and we compared all of them with CASCADE simulations, varying the Coulomb spreading width from 0 to 50 keV. In this analysis we considered the same Coulomb spreading width for all the nuclei populated along the decay cascade. In fact, we are not sensitive to the degree of mixing after the first step, because, after one proton or neutron emission, the self-conjugate nucleus CN has $I_< \neq 0$. Instead of performing the minimization of the FOM on the energy spectrum of ^{60}Zn we decided to analyse the ratio $^{60}Zn/^{62}Zn$. This approach let us to reduce the possible systematic errors and the effect of the Oxygen contamination that could be present in the two spectra. The experimental ratio, for T=2 MeV temperature, is shown in figure 6.5 together with the statistical model (CASCADE) ratios corresponding to different Coulomb spreading width values. It is important to underline that the Coulomb spreading widths defined as input of the statistical model are the widths for the $I_z + 1$ states, namely $\Gamma^{\downarrow}_{>}$. The $\Gamma^{\downarrow}_{<}$ is deduced in the code through the equation 1.45. The blue dashed line and the green dot-dashed lines are respectively the ratios with CSW=0 keV and CSW=50 keV (the maximum possible value). The red, yellow and violet line are instead, respectively, the ratios with CSW=5 keV, CSW=10 keV and CSW=15 keV. We can notice that, in this case, we can perform a minimization of χ^2 in the energy range between 12 MeV and 19 MeV, including the two last points, neglected in the fit of the ^{62}Zn spectrum. With this technique, the comparison between experimental and simulations spectra gives a good match and the result of the minimization of the χ^2 is $CSW = 5 \pm 3$ keV.

At T=2.4 MeV, the statistical model prediction of the γ spectrum of the nucleus ^{60}Zn is different from the measured data. In particular, the data shows a strong emission from 4 to 9 MeV not accounted by the statistical model. As the theoretical and experimental spectra are normalized in the energy region between 5-6 MeV, this results in a mismatch between the data and the statistical model calculation. In order to better understand this effect, in December 2018 we acquired new data, taking the opportunity to perform a measurement with a non contaminated target. This new measurement would have allowed us, on one side, to compare the new spectra with the ones of the experiment performed in 2016 and deduce the real effect of the contamination on the high energy spectra and, on the other side, to check the spectra in the normalization region. For this reason we produced the reaction

$^{32}S+^{28}Si \rightarrow^{60} Zn$ at T=2.4 MeV ($E_{beam} = 110MeV$). We have dedicated the next chapter to the description of this new experiment and the preliminary analysis.

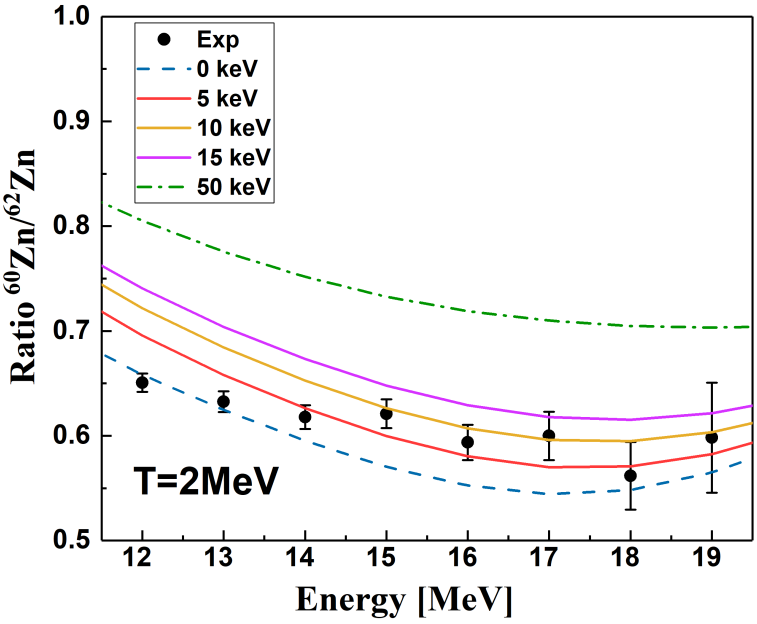

Figure 6.5: Experimental ratio $^{60}Zn/^{62}Zn$ together with the statistical model ratios with different Coulomb spreading width values for the reaction at T=2 MeV. The blue dashed line and the green dot-dashed line are respectively the ratios with CSW=0 keV and CSW=50 keV (the maximum possible value). The red, yellow and violet line are instead respectively the ratios with CSW=5 keV, CSW=10 keV and CSW=15 keV.

CHAPTER 7

The second experiment

Isn't it nice to think that tomorrow is a new day with no mistakes in it yet?

L.M. Montgomery

The data taking was performed at Laboratori Nazionali di Legnaro with an experimental set-up composed by the GALILEO array and only 7 $LaBr_3(Ce)$ detectors. In the measurement a natural Silicon target has been used. Unfortunately, we were able to perform only a small part of the experiment because the Tandem of the laboratory had a failure. We measured the reaction $^{32}S + ^{28}Si \rightarrow ^{60}Zn$ at T=2.4 MeV (E_{beam} = 110 MeV), but the accelerator broke before we could perform the energy calibration.

7.1 Analysis of the target

The target was composed by 97% of ^{28}Si, 2% of ^{29}Si and 1% of ^{30}Si. In this part we analyse the effect of Si isotopes contaminants on the Coulomb Spreading Width. In order to do that, 3 spectra, one for each isotope, were simulated using CASCADE code imposing a Coulomb Spreading Width of 5 keV. All these spectra are summed, each with the relative fraction, to produce one spectrum. The resulting spectrum is what is expected from the experiment. The same procedure described in 6.2.2 was applied. Namely, performing a Monte-Carlo simulation, 10^4 spectra were created adding to the number of counts, of the previous spectrum, a fluctuation randomly extracted from a Gaussian distribution with the statistical error on the number of counts per bin ($\sigma = \sqrt{N}$) as standard deviation. All these spectra were compared with CASCADE simulations, having different Coulomb Spreading Width, in order to deduce the CSW value that minimizes the differences between them. The minimization procedure is the same used in 6.2.2. The input value of

the CSW was 5 keV but as reported in figure 7.1, that shows the CSW value which better reproduce the simulation, a maximum at 6 keV is obtained.

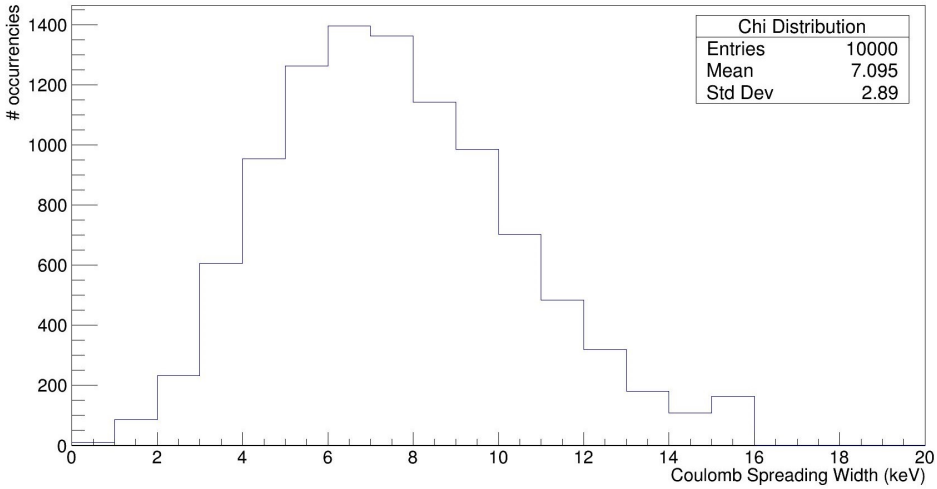

Figure 7.1: Number of occurrences, over 10^4 spectra. The discrepancy from 5 keV give us information about the error on CSW caused by the presence of contaminants in the target. A maximum at 6 keV is obtained.

7.2 Response function

A described in section 4.1.3, we simulated the response function also for this detectors configuration, following the same method. In this second experiment, the $LaBr_3(Ce)$ detectors were located at 90° respect to the target, surrounding the Pb collimators normally used for GALILEO array. We are interested in understanding the effect of the collimators on the response function. In figure 7.3 a comparison between the response function with and without collimators is shown for 3 energies as an illustration. The only modification in the shape is at very low energy, namely under one MeV. Therefore, we can't see a significant change in the behaviour of detectors of the two experimental set-up.

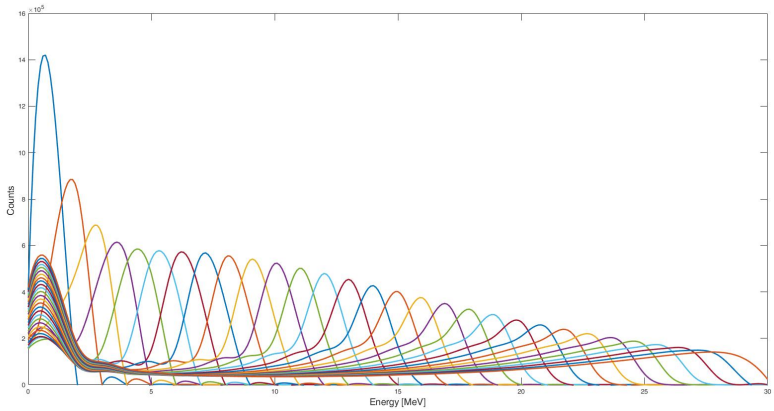

Figure 7.2: Simulation of γ-rays interactions, from 1 to 30 MeV, in $LaBr_3(Ce)$ array.

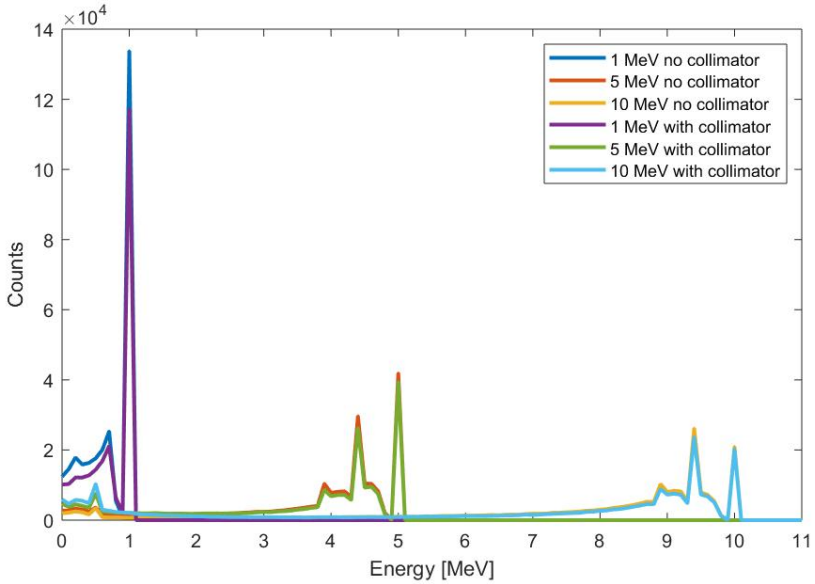

Figure 7.3: Comparison between the RF with and without collimators for 3 energies. Besides a difference in the number of events, that is lower in case of collimators simulations as expected, the only modification in the shape is at very low energy, below one MeV. Theres no evidence of a significant change in the behavior of detection.

7.3 Residual nuclei

The γ-ray spectrum of the GALILEO array, associated to the reaction ^{32}S + ^{28}Si $\rightarrow^{60}$Zn with E$_{beam}$ = 110 MeV, is displayed in figure 7.4. Using the RadWare (54) and NuDat (64) archives as a reference, the main intense peaks were identified. The five main residues produced in the ^{60}Zn decay are reported in table 7.1, together with the corresponding decay channels and the energy of transition from the first excited state to the ground state. In figure 7.4 each identified transition is marked with the energy, the states of the transition and the nucleus. The marks in the coloured boxes describe the transitions to the ground state for the five residual nuclei. The red boxes identify, instead, the peaks associated with the nucleus ^{54}Fe that is populated in an isomeric state as described also in the previous experiment. We have here, the demonstration that in this target there's no sign of any contamination, because all the transition identified belong to the nucleus of interest ^{60}Zn. In figure 7.5 there is the comparison between the GALILEO spectrum measured in the 2016 experiment and the one measured in 2018. We can immediately notice that some peaks visible in 2016 do not have a correspondence in 2018 data. These transitions belong to the oxygen contamination.

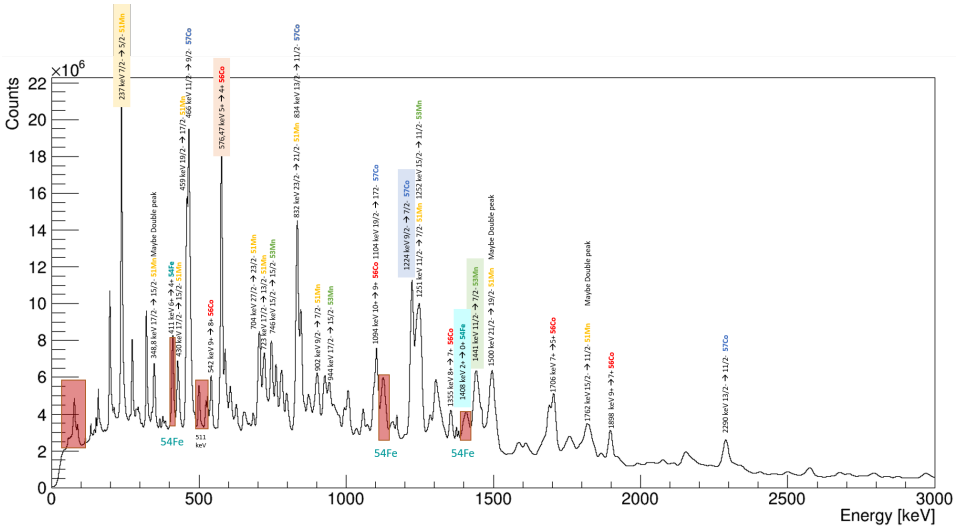

Figure 7.4: The γ-ray spectrum of the GALILEO array, associated to the reaction ^{32}S + ^{28}Si $\rightarrow$ ^{60}Zn with E_{beam} = 110 MeV.

Nuclei	decay mode	Transition to the GS
^{57}Co	3p	1224 keV
^{56}Co	3p + 1n	576 keV
^{54}Fe	1α + 2p	1408 keV
^{53}Mn	1α + 3p	1441 keV
^{51}Mn	1α + 1p	237 keV

Table 7.1: Main residual nuclei observed from the decay of ^{60}Zn, with their population mode and the energy of the transition from the first excited state to the ground state.

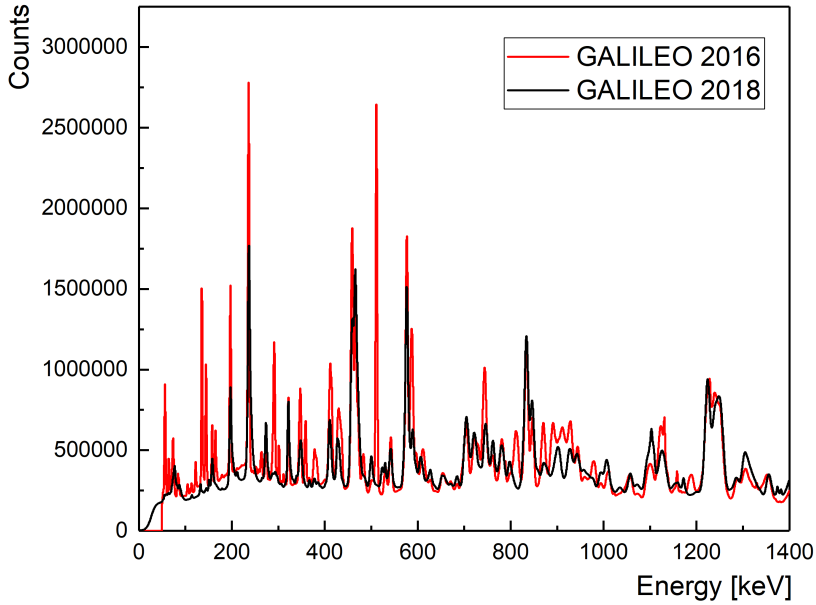

Figure 7.5: Comparison between the GALILEO spectrum detected in the 2016 experiment (red line) and in that detected in 2018 (black line). Transitions that belong to the oxygen contamination are visible only in the 2016 spectrum and they don't have a correspondence in the 2018 spectrum.

7.4 $LaBr_3(Ce)$ spectrum

The experiment in 2018 ended before the calibration at high energy could be made. We had only calibration performed with standard sources, namely ^{137}Cs (E_γ= 661.7 keV) ^{60}Co (E_γ= 1173.2 keV and 1332.5 keV) and $^{241}Am-Be(Fe)$ radioactive sources that we used to calibrate the lower part of the $LaBr_3(Ce)$ spectra. Moreover, we identified some transitions coming from residual nuclei (^{57}Co and ^{51}Mn) up to around 3 MeV detected by $LaBr_3(Ce)$ that we used to have more points for the calibration. It is well known that $LaBr_3(Ce)$ detectors suffer from a strong non-linearity at high energy (65) and using the calibration point we hold, we could obtain an alignment only up to 7 MeV for the 7 $LaBr_3(Ce)$ spectra as shown in figure 7.6.

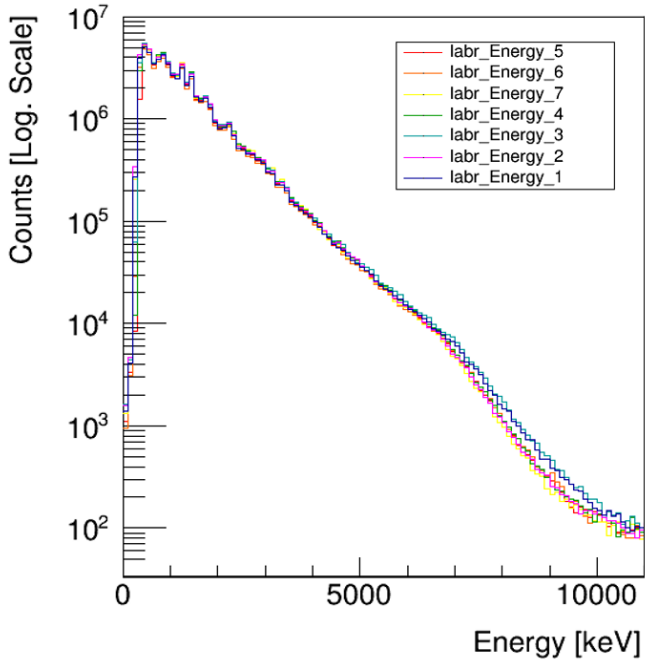

Figure 7.6: Comparison between the 7 $LaBr_3(Ce)$ spectra. The calibration performed is correct up to 7 MeV.

Even if the spectrum of 2018 measurement is properly calibrated up to 7-8 MeV, we can compare the total $LaBr_3(Ce)$ spectrum of 2016 to the one of 2018, because the calibrated region include the normalization one. The comparison is shown in

figure 7.7. and we can notice that in the region between 5 to 6 MeV the number of counts are different. The spectrum acquired in 2016 seems to have an emission in this region that led to have more counts than expected. We cannot establish if this emission belongs to the oxygen contamination or to other events not related to the decay of the compound. This can explain the difference between the measured spectrum of 2016 and the prediction of the statistical model. Because the ratio between the integrals in the normalization region (5-6 MeV) between the two spectra (2016/2018) turns to be 1.29, we assume that the normalization in 2016 is overestimated by a factor 1.29 and we use this normalization to perform the ratio.

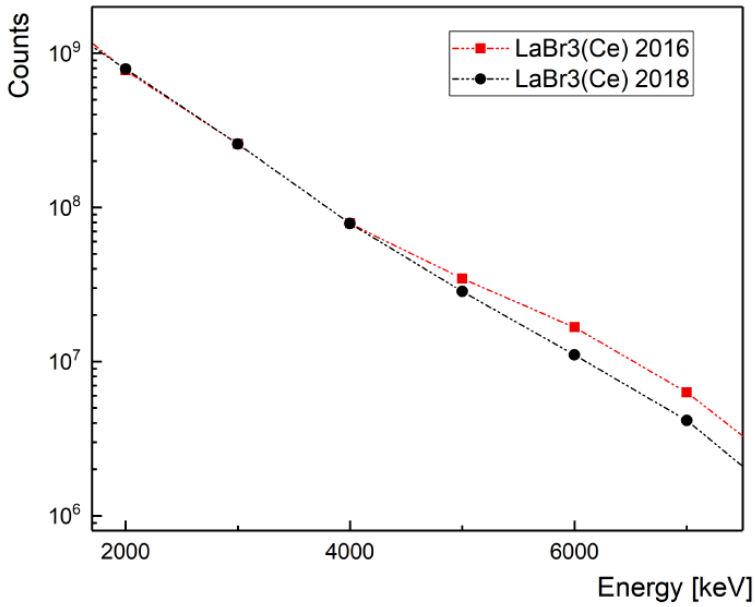

Figure 7.7: Comparison between the $LaBr_3(Ce)$ spectrum of the experiment in 2016 (red) with the spectrum of the experiment 2018 (black). In the region between 5 to 6 MeV the number of counts are different. The ratio between the integrals in the normalization region between the two spectra (2016/2018) is 1.29.

The ratio obtained for the T=2.4 MeV nucleus is shown in the lower part of figure 7.8 together with the ratio already shown for T=2 MeV in the upper part of the figure. The two experimental ratios of figure 7.8 seems to have a very similar trend and a good agreement with the predicted ratios. The result of the χ^2 minimization for the ratio at T=2.4 MeV is $CSW = 7 \pm 3$ keV. The values listed in table 7.2 summarizes the Coulomb spreading widths ($\Gamma^{\downarrow}_{>}$) obtained for the two temper-

Nucleus	T [MeV]	$\Gamma^{\uparrow}_{CN}[keV]$	$\Gamma^{\downarrow}_{>}[keV]$
^{60}Zn	2	107	5 ± 3
^{60}Zn	2.4	189	7 ± 3

Table 7.2: Compound nucleus decay widths $\Gamma^{\uparrow}_{CN}$ (averaged over J) and Coulomb spreading widths $\Gamma^{\downarrow}_{>}$ for the nucleus ^{60}Zn at both temperatures.

atures. The error bars are obtained by the combination of two different errors: the first one comes from the propagation of the errors in the determination of the GDR parameters and the second one by the minimization procedure. In the same table the compound nucleus decay widths for the two temperatures are reported. The compound nucleus decay widths are obtained as a weighted sum for the spin distribution.

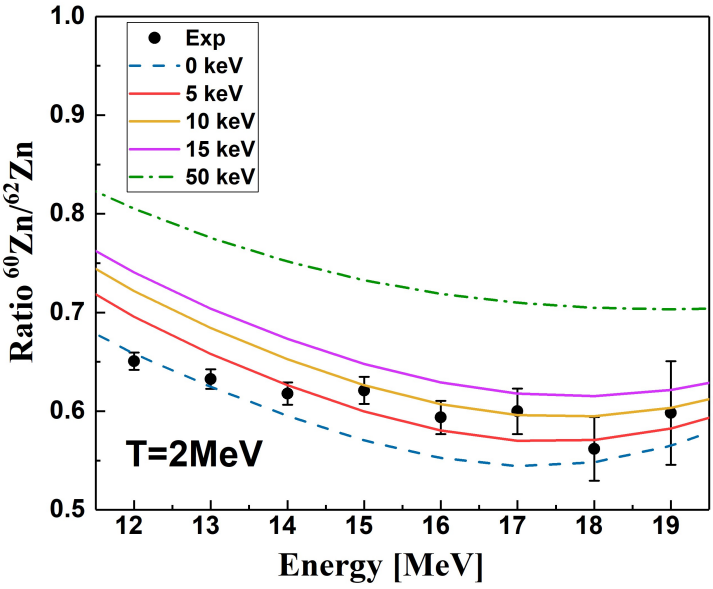

(a) Ratio $^{60}Zn/^{62}Zn$ at $T = 2$ MeV

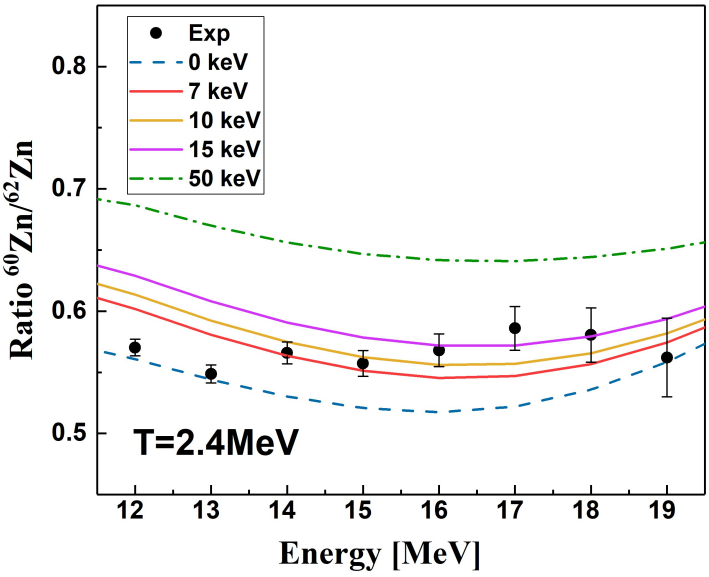

(b) Ratio $^{60}Zn/^{62}Zn$ at $T = 2.4$ MeV

Figure 7.8: Experimental ratio $^{60}Zn/^{62}Zn$ together with the statistical model ratios with different Coulomb spreading width values. For T=2.4 MeV the result of the experimental ratio is in agreement with the expected one.

CHAPTER 8

The isospin mixing probability

Finally, in conclusion, let me say just this

Peter Sellers

In this chapter we are going to use the values obtained for the Coulomb spreading widths for the nucleus at both temperatures to deduce the isospin mixing parameter at fixed temperature. Then, we will propose a model that describes the mixing probability as a function of temperature and we will deduce the isospin mixing at T=0. To conclude we will calculate the value of the isospin mixing breaking correction term δ_c for the first term of the CKM matrix.

8.1 Coulomb spreading width

The values of $CSW = 5 \pm 3$ keV for T=2 MeV and of $CSW = 7 \pm 3$ keV for T=2.4 MeV were obtained. In figure 8.1, the measured value of $\Gamma^{\downarrow}_{>}$ is compared with the values available in literature. For sake of visibility, we reported the mean value between our two results that is $\Gamma^{\downarrow}_{>} = 6 \pm 2$ keV. Our datum (orange square) is in good agreement with the experimental trend. At the top right corner there is a log scale zoom in the region of mass 60.

8.2 Isospin mixing in the nucleus ^{60}Zn

The statistical model provides as output the value of $\alpha^2_{><}(J)$ distribution, once $\Gamma^{\downarrow}_{>}$ is given as input, as reported in figure 8.2. The spin dependence of the isospin mixing is due to the fact that the internal energy of the system (and thus the nuclear temperature) depends on the rotational energy of the system (eq 6.3).

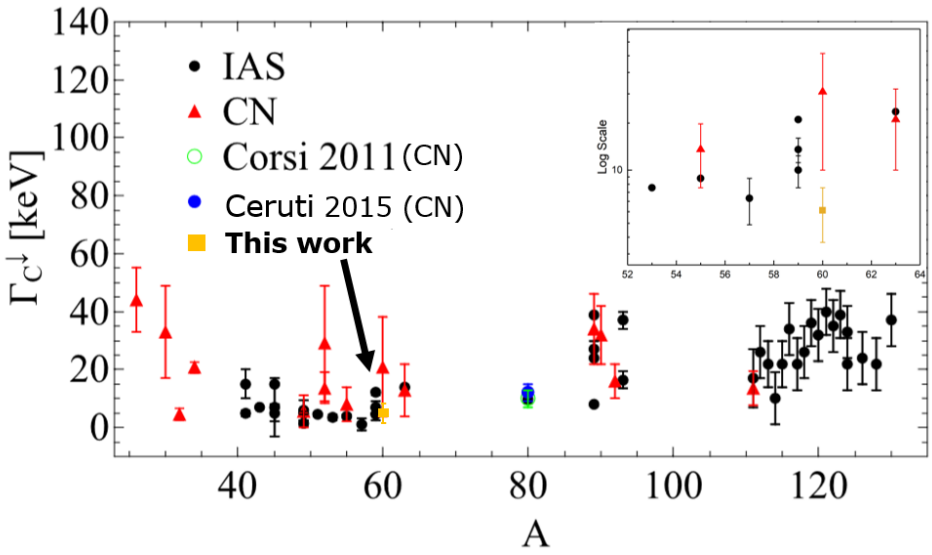

Figure 8.1: Values of the Coulomb spreading width obtained in the IAS (black dots and in the CN (red triangle) (66, 61). The blue and green points are the values obtained in (32) and (33), while the orange square is the value obtained in this work. At the top right corner there is a log scale zoom in the region of the point obtained.

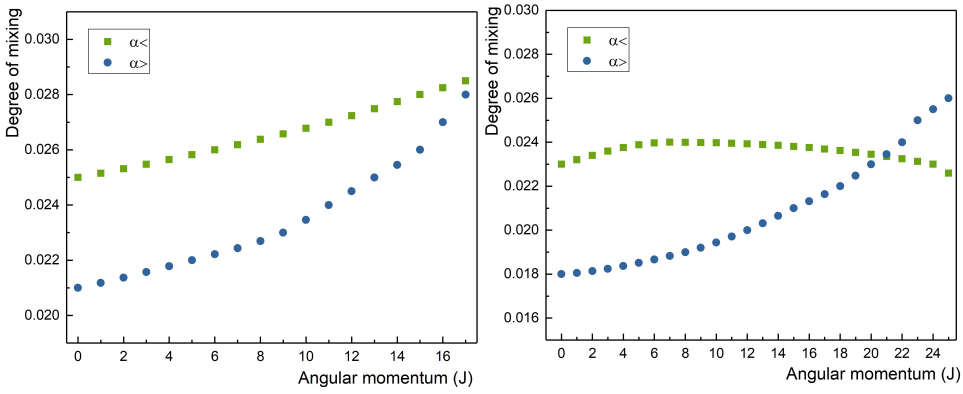

(a) Alpha at T = 2 MeV *(b) Alpha at T = 2.4 MeV*

Figure 8.2: Degree of mixing $\alpha_>(J)$ (blue dots) and $\alpha_<(J)$ (green squares) along to the CN angular momentum (up to the maximum value) for T=2 MeV on the left and T=2.4 MeV on the right.

As expected, the mixing is stronger on colder and long-lived CN. This is evident in the increment of the degree of mixing with the angular momentum of the system. The average of the mixing probability of table 8.1 is obtained by weighting the spin population over the fusion cross section and the γ branching ratio, i.e. the probability of gamma emission over the total decay probability.

T[MeV]	$\alpha^2_<(\%)$	$\alpha^2_>(\%)$
2	2.7 ± 1.5	2.5 ± 1.5
2.4	2.4 ± 1.0	2.2 ± 0.8

Table 8.1: The mean values (over J) of $\alpha^2_{><}$ for both temperatures.

8.2.1 Isospin mixing in the nucleus ^{60}Zn at T=0 MeV

As we described in the paragraph 1.3.5, a theoretical model of the isospin mixing in function of temperature was proposed by Sagawa, Bortignon, Colò as reported in reference (2). This model allows to extrapolate the α^2 value from T>0 to T=0, where one can find most of the theoretical calculations. The isospin mixing probability for a nucleus at finite temperature is defined as:

$$\alpha^2_{T_0+1} = \frac{1}{T_0+1} \frac{\Gamma^{\downarrow}_{IAS}}{\Gamma_{CN}(E^*) + \Gamma_{IVM}(E_{IAS})} \tag{8.1}$$

where $\Gamma_{CN}(E^*)$ is the compound nucleus decay width, $\Gamma^{\downarrow}_{IAS}$ is the width of the IAS (considered equal to $\Gamma^{\downarrow}$) and $\Gamma_{IVM}(E_{IAS})$ is the width of the Isovector Monopole Resonance (IVM) at the excitation energy of the IAS. This quantity has to be considered a parameter of the model, because is impossible to measure it. The experimental points of α^2 are obtained through the CASCADE statistical model simulations in which the parametrization of Harney, Ritcher and Weidenmüller (61) is implemented. The comparison between the experimental data and this temperature-dependent model require some additional notes:

- The Sagawa, Bortignon, Colò model has an explicit dependence on temperature, as opposed to the Harney, Ritcher and Weidenmüller parametrization.
- The Sagawa, Bortignon, Colò model is a first order approximation and it represents a static view of the mixing effect instead, the Harney, Ritcher and Weidenmüller parametrization is a second order description in which the possibility that $I_>$ states mix back to $I_<$ ones is taken into account. This means that the mixing effect is described as a dynamical process.

- The Sagawa, Bortignon, Colò model doesn't consider the angular momentum dependence, thus the mixing parameter is defined at J=0.

Therefore, we need to evaluate the α^2 at J=0. In table 8.2 the compound nucleus decay widths ($\Gamma^{\uparrow}_{CN}$), the Coulomb spreading widths ($\Gamma^{\downarrow}$) and the values of α^2 at J=0 for both temperatures are reported. Each parameter is associated with both $<$ and $>$ values, where the first represents the state $I_< = I_z = 0$ and the second the $I_> = I_z + 1 = 1$.

T[MeV]	$\Gamma^{\uparrow}_{CN<}[keV]$	$\Gamma^{\uparrow}_{CN>}[keV]$	$\Gamma^{\downarrow}_{<}[keV]$	$\Gamma^{\downarrow}_{>}[keV]$	$\alpha^2_<(\%)$	$\alpha^2_>(\%)$
2	130	230	3.3 ± 2.0	5 ± 3	2.5 ± 1.4	2.1 ± 1.2
2.4	210	370	5.1 ± 2.2	7 ± 3	2.3 ± 1.0	1.8 ± 0.8

Table 8.2: The compound nucleus decay widths ($\Gamma^{\uparrow}_{CN}$), the Coulomb spreading widths ($\Gamma^{\downarrow}$) and the values of α^2 at J=0 for both temperatures are reported. Each parameter is associated with both $<$ and $>$ values, where the first represents the state $I_< = I_z = 0$ and the second the $I_> = I_z + 1 = 1$. The two Coulomb spreading widths ($\Gamma^{\downarrow}_{<}$ and $\Gamma^{\downarrow}_{<}$) and the two mixing probabilities ($\alpha^2_<$ and $\alpha^2_>$) have the same order of magnitude, because the level densities of the two states $I_< = I_z = 0$ and $I_> = I_z + 1 = 1$ are similar.

In figure 8.3 the values of the Coulomb spreading widths (in the upper part) and of the $\alpha^2_>(\%)$ at J=0 (in the lower part) are reported together with the values available in literature deduced by GDR γ-decay measurements. The red square is relative to ^{32}S measured in (35) at T=2.7 MeV, the yellow square and the brown point are the two values deduced in this thesis on ^{60}Zn at T=2 MeV and T=2.4 MeV, respectively and the light blue square and the blue point are the measurements performed by S. Ceruti (32) and A.Corsi (33) on ^{80}Zr at 2 MeV and 3 MeV, respectively. In the upper part of the figure, together with the single measurements, an average of all values available in literature, taken with different techniques, are shown as colored rectangle, around mass 32, mass 60 and mass 80. We want to point out that the mixing probability depends on the number of proton in the nucleus and on the temperature, thus, varying both of them (as in the lower part of the figure), it is not possible to deduce a trend.

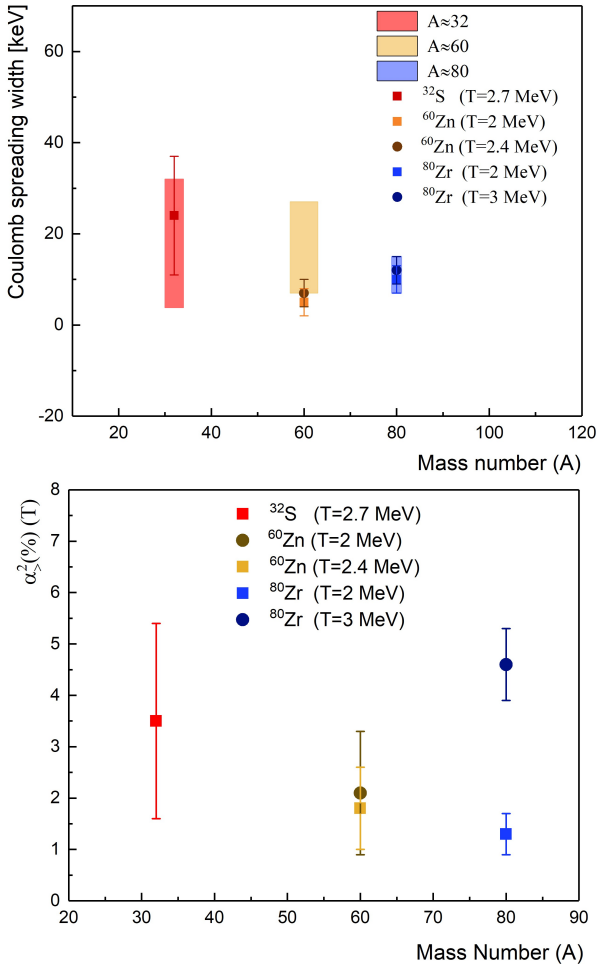

Figure 8.3: Upper panel: values of the Coulomb spreading widths are reported together with the values available in literature deduced by the GDR γ-decay measurements and with average of values, taken with different techniques, shown as colored rectangle, around mass 32, mass 60 and mass 80. Lower panel: $\alpha^2_{>}(\%)$ at J=0 corresponding to the Coulomb spreading widths shown in the upper part. For both panels: The red square corresponds to the nucleus ^{32}S measured in (35) at T=2.7 MeV, the yellow square and the brown point are the two values deduced in this thesis on ^{60}Zn at T=2 MeV and T=2.4 MeV, respectively and the light blue square and the blue point are the measurements performed by S. Ceruti (32) and A.Corsi (33) on ^{80}Zr at 2 MeV and 3 MeV, respectively.

In the equation 8.1, $\Gamma_{IVM}(E_{IAS})$ is a parameter, namely it is constant with temperature and because it cannot be measured experimentally, the value was fixed at 240 keV as reported in (32). $\Gamma_{CN}(E^*)$ increase strongly with temperature and $\Gamma^{\downarrow}$ could be considered either constant with temperature or a small dependence, as expressed by the following relation can be implemented:

$$\Gamma^{\downarrow}(T) = \Gamma(T=0)(1+cT) \tag{8.2}$$

where the parameter c is fixed at $c = 0.1\ MeV^{-1}$ as in (32). The trends are shown in figure 8.4 and in the upper part the temperature dependence of the Coulomb spreading width is shown.

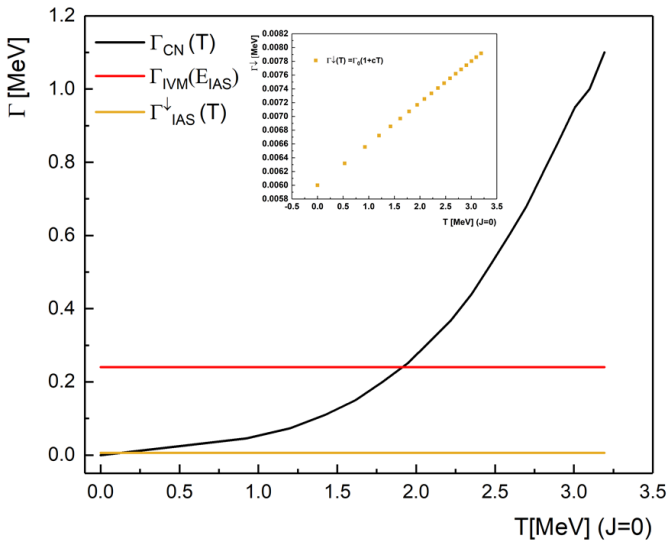

Figure 8.4: Trend of the 3 parameters of the equation 8.1. The $\Gamma_{IVM}(E_{IAS})$ is constant with temperature, instead the $\Gamma_{CN}(T)$ increase with temperature. The curve was obtained, through the CASCADE code, calculating $\Gamma_{CN}(T)$ at J=0 in an excitation energy interval from 0 to 100 MeV, corresponding to a temperature interval from 0 to 3.2 MeV. The $\Gamma^{\downarrow}$ could be considered constant with temperature or have a small dependence as shown in the upper part of the figure.

For comparison with the two previous works on isospin mixing of ^{80}Zr by Ceruti (32) and Corsi (33) we considered the value associated to $I_> = I_z + 1$ comparing the experimental $\alpha^2_>$. In figure 8.5 two bands representing the trend of $\alpha^2_>$, calculated with the equation 8.1, are shown as a function of T. The red band is calculated with a $\Gamma^{\downarrow} = 6 \pm 2$ keV as obtained from the average value of the Coulomb spreading

widths at the two temperatures. The blue band is deduced introducing the small temperature dependence of $\Gamma^{\downarrow}$ following the equation 8.2, introduced in (2). The black squares, namely the values obtained in this analysis with the related error bars are in agreement with the theoretical bands. With this model we can also extract the value of $\alpha^2_>$ at T=0 (where the compound nucleus decay width is zero), that results 2.5 $\pm$ 0.8 %. The comparison between this value and the prediction in (3) of $\alpha^2_>$ at T=0 for the ^{60}Zn that is equal to 2.2%, is shown as a yellow star in figure 8.5. The value obtained is also in line with a result on ^{64}Ge ((37)) that shows $\alpha^2(T=0) = 2.5^{+1}_{-0.7}\%$. These data, with the addition of the value at T=0 deduced in (32) on ^{80}Zr and the theoretical trend predicted by (3) are shown in figure 8.6. In figure 8.7 the comparison between the trends of $\alpha^2_>$ with temperature, for the nucleus ^{60}Zn (deduced in this thesis) and the nucleus ^{80}Zr (obtained in (32)), together with the experimental points at different temperatures and the prediction at T=0 reported in (3) are shown.

8.2.2 δ_c in ^{60}Zn

In (27), N. Auerbach proposed a simple analytic relation between the isospin mixing breaking correction term δ_c for the first term (V_{ud}) of the CKM matrix and the isospin mixing probability. δ_c is not measurable directly and it is linked to the isospin mixing coefficient as follow:

$$\delta_C = 4(I+1)\frac{V_1}{41\xi A^{\frac{2}{3}}}\alpha^2 \tag{8.3}$$

where $V_1 = 100$ MeV and $\xi = 3$, while α^2 is the isospin impurity in the ground state and I the isospin of the nucleus. From this equation we obtained the value of $\delta_c = 0.53 \pm 0.17\%$.

In the upper part of figure 8.8 the value obtained in this work is compared with two different theoretical calculation from the Damgaard model (38) and a shell model with Saxon-Woods radial wave function prediction (39). Black circles are the experimental points extracted from β decay as reported in Ref. (25), the blue triangle is the value obtained from the mass measurement in Ref. (29). The red star at mass 80 is the value obtained in (32) whilst the red star at mass 60 is the value of δ_c extracted in this work. It is plotted the quantity $\frac{\delta_c}{(I+1)}$ since β-decay measurements are for I = 1 nuclei, while that for ^{60}Zn is I = 0. In the lower part of the figure, the same experimental points are compared with values calculated using the equation 8.3 starting from the theoretical model of $\alpha^2(T=0)$ reported in (3).

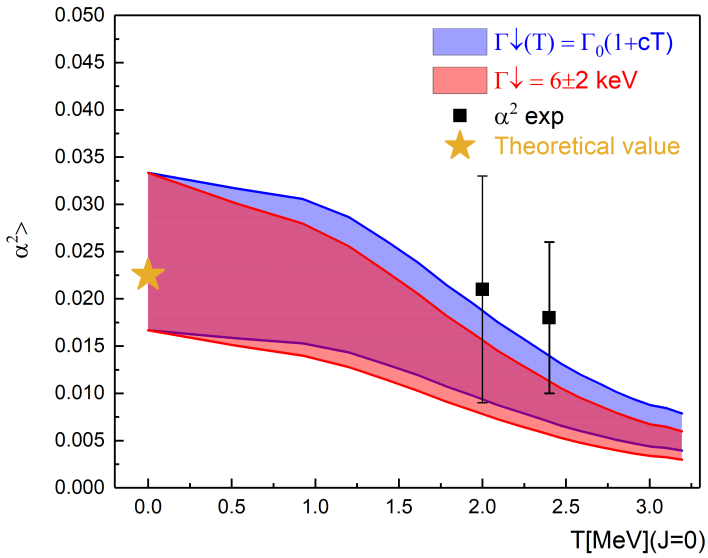

Figure 8.5: Values $\alpha^2_>$, calculated with the equation 8.1, as a function of T. The red band is calculated with a $\Gamma^{\downarrow} = 6 \pm 2$ keV as obtained from the analysis of ^{60}Zn ratio in the previous section. The blue band is deduced introducing the small temperature dependence of $\Gamma^{\downarrow}$ with temperature following the equation 8.2. The yellow star is the value at T=0 predicted in (3) and the black squares are the values obtained in this analysis with the related error bars.

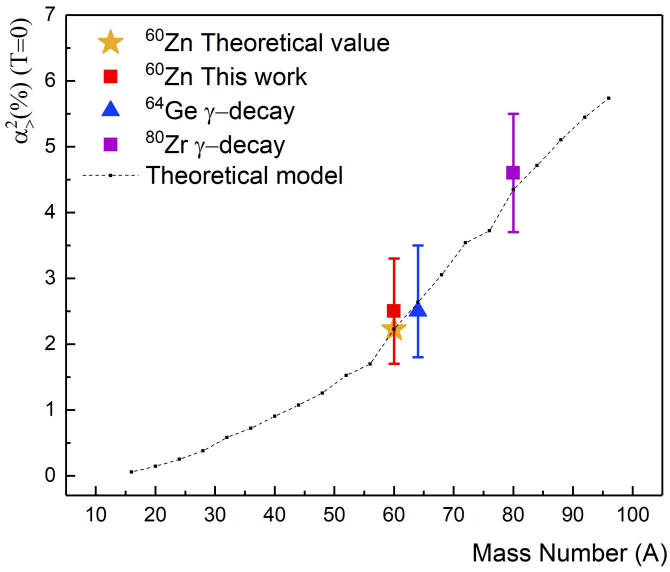

Figure 8.6: Comparison between α^2 data at T=0. The red square is the value on ^{60}Zn obtained in this work whilst the yellow star is a prediction in (3) of $\alpha^2_>$ at T=0 for the ^{60}Zn that is equal to 2.2%. The blue triangle is a result on ^{64}Ge ((37)) that shows $\alpha^2(T=0) = 2.5^{+1}_{-0.7}\%$. Moreover, the value at T=0 deduced in (32) on ^{80}Zr and the theoretical trend predicted by (3) are displayed.

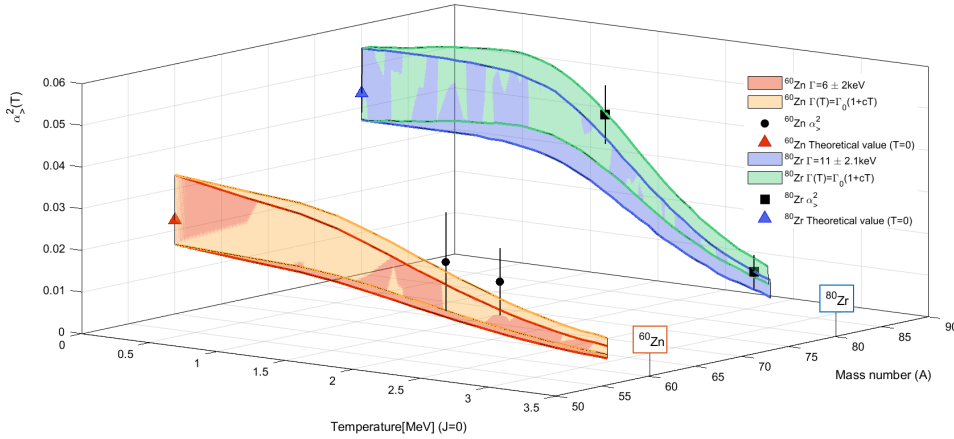

Figure 8.7: Comparison between the trends of $\alpha^2_>$ with temperature, for the nucleus ^{60}Zn (deduced in this thesis) and the nucleus ^{80}Zr (obtained in (32)), together with the experimental points at different temperatures and the prediction at T=0 reported in (3).

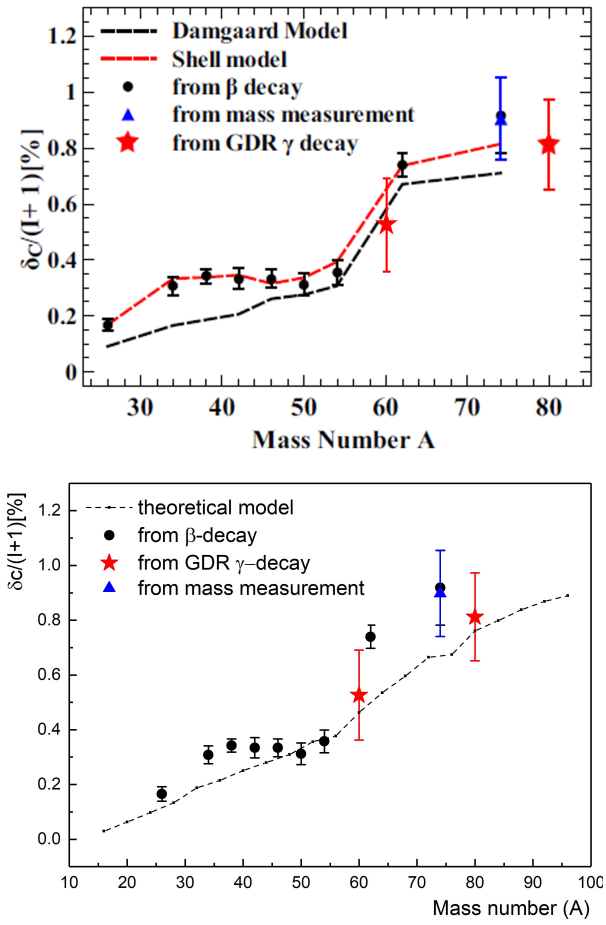

Figure 8.8: In the upper part, the isospin mixing correction δ_c as a function of the nuclear mass number A is shown. The dashed black line is the prediction from the Damgaard model (38), while the red line is a shell model with Saxon-Woods radial wave function prediction (39). Black circles are the experimental points extracted form β decay as reported in Ref. (25) , the blue triangle is the value obtained from the mass measurement in Ref. (29). The red star at mass 80 is the value obtained in (32) whilst the red star at mass 60 is the value of δ_c extracted in this work. It is plotted the quantity $\frac{\delta_c}{(I+1)}$ since β-decay measurements are for $I = 1$ nuclei, while that for ^{60}Zn is $I = 0$. In the lower part of the figure, the same experimental points are compared with values calculated using the equation 8.3 starting from the theoretical model of $\alpha^2(T = 0)$ reported in (3).

Conclusions

The goal of this PhD thesis was to extract the isospin mixing coefficient for the nucleus ^{60}Zn at two different temperature T=2 MeV and T=2.4 MeV, to verify the temperature dependence predicted by Wilkinson (6), to extrapolate the value at T=0 and to deduce the value of δ_c.

The preliminary analysis on the data shows that the oxygen contamination in the target can't be eliminated from the experimental spectra. We considered the system as a mix between ^{60}Zn and ^{48}Cr and we fitted the ^{62}Zn spectra to obtain the GDR parameters, namely centroid, width and strength. Because ^{60}Zn and ^{62}Zn have a very similar mass we made the assumption that the GDR spectra must have the same shape and thus, we applied the GDR parameters of ^{62}Zn to the ^{60}Zn spectra for both temperatures.

The only free parameter remains, in this way, the Coulomb spreading width. Performing n statistical model simulations, varying the CSW from 0 to 50 keV and carrying out a χ^2 minimization between them and the experimental points, we obtained the CSW values that best reproduce the experimental data, namely 5 ± 3 keV (T=2 MeV) and 7 ± 3 keV (T=2.4 MeV).

From the statistical model and the Coulomb spreading width values we obtained the experimental $\alpha^2_{><}$. The comparison with the temperature dependent model predicted in (2) let us to extract the value at T=0. The $\alpha^2_>(T=0) = 2.5 \pm 0.8\%$ is in good agreement with the theoretical prediction (3) and the experimental results in literature (25, 37).

In addition, the isospin-symmetry-breaking correction δ_c used for the Fermi superallowed transitions was extracted as $\delta_c = 0.53 \pm 0.17\%$. Our result is in good agreement with the theoretical and experimental mass-trend. This result supports the validity of the method based on the GDR at finite T to obtain isospin mixing in regions of Z not directly accessible at T = 0.

Publications

1. G. Gosta "Study of the Isospin Symmetry in 60Zn" Acta Physica Polonica B (2019)
2. G. Gosta "Isospin symmetry in the 60Zn nucleus" Acta Physica Polonica B (2020)

Bibliography

[1] S. Ceruti, et al., Phys. Rev. C 95, 014312 (2017).

[2] H. Sagawa, P. F. Bortignon, G. Colò, Phys. Lett. B 444, 1 (1998) and private communication.

[3] W. Satuła, et al., Phys. Rev. Lett. 103, 012502 (2009).

[4] J. A. Behr, et al., Phys. Rev. Lett. 70, 3201 (1993).

[5] M. Harakeh and A. Woude, Giant Resonances: Fundamental High-frequency Modes of Nuclear Excitation, Oxford science publications (Oxford University Press, 2001).

[6] D. Wilkinson, Isospin in nuclear physics (North Holland Pub. Co., 1970).

[7] P E Hodgson 1987 Rep. Prog. Phys. 50 1171

[8] P. Bortignon, A. Bracco, and R. Broglia, Giant Resonances: Nuclear Structure at Finite Temperature, Contemporary concepts in physics (Harwood, 1998)

[9] E. Gadioli and P. E. Hodgson, Pre-Equilibrium in Nuclear Reaction (Oxford Science Publications, 1992).

[10] R. J. Charity, Phys. Rev. C 82, 014610 (2010).

[11] R. Bass, Nuclear Reaction with Heavy Ions, Theoretical and Mathematical Physics (Springer-Verlag Berlin Heidelberg, 1980).

[12] W. Hauser and H. Feshbach, Phys. Rev. 87, 366 (1952).

[13] B. L. Berman and S. C. Fultz, Rev. Mod. Phys. 47, 713 (1975).

[14] A.Tamii PRL 107, 062502 (2011)

[15] Goldhaber, M., and E. Teller, 1948, Phys. Rev. 74, 1046

[16] D. M. Brink, PhD Thesis, Oxford University (1955).

[17] P. Axel, Phys. Rev. 126, 671 (1962).

[18] W. Heisenberg, 1932, Z.Phys. 77,1

[19] H. J. Hofmann, et al., Nucl. Phys. A571, 301 (1994)

[20] M. MacCormick and G. Audi, Nuclear Physics A 925, 61 (2014).

[21] W.A. Fowler, L.A. Delsasso and C.C. Lauristen,1936, Phys. Rev. 49,561.

[22] G. A. Miller et al., Annu. Rev. Nucl. Part. Sci. 56, 253 (2006).

[23] H. Morinaga, Phys. Rev. 97, 444 (1955).

[24] A. Bohr and B. R. Mottelson, Nuclear Structure: Single particle motion, Vol. 1 (World Scientific, 2008).

[25] I. S. Towner and J. C. Hardy PHYSICAL REVIEW C 77, 025501 (2008)

[26] W. Satuła, J. Dobaczewski, W. Nazarewicz, and M. Rafalski, Phys. Rev. Lett. 106,132502 (2011).

[27] N. Auerbach, Phys. Rev. C. 79, 035502 (2009).

[28] I. S. Towner and J.C. Hardy, Phys. Rev. C. 82, 065501 (2010).

[29] A. Kellerbauer et al., Phys. Rev. Lett. 93, 072502 (2004).

[30] N. Severijns, et al., Phys. Rev. C 71, 064310 (2005)

[31] M. Harakeh, et al., Physics Letters B 176, 297 (1986).

[32] S. Ceruti, et al., Phys. Rev. Lett. 115, 222502 (2015).

[33] A. Corsi, et al., Phys. Rev. C 84, 041304 (2011).

[34] E. Kuhlmann, Phys. Rev. C 20, 415 (1979).

[35] D. Mondal, et al., Physics Letters B 763, 422 (2016).

[36] M. Kicinska-Habior, et al., Nuclear Physics A 731, 138 (2004).

[37] E. Farnea, et al., Physics Letters B 551, 56 (2003).

[38] J. Damgaard, Nucl. Phys. A 130, 233 (1969).

[39] I. S. Towner, J. C. Hardy, and M. Harvey, Nucl. Phys. A 284, 269 (1977).

[40] A. Mentana, Ph.D. thesis, Physics, Astrophysics and Applied Physics PhD School, Università degli Studi di Milano, Milano (2017)

[41] J. Valiente Dobòn et al., Lnl-infn annual report 2014 (2015).

[42] A. Giaz, et al., Nuclear Instruments and Methods in Physics Research Section A: Accelerators, Spectrometers, Detectors and Associated Equipment 729, 910 (2013).

[43] D. Testov Eur. Phys. J. A (2019) 55: 47

[44] *Ö*. Skeppstedt, et al., Nuclear Instruments and Methods in Physics Research Section A: Accelerators, Spectrometers, Detectors and Associated Equipment 421, 531 (1999).

[45] SPES project: https://web.infn.it/spes/

[46] Glenn F. Knoll, Radiation Detection and Measurements (John Wiley and Sons. Inc., 2000) p. 396.

[47] J. Ljungvall, M. Palacz, and J. Nyberg, Nuclear Instruments and Methods in Physics Research Section A: Accelerators, Spectrometers, Detectors and Associated Equipment 528, 741 (2004).

[48] D.Barrientos, IEEE TRANSACTIONS ON NUCLEAR SCIENCE, VOL. 62, NO. 6, DECEMBER 2015

[49] D. Barrientos et al., Lnl-infn annual report 2014 (2015).

[50] J. Gutleber, S. Murray, and L. Orsini, Computer Physics Communications 153, 155 (2003).

[51] A. Gozzellino (2017), workshop GALILEO Days 2017, 20-22 September 2017, Laboratori Nazionali di Legnaro (LNL-INFN, PD Italy).

[52] E.Beneduce, Bachelor thesis, "Studio della relazione tra molteplicità e fold nell'array GALILEO"

[53] D. Jannis, Master's thesis, KU Leuven - Faculty of Science (2017).

[54] https://radware.phy.ornl.gov/

[55] V. Rigato and Laboratori Nazionali di Legnaro (LNL-INFN), private communication.

[56] J. Ljungvall, J. Nyberg Nuclear Instruments and Methods in Physics Research Section A 546 (2005) 553-573.

[57] S. Ceruti, Ph.D. thesis, Physics, Astrophysics and Applied Physics PhD School, Università degli Studi di Milano, Milano (2016)

[58] S. Lodetti, Bachelor thesis, Università degli Studi di Milano (2011-2012).

[59] P*ü*hlhofer, F. Nucl. Phys. A 280, 267 (1977).

[60] Harakeh, M. N., Dowell, D. H., Feldman, G., Garman, E. F., Loveman, R., Osborne, J. L., and Snover, K. A. Phys. Lett. B 176, 297 (1986).

[61] H. L. Harney, A. Ritcher and H. A. Weidenm*ü*uller, Rev. Mod. Phys. 58, 607 (1986).

[62] A. Corsi, Ph.D. thesis, Physics, Astrophysics and Applied Physics PhD School, Università degli Studi di Milano, Milano (2009)

[63] J. A. Behr, Ph.D. thesis, University of Washington (1991).

[64] Nudat - national nuclear data center, URL www.nndc.bnl.gov/.

[65] G. Gosta, Nuclear Inst. and Methods in Physics Research, A 879 (2018) 92–100

[66] J. J*ä*necke, M. N. Harakeh and S. Y. Van der Werf, Nucl. Phys. A 463, 571 (1987).